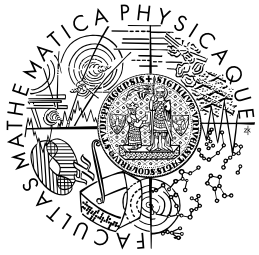

FACULTY
OF MATHEMATICS
AND PHYSICS
Charles University

DOCTORAL THESIS

Petr Cejpek

Study of indium doped shape-memory alloy Ni_2MnGa

Department of Condensed Matter Physics

Supervisor of the doctoral thesis:	RNDr. Milan Dopita, PhD.
Study programme:	Physics
Study branch:	4F3

Prague 2021

I declare that I carried out this doctoral thesis independently, and only with the cited sources, literature and other professional sources.

I understand that my work relates to the rights and obligations under the Act No. 121/2000 Sb., the Copyright Act, as amended, in particular the fact that the Charles University has the right to conclude a license agreement on the use of this work as a school work pursuant to Section 60 subsection 1 of the Copyright Act.

In ..... date ..... signature of the author

I hereby would like to show my appreciation to my supervisor RNDr. Milan Dopita, PhD. for guiding my work, for suggestions to its processing and also for the help with X-ray diffraction measurements. Many thanks belong to prof. RNDr. Václav Holý, CSc. and Mgr. Lukáš Horák, PhD. for the fruitful discussion about the X-ray diffraction problematics and its experimental aspects. Next, I would like to thank to RNDr. Petr Doležal for helping me with the measurement of X-ray diffraction at low temperatures. I want to thank to RNDr. Petr Opletal, Mgr. Petr Proschek and RNDr. Petr Čermák, PhD. as well for helping me with the magnetisation measurements. A part of my thanks also belongs to RNDr. Jaroslav Valenta, PhD. who helped me with the resistivity measurements and with the preparation of the sample for these experiments. I want to thank to RNDr. Klára Uhlířová, PhD. and Mgr. Kristina Vlášková for sealing the glass tubes for the annealing of the samples. I would like to thank to RNDr. Jiří Pospíšil, PhD., RNDr. Michal Vališka, PhD. and Dr. Ross Harvey Colman for the discussion about single crystal growth. Also, I want to acknowledge Ing. Barbora Vondráčková for helping me with the DSC measurements at high temperatures and RNDr. Přemysl Vaněk, CSc. for the DSC measurement at low temperatures. Thanks also belong to Denys Mussienko, D.Sc. who performed the XRF measurements of the samples composition. The special thanks belong to prof. Kristián Mathis, PhD., DrSc. and RNDr. Daria Drozdenko, PhD. who enabled the in-situ measurements with the tensile stage. Last but not least, I want to appreciate a lot the help of Dr. Oleg Heczko, Ing. Ladislav Straka, DSc. and RNDr. Martin Veis, PhD. who introduced me to Ni_2MnGa concepts and helped me a lot with writing of my first article.

The work presented in this thesis was supported by Grant Agency of Charles University (GAUK), project No. 244217. I want to acknowledge the financial support from the project NanoCent - Nanomaterials Centre for Advanced Applications, Project No. CZ.02.1.01/0.0/0.0/15_003/0000485, financed by ERDF. The work was also supported partly by the project MatFun, Project No. CZ.02.1.01/0.0/0.0/15_003/0000487, financed by ERDF as well. Samples preparations and measurements were performed in MGML (mgml.eu), which is supported within the program of Czech Research Infrastructures (Project No. LM2018096).

Title: Study of indium doped shape-memory alloy Ni_2MnGa

Author: Petr Cejpek

Department: Department of Condensed Matter Physics

Supervisor: RNDr. Milan Dopita, PhD., Department of Condensed Matter Physics

Abstract: The alloys related to Ni-Mn-Ga system exhibit effects connected to the magnetic shape-memory and martensitic transformation and therefore attract attention of researchers for their application potential. Properties and especially transformation temperatures are strongly dependent on composition, doping and also on external conditions as a magnetic field or pressure.

The main aim of the work was to prepare own single crystals of $Ni_2MnGa_{1-x}In_x$ and to study their properties with respect to the temperature and applied fields in dependence on a various indium doping. The transformation temperatures obtained from the measurement of electrical resistivity and magnetisation revealed the systematic decrease of martensitic transformation temperature T_M, pre-martensitic transformation temperature T_P and Curie temperature T_C. The martensitic transformation should vanish at indium concentration of $x \approx 0.10$. The decrease with indium content is much faster than in the study published previously on the polycrystalline samples (vanishing at $x \approx 0.20$). This discrepancy is probably caused by the residual stress remaining in polycrystalline samples from arc melting preparation. The measurements in various magnetic field revealed the increase of T_M and T_P in the order of 0.2-0.6 K/T.

The lattice parameters and the structure modulation were examinated by X-ray diffraction. Indium increases unit cell volume and also increases the volume change during the martensitic transformation. Indium also influences modulation parameters - the increasing indium content increases the length of the modulation vector in the pre-martensitic phase and decreases its length in the martensite. It also decreases the pre-martensitic modulation amplitude.

The last part of the thesis was dedicated to the measurement of X-ray diffraction in-situ in tension on the off-stoichiometric $Ni_{50}Mn_{28}Ga_{28}$ with the martensitic phase at room temperature. When c axis (the shortest) is along the direction of the tension, the elongation of the sample is done primarily by the induced reorientation (creation of the new domains suitably oriented to the tension by twinning and increasing of their volume). When a or b axes lie along the direction of tension, the overall elongation happens primarily due to the change of the lattice parameters. This sample orientation also allows the tension to rapidly decrease the modulation amplitude with the applied tension.

Keywords: Ni-Mn-Ga alloys, shape memory, twinning, structure modulation, single crystal growth

Contents

Introduction

The materials related to the Ni-Mn-Ga system attract significant attention. Since they belong to the magnetic shape-memory alloys family they have promising potential applications as actuators, sensors, micropumps or magnetic refrigerators [1, 2, 3]. These applications are related to magnetically induced reorientation (MIR) [4] and giant magnetic-field induced strain (MFIS) – up to 12 % can be reached by appropriate doping [4, 5, 6, 7, 8].

However, preparation of a good single-crystal shows itself to be necessary to observe significant effects connected to the MIR and MFIS. Grain boundaries can block the motion of twin boundaries. Even in a single crystal the MFIS might be hard to achieve as the twin boundary motion can be suppressed by various lattice imperfections. Moreover, a single crystal is necessary for precise determination of the structure.[9, 10]. The milling to prepare powder samples can induce large stresses in the lattice, which can result in stress-induced martensite transformation and moreover, it can strongly affect or even destroy the specific arrangement necessary for MIR.[11, 12, 13, 14]

The properties of Ni_2MnGa related materials are connected to the martensitic transformation, during which the high-temperature cubic phase (austenite) undergoes a transformation to the low-temperature phase with lower symmetry (martensite) [15, 16, 17, 18, 19]. In most cases the martensitic phase exhibits the structure modulation [19, 9, 10], however, the non-modulated Ni-Mn-Ga martensite has also been reported [6, 4]. Depending on composition, one could observe additional pre-martensitic phase. Pre-martensitic transformation (austenite to pre-martensite) occurs at temperatures higher than martensitic transformation temperature (T_M) and it is connected to the partial condensation of the transversal acoustic phonon branch [20, 21].

Many works were published describing the behavior of martensitic transformation in Ni-Mn-Ga related alloys under various conditions. The critical temperatures of Ni-Mn-Ga based alloys are strongly dependent on alloying and composition. For example, the partial substitution of Mn with Ni atoms results in an increase of T_M and a decrease of Curie temperature (T_C) [22]. Contrary, substitution of Mn with Fe leads to a decrease of T_M and to an increase of T_C [23, 24]. The alloying of Ni sites with Co increases the Curie temperature, but contrary to that T_M is decreased [24, 25]. Replacing Ga or Mn site with Cu causes T_M increase [24, 26].

There is the empirical rule about the dependence of the critical temperatures on the valence electrons concentration [27, 28]. However, taking into account alloying with various elements, this empirical rule is not valid generally, because the experimentally obtained critical temperatures have a wide spread around the fitted dependences. Recently, Armstrong et al. [29] published the study dealing with the systematic trends of transformation temperatures in Ni-Mn-Ga-Fe-Cu alloys which treats the influence of individual element concentrations on T_M and T_C.

The martensitic transformation temperature T_M is influenced also by the external conditions such as pressure or magnetic field. Application of magnetic field in the vicinity of T_M can be used for the actuation purpose by means of magnet-

ically induced (reverse) martensite transformation (MIM), which could be then used similarly as the classical thermal shape memory effect. In a magnetic field, the phase with the higher magnetic moment is energetically favored which leads to a shift of T_M [30], consequent transformation, and shape change. This was shown already for $Ni_{45}Co_5Mn_{36.6}In_{13.4}$ alloy by Kainuma et al. [31] and Heczko et al. [32] has for example shown this effect in the thin film of $Ni_{51}Mn_{23}Ga_{26}$.

The change in the magnetisation during the martensitic transformation enables the magnetocalorical effect (MCE). Promising MCE in Ni-Mn-Ga alloys can be achieved by the preparation of compounds with the off-stoichiometric composition [33, 32] or with element substitution. Concerning the latter, alloying by indium plays an important role, since it enlarges the magnetisation difference between austenite and martensite. However, it simultaneously decreases T_M [34, 35], therefore the compensation for that is needed. This can be achieved by an additional alloying with yet another element or using off-stoichiometric compositions (e.g. Mn-rich Ni-Mn-Ga [36]) to increase T_M back to the suitable temperature region.

The aim of this thesis is to prepare single-crystalline samples and study the effects of alloying of Ga atomic sites with In atoms. Since In and Ga are isoelectric elements, the abovementioned empirical rule cannot be followed because the average number of valence electrons per atoms is unchanging. Several articles dealing with In alloying were already published [37, 38, 39, 40, 34, 41, 42]. Kitanishi, et al. [37] investigated the shear and the bulk modulus of $Ni_2MnGa_{1-x}In_x$ on a base of the first principles theory. The articles [38, 39, 40, 41] showed the study of Co and In alloyed Ni_2MnGa in the purpose of an examination of magnetocaloric properties. Khan et al. [34] studied systematically the behavior of the physical properties with respect to indium content. Glavatskyy et al. [42] studied the Ni_2MnGa compound under the various alloying with Si, In, Co and Fe. All these experimental papers showed that indium alloying decreases the critical temperatures. However, it needs to be pointed out that these works were done on polycrystalline samples and the aim of this thesis is to study single crystals.

One part of the thesis is also dedicated to the influence of magnetic field on the martensitic transformation temperature T_M. In magnetocalorics, the effect of magnetic field on T_M is an important parameter. Indium alloying causes the decrease of T_M in the applied magnetic field [43, 44, 45, 46, 47]. The corresponding slopes are usually several K/T. For example, Bourgault et al. [43] reported -2.5 K/T for $Ni_{45}Co_5Mn_{37.5}In_{12.5}$, Huang et al. [44] -4.9 K/T for $Ni_{49.8}Co_{1.2}Mn_{33.5}In_{15.5}$, Chen et al. [45] approximately -6 K/T for various amount of Co/Fe alloying and Krenke et al. [46] even -8 K/T at low fields for off-stoichiometric $Ni_{50}Mn_{34}In_{16}$. The negative slope of several K/T was reported also for the Co-alloying only [47]. In contrast, for the Ni-Mn-Ga without alloying the positive slopes have been reported. In absolute values, these slopes are smaller – approximately +0.6 K/T for $Ni_{50}Mn_{26}Ga_{22}$ [33] and for $Ni_{50}Mn_{30}Ga_{20}$ [47] and i.e. +0.36 K/T for $Ni_{51}Mn_{23}Ga_{26}$ already mentioned above [32]. For the alloyed samples, the positive shift about +2 K/T was reported by Mendonça et al. [48] within their magnetostriction studies on the Cu- and Al-alloyed Ni-Mn-Ga.

This thesis is divided into several parts. In the first chapter, the physical concepts common for Ni-Mn-Ga related shape-memory alloys are introduced. The second chapter is dedicated to experimental methods and their theoret-

ical aspects. The following parts of the thesis deal with the samples preparation, their characterisation and the results obtained from physical properties measurement and the results from X-ray diffraction measured at different temperatures. A single chapter deals also with the X-ray diffraction measurement on off-stoichiometric Ni_2MnGa in-situ at different tensions. The last chapter is dedicated to the discussion of the obtained results.

1. Physical concepts in Ni-Mn-Ga shape-memory alloys

In this chapter, the structure of Ni-Mn-Ga will be introduced. The main physical concepts such as twinning or shape-memory will be described. In the last part possible applications of the shape-memory alloys will be discussed.

1.1 Structure

1.1.1 Basic structure

The parent structure of Ni_2MnGa is cubic and we label it as the austenitic phase. Since the Ni_2MnGa belongs to full-Heusler alloys [49, 50], the austenitic structure can be described with the space group $Fm\bar{3}m$ (n. 225) where Ni, Mn and Ga atoms sit at 8c, 4b and 4a positions respectively. The unit cell of austenite is depicted in Figure 1.1. At low temperatures the structure undergoes a martensitic transformation to a less symmetric martensitic phase. Its structure can be tetragonal, orthorombic or even monoclinic [15, 16, 17, 18, 19] (depending on the composition of the sample). The main feature of the martensitic transformation is the shortening of the lattice parameter c (for Ni_2MnGa from $a_{austenite} = 5.83$ Å to $a_{martensite} = 5.92$ Å, $c_{martensite} = 5.56$ Å, $\gamma_{martensite} = 90.3°$ [15]).

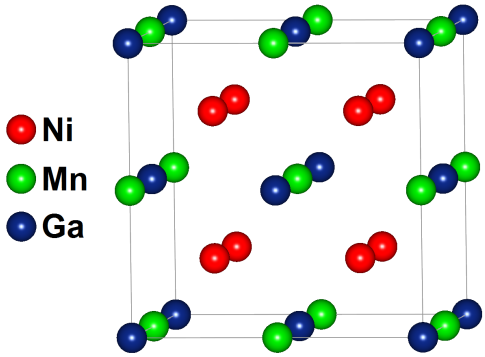

Figure 1.1: Ni_2MnGa unit cell

1.1.2 Types of ordering

Different types of atomic ordering can be observed in Ni_2MnGa related alloys. The most important for us is the $L2_1$ ordering and B2′ ordering [49, 51]. The $L2_1$ ordering is such arrangement of the unit cell where no mixing of atoms on the individual atomic sites is allowed (each atomic site is occupied only by one element). This ordering corresponds to the arrangement of atoms in Figure 1.1. In B2′ ordering, the Mn and Ga are equally mixed on their atomic sites (see Figure 1.2). This ordering usually remains in the sample after the single crystal growth when the sample is uncontrollably cooled. The natural goal is to prepare a single crystal which contains the $L2_1$ ordering only, therefore the heat treatment of the as grown samples is needed to get rid of the B2′ ordering.

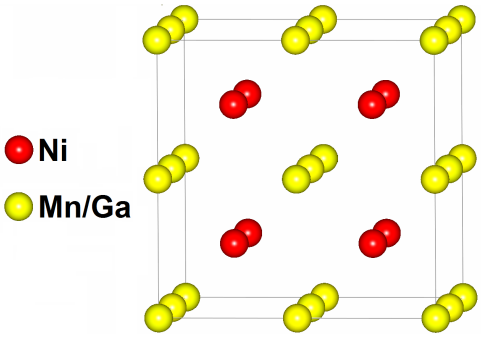

Figure 1.2: B2′ ordering in Ni_2MnGa unit cell

1.1.3 Structure modulation

In most cases the martensitic phase exhibits the structure modulation [19, 11, 9], however, the non-modulated Ni-Mn-Ga martensite has also been reported [4, 6]. In the X-ray or electron diffraction this modulation leads to the creation of well observable satellite maxima [19, 52]. The modulation is created as periodical shift of atoms in the crystallographic basal plane (001) while the modulation is pronounced along the direction [110]. The modulation amplitude points along $[\bar{1}10]$.

The period of the modulation depends on the sample composition. One type of the modulation is labeled 10M which corresponds to the period of 10 atomic planes (along (110)) and the modulation vector $q_{mod} = \left[\frac{2}{5}, \frac{2}{5}, 0\right]$. The modulation 10M is depicted in Figure 1.3a. Another type of modulation is labeled 14M. It corresponds to the period of 14 atomic planes and the modulation vector $q_{mod} = \left[\frac{2}{7}, \frac{2}{7}, 0\right]$. There is still discussion whether the modulation is commensurate or incommensurate, because an incommensurate modulation in Ni-Mn-Ga alloys was also reported [9]. However, the values of the modulation vectors for these samples lie still around $\left[\frac{2}{5}, \frac{2}{5}, 0\right]$ or $\left[\frac{2}{7}, \frac{2}{7}, 0\right]$.

In the high temperature cubic phase one could observe another type of modulation pronounced along [110] and the corresponding modulation vector is $q_{mod} = \left[\frac{1}{3}, \frac{1}{3}, 0\right]$. It is connected to the partial condensation of the transversal acoustic phonon branch [53, 20, 21]. This is labeled as the pre-martensitic phase and the pre-martensitic transformation occurs at temperatures above the martensitic transformation.

1.1.4 Phases and critical temperatures

There is a sketch in Figure 1.4 to make better overview of the phases and critical temperatures in Ni-Mn-Ga. As it was already mentioned, the high temperature cubic phase is labeled as austenite. Because the Ni-Mn-Ga is the ferromagnet, it undergoes the ferromagnetic transition at Curie temperature T_C (373 K for Ni_2MnGa [51]). Going down with the temperature, the pre-martensitic phase is created at T_P (temperature of the pre-martensitic transformation, 220 K for Ni_2MnGa [51, 53]) via the modulation with the wave vector $q_{mod} = \left[\frac{1}{3}, \frac{1}{3}, 0\right]$. Finally, at the temperature T_M (202 K for Ni_2MnGa [15, 51]) the material undergoes the martensitic transformation to the martensitic phase. Depending on composition of the sample, the martensite can be modulated.

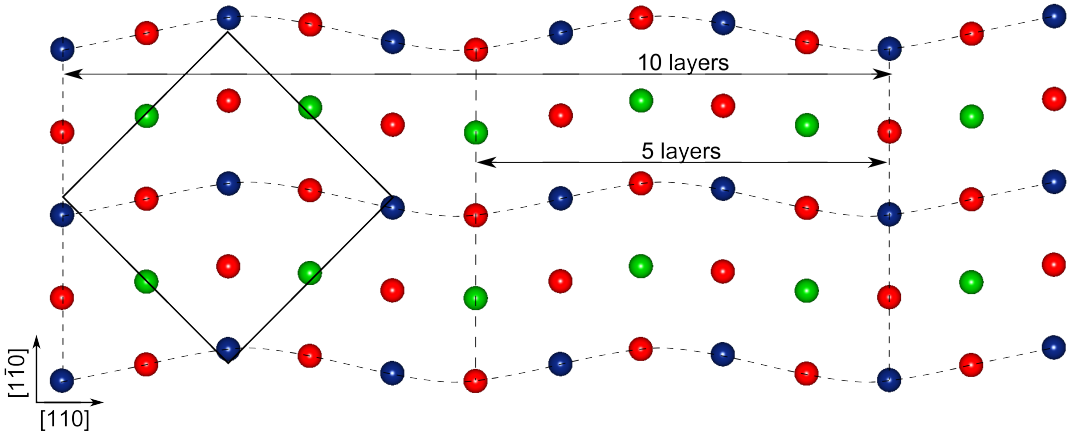

(a) 10M modulation with a sinusoidal wave

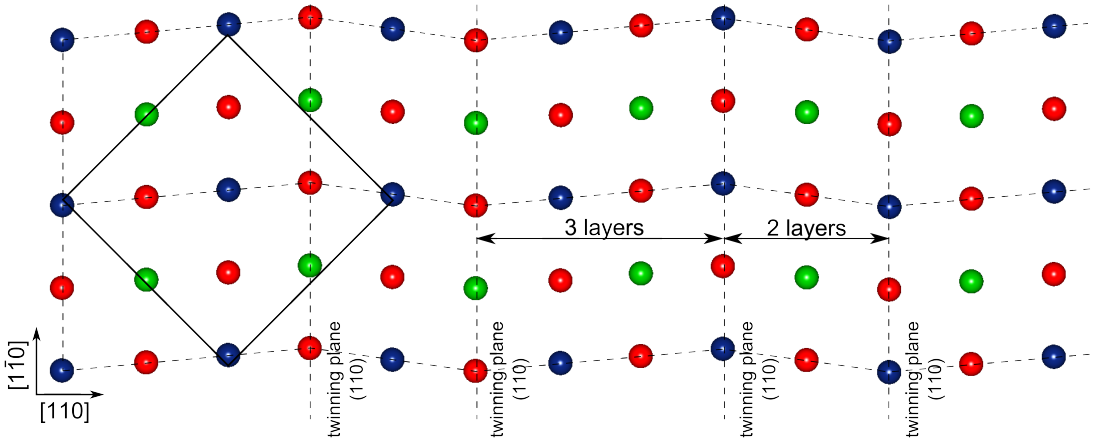

(b) 10M modulation explained by the nano-twinning (adaptive concept)

Figure 1.3: 10M modulation in Ni_2MnGa. The crystallographic axis [001] is perpendicular to the figure. The original unit cell is highlighted by the solid lines, the dashed lines correspond to the modulation wave of the atomic displacements.

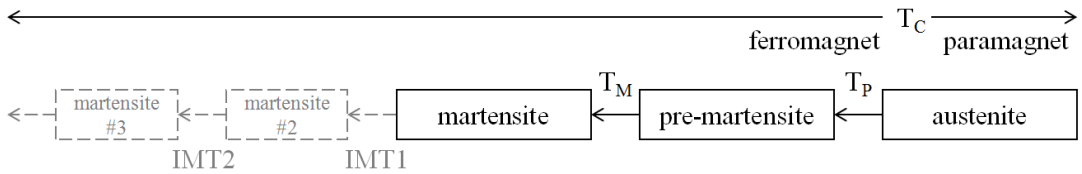

Figure 1.4: Phases in Ni-Mn-Ga alloy

The martensitic transformation is the transition of the first kind. Therefore, it has the hysteresis with respect to temperature, usually about 10-20 K [51, 35, 54, 55]. Moreover, since the critical temperature can be quite easily shifted by composition [27, 54], T_M could be shifted above T_P and the pre-martensitic transformation would not be observed at all. The material will transform directly from austenite to martensite [50, 19].

In some of the off-stoichiometric Ni-Mn-Ga (composition different from 2:1:1 ratio) the intermartensitic transformations (IMTs) can be also observed. Within those transitions the modulation type of the martensitic phase changes towards the non-modulated structure which should be the most stable at low temperatures [56, 57]. The individual sequence of modulation changes depends also on the composition [58]. The IMTs are indicated in Figure 1.4 by the dashed lines.

Concerning the martensitic transformation, one could label four different temperatures regarding the phase of the transformation process: M_s and M_f are martensite start and martensite finish temperatures (during the cooling). Similarly, A_s and A_f are the start and finish temperatures of the reverse martensite transformation (during the heating). The equilibrium temperature T_M is calculated as the average of these four values, i.e. $T_M = (M_s + M_f + A_s + A_f)/4$. The individual temperatures can be determined by the conventional tangential method which is sketched in Figure 1.5. The individual parts of the temperature dependence of the studied physical quantity in the vicinity of the transformation points are fitted with linear functions (or with polynomial functions if necessary). The temperatures M_s, M_f, A_s and A_f then lies at the intersection points of these functions as it is sketched in Figure 1.5.

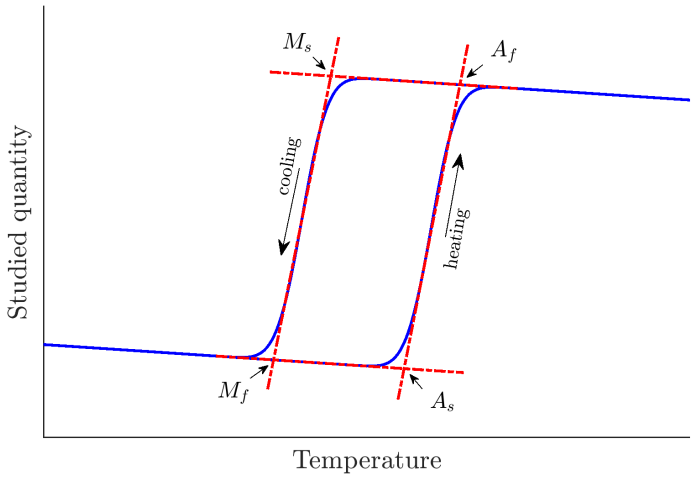

Figure 1.5: The sketch of the tangential method to determine the characteristic temperatures of the martensitic transformation

1.2 Shape-memory

A shape-memory materials can be deformed in the martensitic phase and returned to its original shape by heating to the austenitic phase. The effect can be also referred as a thermal shape-memory. However, ferromagnetic shape memory

alloys based on Ni-Mn-Ga can exhibit so-called magnetic shape-memory (MSM). This phenomena occurs in the low temperature martensitic phase - the material can be influenced by an application of an external magnetic field or a mechanic force and produces strain in order of several percents (or even 12 % [6]).

The mechanism responsible for this strain is magnetically induced reorientation (MIR) and it is sketched in Figure 1.6 (taken from [59]). Because the Ni-Mn-Ga is ferromagnetic, it exhibits macroscopic magnetisation when an external magnetic field is applied. However, it is more energetically preferable to align magnetic moments by the rotation of whole unit cells and not by the rotation of individual magnetic moments within the cells.

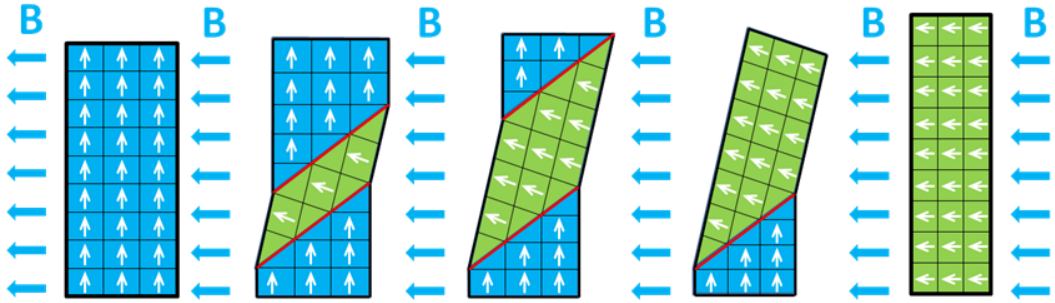

(a) Magnetically induced reorientation (MIR)

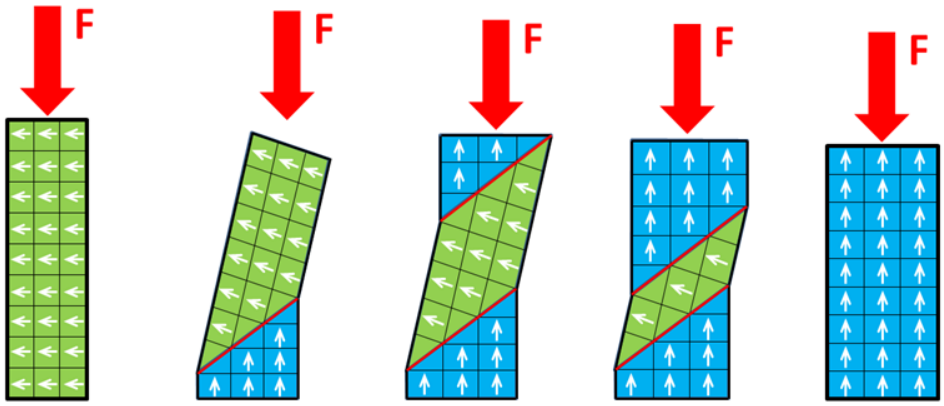

(b) The reorientation induced by the application of a mechanical force

Figure 1.6: The sketch of Ni-Mn-Ga sample reorientation induced by magnetic or mechanical forces. The figure is taken from [59].

This is the consequence of the large magnetic anisotropy, and the high mobility of the internal regions called twins or twin variants. The magnetic anisotropy in the martensitic phase is in order of 10^5 J/m^3 and depends on the structure of the martensite [60] (10M, 14M or non-modulated). The mobility of twin boundaries is inversely proportional to a twinning stress and can be computed from the magnetic stress obtained from the measurement of magnetisation curves [61, 62]. The twinning stress is approximately 0.1 MPa at room temperature for $Ni_{49.9}Mn_{28.3}Ga_{21.8}$ [61] and it increases with decreasing temperature (i.e. mobility of twin boundaries decreases).

The twin mobility is also the reason why the preparation of single crystal is prerequisite for the clear observation of MIR. The motion of twins can be blocked

by lattice imperfections and grain boundaries in a polycrystal. Moreover, milling polycrystalline samples to a powder induces large stresses, which can result in the stress-induced martensitic transformation [11] or even the shift of T_M [63] (similar to an application of the hydrostatic pressure on Ni_2MnGa [64].

1.2.1 Twinning

Theoretical description of twinning

We can describe the twinning theoretically by the means of deformation twinning [65, 66]. By convention, the twin is a region of a crystal that has undergone a homogeneous shape deformation (a shear) and it has the same structure as the parent domain but differently oriented. Assuming that the twin and the parent domain remain in contact, the orientation of the twin is given by exact geometrical relation. The twin can be characterized by several parameters:

- K_1 - the twinning plane (invariant plane of the shear)
- $\vec{\eta}_1$ - the twinning direction or the direction of the shear lying in K_1
- K_2 - the reciprocal twinning plane (the second undistorted but rotated plane of the shear)
- $\vec{\eta}_2$ - the reciprocal twinning direction lying in K_2

The operation describing the orientation relation must leave the twinning plane invariant. We can consider the four classical situations obtained by:

1. reflection over K_1
2. rotation of 180° around $\vec{\eta}_1$
3. reflection over the plane perpendicular to $\vec{\eta}_1$
4. rotation of 180° around the normal of K_1

By the closer examination of the geometry of the resulting twins, we can find out, that only two new orientations arose and the cases 1) and 4) are equivalent (similarly also the cases 2) and 3)). Therefore, we can classify the case 1) and 4) as the twinning type I and the case 2) and 3) as the twinning type II. The twinning can be also classified according to the rationality of K_1, η_1, K_2, η_2. For type I K_1 and η_2 are rational, for type II η_1 and K_2 are rational and if all mentioned parameters are rational, we have so-called compound twinning.

The lattice vectors (in the direct lattice) of the parent and twin could be related as follows:

$$\vec{b}_i = \vec{a}_i - 2\left(\vec{a}_i \cdot \vec{K}'\right)\vec{K}' \tag{1.1}$$

$$\vec{b}_i = \vec{a}_i - 2\left(\vec{a}_i \cdot \vec{\eta}'\right)\vec{\eta}' \tag{1.2}$$

where $\vec{a}_i$ are the lattice vectors of the parent domain, $\vec{b}_i$ are the lattice vectors of the twin, $\vec{K}'$ is the unit vector perpendicular to the plane K_1 and $\vec{\eta}'$ us the unit vector along the direction $\vec{\eta}_1$.

1.2.2 Twinning in Ni_2MnGa

According to different set of parameters K_1, η_1, K_2, η_2 we can divide the twinning in Ni_2MnGa into several groups [67]:

- **compound twinning** - twinning plane K_1 is (110) or $(1\bar{1}0)$. It is responsible for creation of so called a/b laminate, which is the sequence of smaller domains along which the a and b lattice vectors are alternating. Compound twinning plays also the role in the adaptive concept of modulation (see further).

- **modulation twinning** - twinning plane K_1 is (100) or (010). If the modulation is pronounced along [110] crystallographic direction it means that the modulation twinning switches the modulation to the perpendicular direction $\left[\bar{1}10\right]$.

- **twinning type I** - the characteristic planes of this twinning is (101) and (011) (or $(10\bar{1})$ and $(01\bar{1})$). It is responsible for the switching between a/c and b/c axes.

- **twinning type II** - it is similar to previous twinning with the difference that the characteristic parameter is the direction $\eta_1 = [101]$ and [011] (or $\left[\bar{1}01\right]$ and $\left[0\bar{1}1\right]$)

- **non-conventional twinning** - for this case, both K_1 and η_1 are irrational (according to [67] the twinning plane $K_1 \doteq [-0.9509; 0.3094; 0]$ or $K_1 \doteq [0.3094; 0.9509; 0]$.

Considering this list, the MIR depicted in Figure 1.6 can be explained by the shift of the twin boundary which is parallel to the twinning plane of twinning type I or II. The initial single variant (the whole sample is only one twin) which has for example the a axis along the direction of the external field transforms into the variant with c axis pointing along the field direction. This means that the fully transformed sample is contracted with the corresponding strain $\epsilon = \frac{c-a}{a} \approx 6\%$ (for stoichiometric Ni_2MnGa).

The presence of the twinning is directly visible in diffraction experiment. For example, due to the manipulation of the sample and sticking it on the holder by pressing one could induce a creation of many twin variants and it leads to the splitting of diffraction spots. For instance, the Bragg reflection 400 is split to 400, 040 and 004 [19, 50]. On the other hand, a single variant sample can be prepared by a defined pressing. And the single variant state can be good prerequisite for the precise measurements [61, 50].

Twin boundaries of type I and II could be also well observed by electron or optical microscope [67, 68, 69, 70]. Moreover, with the known orientation of the sample, the type I and II can be distinguishable. Due to their geometrical relation, both twin boundaries should be mutually inclined approximately about 6 deg [67].

There is an approach called *adaptive concept* [71, 72] which tries to explain the modulation in Ni-Mn-Ga by a nano-twinning (the sketch for 10M modulation is depicted in Figure 1.3b). Here, the 10M modulation is formed by repeated twinning over the crystallographic plane (110) (compound twinning) on atomic planes

in the sequence 3,2,3,2,3,2 layers,. . . (see Figure 1.3b). Similarly, 14M modulation is formed by the sequence 5,2,5,2,5,2 layers,. . . . The incommensurate modulation is then created by the deviation from these sequences within the sample volume (e.g. 5,2,5,3,5,2,4,2. . .). Up to now, it is still not know which approach is correct, since the classical sinusoidal modulation and the nano-twinning model leads to the equivalent fits of the diffraction data [19, 73].

1.3 Compositional dependence

There is an empirical rule for the dependence of Ni-Mn-Ga properties on the concentration of valence electrons (the average number of valence electrons per atom). It is illustrated by Figure 1.7 taken from [27]. The saturated magnetisation has a peak-like dependence on the concentration of valence electrons. Its maximum lies at $\frac{e}{at} = 7.50$ (the number of valence electrons per atom) which is the value corresponding to stoichiometric Ni_2MnGa (Ni contributes with 10 valence electrons, Mn with 7 and Ga with 3). The valence electrons concentration also increases T_M. However, due to the large standard deviation of T_M with respect to the fit [27] it is obvious that the influence of individual dopant concentration on T_M should be either treated separately or the dependence is sensitive to other parameters such as a microstructure or a stress.

Armstrong et al. [29] published the study dealing with the systematic trends of transformation temperatures in Ni-Mn-Ga-Fe-Cu alloys. They took about 20 samples with various compositions and doping and they treated the influence of individual element concentrations on T_M and T_C separately. According to [29], T_M increases with higher Ni and Mn concentrations (see Figure 1.8). One can see also the separated regions corresponding to different modulation types (Figure 1.8a).

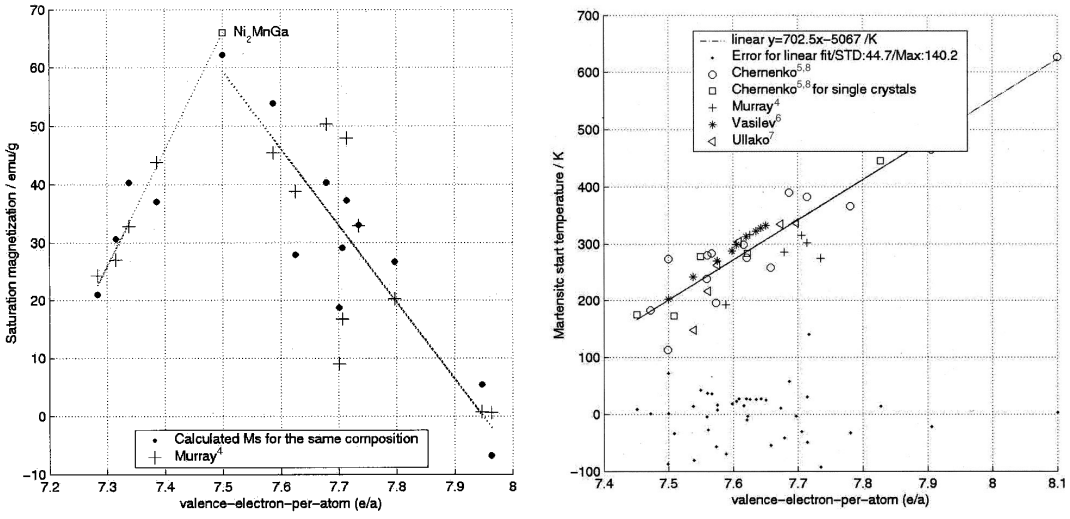

(a) M_S dependence on $\frac{e}{at}$ (b) T_M dependence on $\frac{e}{at}$

Figure 1.7: Empirical dependences of Ni-Mn-Ga properties on the concentration of the valence electrons taken from [27].

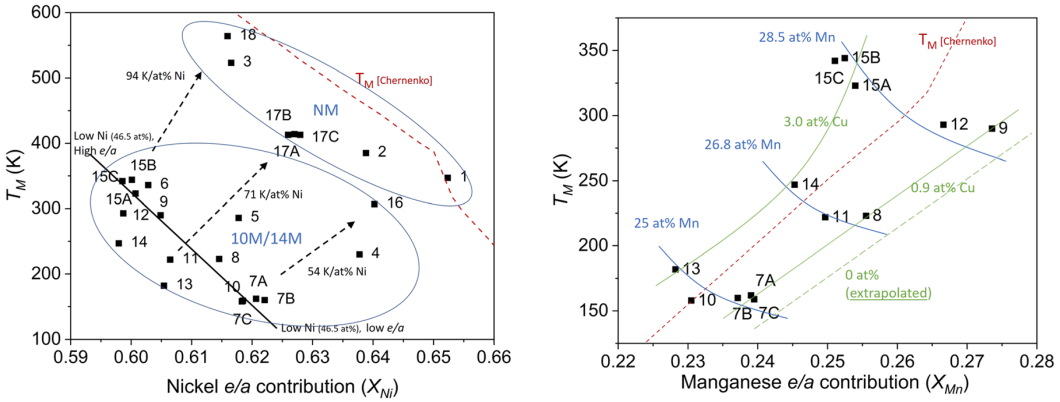

(a) T_M dependence on Ni concentration (b) T_M dependence on Mn concentration

Figure 1.8: Dependences of T_M on Ni and Mn concentration taken from [29]. The values on the horizontal axis corresponds to the valence electrons relatively to the overall number of the valence electrons in the compound. For the stoichiometric Ni_2MnGa: $X_{\mathrm{Ni}} = \frac{10+10}{10+10+7+3} = 0.\overline{666}$ and $X_{\mathrm{Mn}} = \frac{7}{10+10+7+3} = 0.2\overline{33}$.

1.4 Applications

Ni-Mn-Ga related alloys have an application potential on the field of micro-pumps, actuators or magnetic refrigerators [2, 3, 1]. The micro-pump applications use the strain induced by an external magnetic field. The sketch of the basic micro-pump based on the magnetic shape-memory effect can be seen in Figure 1.9 (taken from [1]). The permanent magnet rotating under the Ni_2MnGa specimen reorients a small part of the sample which leads to the shrinkage of this part. Then, it is shifted because the magnetic field moves due to the magnet rotation. The free space which originates above the shrank part of the Ni_2MnGa specimen can be used for the transfer of a gas or a liquid. The flow rate can be then controllable by the rotation speed of the permanent magnet. The advantage of these micro-pumps is the simplicity (the whole device consists only from few parts), electrical contacts are used for the magnet rotor only and the magnetic field required for the sample shrinkage is relatively small (cca 0.2 T [1]).

Magnetic refrigeration is a technology based on the magnetocaloric effect [3]. Here, the sample temperature changes during the exposition of the material to the changing magnetic field (sometimes referred as *the adiabatic demagnetisation*). The change in temperature is related to the change in magnetic entropy. Ni-Mn-X (X=Ga, Co, In, Al, Sb) alloys are good candidates for magnetic refrigerator because their T_C can be easily tuned by the amount of doping and therefore T_C can lie close to the room temperature [3]. The change of the magnetic entropy can be also increased by tuning of T_M by a composition - when T_M is close to T_C, change in magnetic entropy is even larger. Moreover, suitable magnetocaloric material often contains rare-earth elements (such as Gd and La [3, 74, 75]). But Ni-Mn-X is promising due to the cost reduction, because it is rare-earth free.

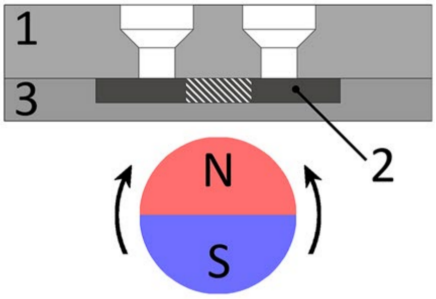

Figure 1.9: The sketch of the basic micropump based on the magnetic shape-memory effect taken from [1]. In the bottom part of the picture is the rotating magnet, the micro-pump in the upper part consists of several parts: (1) a polycarbonate plate which acts as the substrate, the holes work as an inlet and an outlet, (2) the magnetic shape memory material Ni–Mn–Ga (the striped section is the part shrank by magnetic field), (3) the elastomer which seals the channel and prevents leaking.

2. Theory and used experimental methods

In this chapter, the principles of the used theoretical method will be introduced. Theoretical formulas needed for the calculation and data processing will be presented as well.

2.1 Samples preparation

2.1.1 Single-crystal growth

Bridgman method

The first stage before a single crystal growth was a preparation of polycrystalline precursors. They were prepared in a monoarc furnace from 5N Ni, 7N Ga, 3N5 Mn and 5N In pellets in Ar atmosphere of 0.3 bar. To compensate the evaporation during the arc melting we added three extra weight percents of Mn and Ga, in advance. The single crystals were grown by Bridgman method from prepared precursors. For the single crystal preparation the precursor material was ground into a powder and placed in a BN or Al_2O_3 crucible and sealed inside a molybdenum capsule, therefore the evaporation was not an important issue during the single crystal growth. The sealed capsule was placed in the in-house built induction furnace using AC current of frequency 125 kHz. The sketch of the furnace and the cut through the molybdenum capsule is depicted in Figure 2.1.

Then, the capsule was heated to 1250°C (the melting point of Ni_2MnGa lies around 1130°C [51]) and then slowly pulled outside the hot zone. As the result of several growth attempts, the pulling speed of 0.5 mm/h was found as optimal for growth in our Bridgman furnace. Prepared single crystalline ingots were roughly 20 mm long and had 8 mm in diameter.

Floating zone method

The single crystals growth by the floating zone (FZ) method was performed in the commercial optical furnace from Crystal System Corporation Japan, model FZ-T-4000-VI-VPM-PC. For the growth in the floating zone the prepared polycrystalline precursor needed to be remelted into shape of the long rod (approximately 10 cm). Then, this ingot is cut in two pieces and placed into the FZ furnace (sketch in Figure 2.2). The bottom piece serves as a seed. Both pieces are carefully reconnected in the hot zone created by the four 1 kW halogen lamps which light is focussed by the elliptical mirrors to their common focus point. The chamber where the rod is placed is evacuated and filled with overpressure of Ar atmosphere (1.25 bar) to compensate possible evaporation of elements from the rod material. The single crystal growth is done by pulling the reconnected rod trough the hot zone. The furnace allows to shift both holders with different speed but we used this feature only at the beginning to create a neck. After that, the speed was set to 80 mm/h for both holders. The furnace also allows the rotation

of the holders. This was not used during the successful growth because of a creation of a crust. The crust (probably MnO) was originating at the surface of the melt and during the rotation the crust broke away the melt.

2.1.2 List of the samples

The list of the samples prepared and used in the performed experiments is shown in Table 2.1.

nominal chemical formula	**label**	**form**	**prepared / supported by**
Ni_2MnGa	NMG	bulk SC	Petr Cejpek[1)]
Ni_2MnGa	NMG_{FZ}	bulk SC	Petr Cejpek[1)]
$Ni_2MnGa_{0.98}In_{0.02}$	NMGIn2	bulk SC	Petr Cejpek[1)]
$Ni_2MnGa_{0.95}In_{0.05}$	NMGIn5	bulk SC	Petr Cejpek[1)]
$Ni_2MnGa_{0.90}In_{0.10}$	NMGIn10	bulk SC	Petr Cejpek[1)]
$Ni_2MnGa_{0.85}In_{0.15}$	NMGIn15	bulk SC	Petr Cejpek[1)]
$Ni_2MnGa_{0.25}In_{0.75}$	NMGIn25p	PC	Petr Cejpek[1)]
$Ni_2MnGa_{0.50}In_{0.50}$	NMGIn50	bulk SC	Petr Cejpek[1)]
$Ni_2MnGa_{0.75}In_{0.25}$	NMGIn75p	PC	Petr Cejpek[1)]
Ni_2MnIn	NMIn_p	bulk with several SC grains	Petr Cejpek[1)]
$Ni_{50}Mn_{26}Ga_{24}$	$NMG_{AdaptaMat}$	bulk SC	Ladislav Straka[2)]
$Ni_{50}Mn_{28}Ga_{22}$	N50M28G22	bulk SC	Ladislav Straka[2)]
$Ni_{50}Mn_{28}Ga_{22}$	$N50M28G22_{RC}$	bulk SC	Ross H. Colman[1)]

Table 2.1: The of the prepared samples, which were used in the performed experiments. The label FZ means the preparation by the floating zone method, the rest of the single crystals were grown by Bridgman method, SC - single crystal, PC - polycrystal. [1)] Department of Condensed Matter Physics, Faculty of Mathematics and Physics, [2)] Institute of Physics of Czech Academy of Sciences

2.1.3 Heat treatment

Resulting single crystals were sealed in quartz tube with the Ar atmosphere (1 bar) to reduce Mn evaporation in the following heat treatment done in a resistance furnace. At first, the samples were annealed at the temperature close bellow the melting point T_{melt} for five days (homogenization annealing). After that the temperature was decreased close above the B2′ →$L2_1$ ordering temperature $T_{B2'\rightarrow L2_1}$ [20, 51, 76], and held for two days (ordering annealing). Finally, the samples were quenched into water. For example, the NMG sample was annealed at 1000°C (homogenisation) and 850°C (ordering). The annealing temperatures for other samples depend on the indium concentration because it influences T_{melt} and $T_{B2'\rightarrow L2_1}$ (shown in Section 3.3).

Similar annealing procedure was already used for example in [20, 77, 78]. It was shown that the temperature hysteresis of the martensitic transformation is narrow on the samples treated this way [78]. The quenching was done to avoid long range diffusion and to retain $L2_1$ order during cooling. Upon ordering

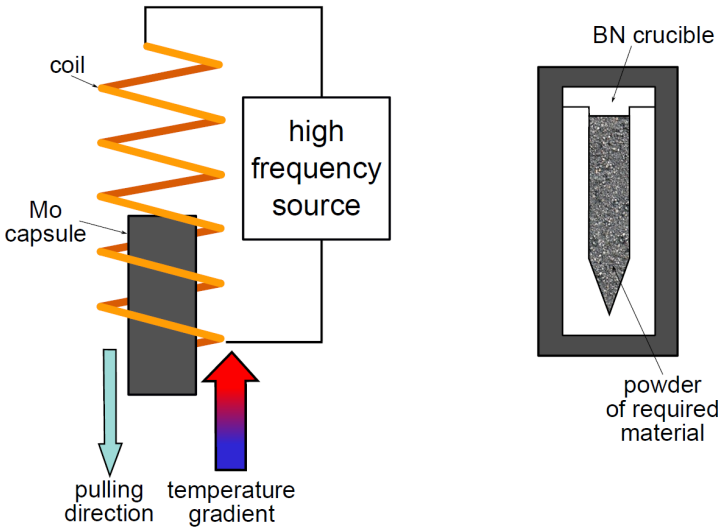

(a) vertical induction furnace

(b) cut through the molybdenum capsule

Figure 2.1: A sketch of the Bridgman method performed in the vertical induction furnace.

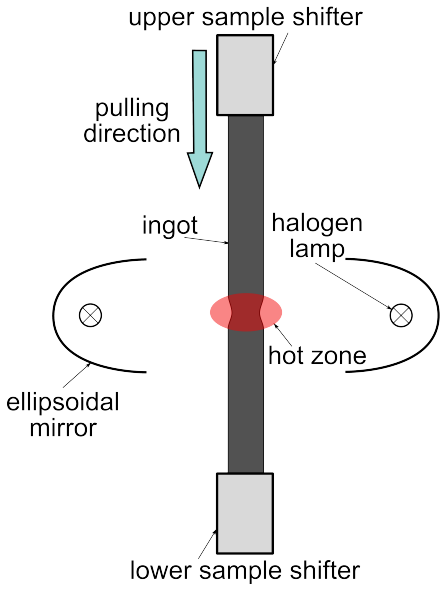

Figure 2.2: A sketch of the floating zone method performed in the optical furnace.

temperature the formation of $L2_1$ order is very fast as shown by Overholser et al. [79]. Santamarta, et al. [76], who studied similar compound Ni-Fe-Ga, proposed the explanation that quenching from high temperature above $B2' \rightarrow L2_1$ transition promotes the vacancy assisted diffusion, which leads to a higher degree of order than when quenching from lower temperatures.

2.2 Samples characterisation

2.2.1 Laue method

X-ray Laue System by Photonic Science, UK, was used to perform Laue method and to obtain information of a quality of our single crystals and their orientation for the following samples manufacturing. Our Laue machine works in the reflection geometry where the X-rays are screened by a small circular slit (diameter up to 1 mm), they reach the sample at a goniometer and the backscattered diffracted beams are registered on the plane CCD detector (155x105 mm) before the sample.

2.2.2 EDX and XRF

The chemical composition and homogeneity of prepared single crystals were checked by Energy Dispersive X-ray (EDX) spectroscopy and X-ray Fluorescence (XRF) method. The EDX experiments were performed on the scanning electron microscope Tescan MIRA I LMH equipped with Bruker Flash Energy Dispersive X-ray (EDX) detector. The polished sample is irradiated with the electron beam. The interaction of high energy electrons with the material in the sample produces secondary electrons. The electrons backscattered from the surface provide information about the surface topography. Secondly, the primary electron beam stimulate the emission of characteristic X-rays which are collected with EDX detector. Each element provides its unique spectrum because of its specific electronic structure. Therefore, scanning the surface with electron beam can be used to map the composition and to check the chemical homogeneity of the sample. The systematic error of EDX method is usually estimated as 2-3 % relatively to measured values of elements concentrations.

X-ray fluorescence method uses the similar principle, the only difference is that the emission of characteristic X-rays is stimulated by high energy X-ray beam. The experiments were performed at Czech Academy of Sciences on the in-house built XRF machine equipped with Rh X-ray tube. The accuracy for Ni, Mn and Ga for this machine is claimed to be in the range of 0.1-0.5 at%. because of the calibration with Ni-Mn-Ga standards.

2.2.3 DSC

To determine the melting temperatures and temperatures of $B2' \rightarrow L2_1$ transition, the heat-flux differential scanning calorimetry (DSC) was performed. The measurements were done on SETSYS Evolution instrument from SETARAM Instrumentation. The heating/cooling rate was set up to 10°C/min. The He was used as a protective atmosphere with the flow of 20 $\frac{\text{ml}}{\text{min}}$.

Within the experimental arrangement, the reference and the studied sample is connected by a metal strip, which is in the contact with thermal reservoir. The voltage of thermocouple corresponding to the temperature difference between the samples is measured as the resulting DSC signal. With the calibration using the standard samples with the known latent heat, it is also possible to determine the heats connected with the first order transitions.

2.2.4 Resistivity measurement

For the resistivity measurements, the samples were cut into a shape of small elongated prism (approximately 1x2x5 mm^3). The resistivity measurements themselves were done by four probe method in the closed cycle refrigerator constructed for temperature dependence measurements down to 4 K. The first attempts were performed with the contacts prepared by Ag paste. However, the forces occurring during the martensitic transformation were so big that the contacts were disrupt during the measurement. The effect on the measured data around T_M for the sample Ni_2MnGa can be seen in Figure 2.3. For that reason, we decided to prepare the samples with the point contacts from Au wires by the spot welding.

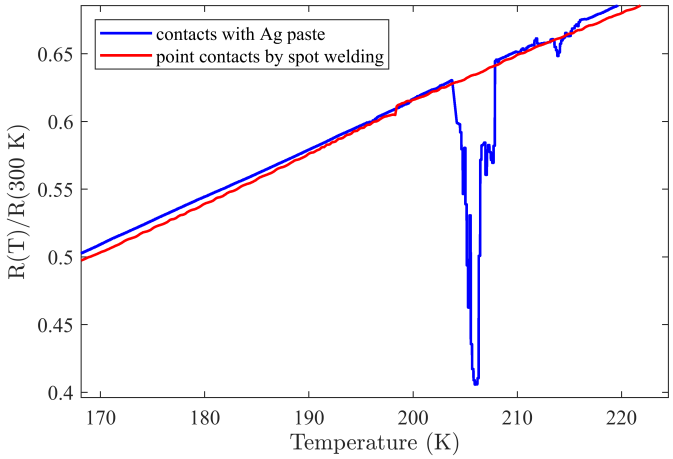

Figure 2.3: The comparison of resistivity measurements around T_M performed on the Ni_2MnGa sample with Ag paste contacts and the point contacts created by the spot welding

2.2.5 Magnetisation measurement

Magnetisation measurement were performed in Material Growth and Measurement Laboratory (MGML) [80] using the Physical Property Measurement System (PPMS) and Magnetic Property Measurement System (MPMS) - both by Quantum Design, Inc. in the temperature range of 4-400 K, up to 7 T of applied magnetic field. The Vibrating sample magnetometer (VSM) option was used for the magnetisation measurement on PPMS.

Demagnetisation

When the sample is exposed to the external magnetic field $\vec{H}_{ext}$, the magnetisation generates so-called demagnetizing field $\vec{H}_d$ inside the sample which acts oppositely

to the external field. This reflects the tendency to reduce the total magnetic moment of the specimen. The demagnetizing field depends on the geometry of the sample and it can be very difficult to calculate. For the special case of ellipsoids, demagnetising field is linearly related to the magnetisation $\vec{M}$ by a geometry-dependent demagnetizing factor N_d. Therefore, for the real magnetic field inside the sample we can write:

$$\vec{H} = \vec{H}_{ext} + \vec{H}_d = \vec{H}_{ext} - N_d\vec{M} \tag{2.1}$$

Let's assume we have the sample of the shape of an general ellipsoid (with the principal axes $c \geq b \geq a$) and the long axis c lies along the direction of the external magnetic field. The calculations [81, 82] lead to the following formula of the demagnetisation factor along c:

$$N_d^{\parallel} = \frac{r_a r_b}{k^2 \sin^3 \Theta} \left[F\left(\Theta, k\right) - E\left(\Theta, k\right)\right] \tag{2.2}$$

where $r_a = a/c$, $r_b = b/c = \cos\Theta$, $k = \sqrt{\frac{1-r_a^2}{1-r_b^2}}$ and $F\left(\Theta, k\right)$ and $E\left(\Theta, k\right)$ is an indefinite elliptical integral of the first and of the second kind respectively. The Equation 2.2 could be more simplified when we assume that the ellipsoid is the rotational one ($a = b$). In this case the demagnetisation factor [83, 84] is:

$$N_d^{\parallel} = \frac{1}{r^2 - 1}\left(\frac{r}{\sqrt{r^2-1}} \ln\left(r + \sqrt{r^2 - 1}\right) - 1\right) \tag{2.3}$$

where $r = c/a$ is the ratio of the principal axis lengths.

The usual way is to cut the samples into a shape of a prism with one longer side and to approach this shape as a rotational or a general ellipsoid. It follows from Equation 2.3 that the factor $N_d^{\parallel}$ decreases with the increasing ratio r. For $r = 5$ the $N_d^{\parallel} \approx 0.056$, for $r > 10$ it is less than 0.02, therefore the correction becomes negligible for the largely elongated samples (measured along their long side).

Magnetic energy and anisotropy

As it was mentioned in Section 1.1.1, the martensitic phase of Ni-Mn-Ga related alloys is tetragonal (or approximately tetragonal) with the lattice parameters $c < a \approx b$. As a consequence, we have one easy axis along c and two hard axes along a and b for the magnetisation. The corresponding magnetisation hysteresis loops could significantly differ as it is shown in Figure 2.4 for the sample $Ni_{48}Mn_{30}Ga_{22}$ [85]. The driving force for the twin boundaries movement during the MFIS is a difference of the magnetic energy of differently oriented twin variants in the magnetic field. Therefore, a large magnetic anisotropy is a prerequisite for the existence of MSM effect, because the difference of the magnetic energy is directly related to magnetic anisotropy.

The density of the magnetic energy stored in the sample can be calculated from the magnetisation hysteresis loop (magnetisation vs. field) as:

$$\epsilon = \int \vec{H} \mathrm{d}\vec{M} \tag{2.4}$$

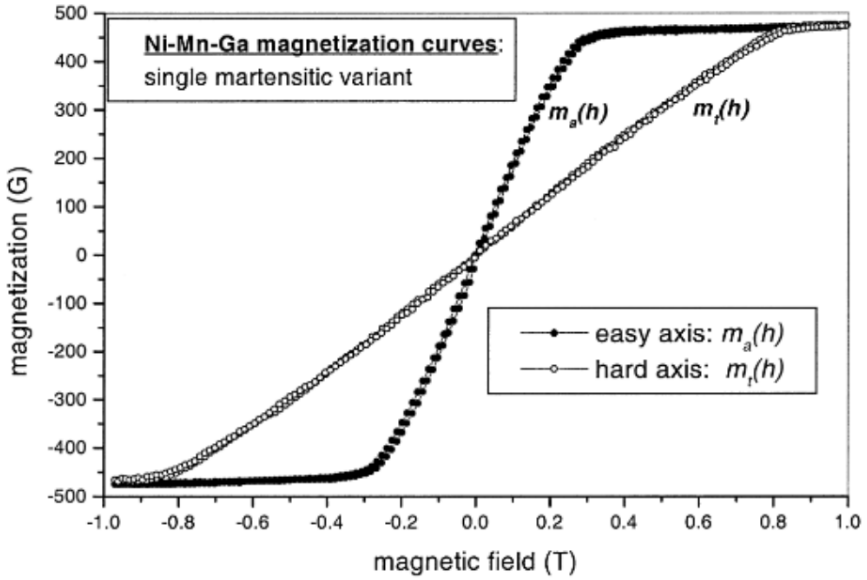

Figure 2.4: Magnetization curves along easy and hard axes of $Ni_{48}Mn_{30}Ga_{22}$ (figure taken from [85])

Then, the magnetic anisotropy could be related to the difference of the energies corresponding to hysteresis loops measured along individual axes (i.e. the area between the easy and hard axis curves in the Figure 2.4).

Clausius-Clapeyron equation

Since the martensitic transformation is the transition of the second kind, we can characterize it with the Clausius-Clapeyron relation. This relation is usually stated as follows:

$$\frac{\mathrm{d}p}{\mathrm{d}T} = \frac{L}{T\Delta v} \tag{2.5}$$

where L is the latent heat, T is the temperature of the transition and $\Delta v = \Delta\rho^{-1}$ is the change in the specific volume (ρ is the mass density). $p\,(T)$ is meant as the coexistence curve of the phases in the $p - T$ phase diagram.

Concerning the magnetisation measurements performed at different magnetic fields, it is more useful to work with Equation 2.5 in the other form [86]:

$$\frac{1}{\mu_0}\frac{\mathrm{d}T}{\mathrm{d}H} = \frac{\Delta M}{L}T \tag{2.6}$$

where H is the applied magnetic field and ΔM is the difference of the saturation magnetisation - in our case the saturation magnetisation M_M of the martensitic and M_A austenitic phase respectively. T now stands here as the transformation temperature at the zero field.

2.2.6 X-ray diffraction

The X-ray diffraction measurements at room temperature were performed on Panalytical X'Pert Pro MRD diffractometer equipped with the Cu X-ray tube,

hybrid monochromator in the incident beam optics, Pixcel 3D detector and Euler cradle allowing the movement, rotation and the tilt of the sample. The X-ray diffraction at low temperatures was measured at the low-temperature diffractometer built on Siemens D500 goniometer. This machine is equipped with Cu X-ray tube, $\Theta - \Theta$ vertical goniometer, 1D Mythen detector and Bragg-Brentano diffraction geometry. The cooling is provided by the closed-cycle He cryostat, allowing the measurements down to 4 K. However, this diffractometer is dedicated mostly for the powder diffraction measurement, since the absence of the tilt axis for the sample makes the alignment of the asymmetric Bragg reflections during the single crystal diffraction measurement quite difficult.

Refinement of lattice parameters

For the diffraction of monochromatic wave on the crystal specimen, the Laue condition has to be fulfilled - the scattering vector has to be equal to a reciprocal vector $\vec{G}_{hkl}$. This condition can be expressed also by the Bragg's law [87, 88]:

$$2d_{hkl} \sin \Theta_{hkl} = \lambda \tag{2.7}$$

where d_{hkl} is the interplanar distance of the outline of crystallographic planes with indices hkl, λ is the wavelength of the used X-ray radiation and Θ_{hkl} is the Bragg angle of the crystallographic planes hkl. It can be shown that the angle between the incident and the diffracted beam is equal to 2Θ. The advantage of the Bragg's law 2.7 is the direct relation of the angular positions 2Θ of measured diffraction peaks with the geometry of the unit cell. That is expressed here by d_{hkl} which has a connection to the lattice parameters.

To refine lattice parameters, one has to fit the profiles of the measured diffractions to find their 2Θ positions and then solve the system of equations 2.7 with corresponding diffraction indices. However, the obtained values for 2Θ angles should be corrected because of the experimental systematic shifts as:

$$2\Theta = 2\Theta_{exp} + \Delta^{2\Theta}_{zero} + \Delta^{2\Theta}_{sycos} \tag{2.8}$$

where $2\Theta_{exp}$ is the experimentally obtained value, $\Delta^{2\Theta}_{zero}$ is the offset of the 2Θ motor of the diffractometer and $\Delta^{2\Theta}_{sycos}$ expresses the correction corresponding to the vertical shift of the sample from the goniometer axis. For the measurement of the asymmetric diffraction ($\omega \neq \Theta$, where ω is the incident angle) in the coplanar geometry it can be derived:

$$\Delta^{2\Theta}_{sycos} = \operatorname{sgn}(S) \arccos\left(\sqrt{1 - \frac{S^2}{4}\left[\sin(2\Theta - \omega)\cot\omega + \cos(2\Theta - \omega)\right]^2}\right) \tag{2.9}$$

where $S = \frac{2s}{R}$, R is the radius of the goniometer and s is the vertical shift from the goniometer axis. The whole derivation is shown in Appendix A. For the symmetric case ($\Theta = \omega$) the Equation 2.9 transforms into the form $\Delta^{2\Theta}_{sycos} = S\cos\Theta$ which is well used for the powder diffraction and can be found for example here [89].

Corrections for integrated intensity

Following from the kinematical diffraction theory, the integrated intensity of Bragg reflection hkl obtained from the diffraction measurement is proportional to the structure factor and angularly dependent corrections. We can write:

$$I_{hkl}^{integrated} \sim |F_{hkl}|^2 \cdot S \cdot A \cdot L \cdot P \cdot E_{hkl} \tag{2.10}$$

where F_{hkl} is the structure factor, S is the irradiated area of the sample A is the absorption correction, L is Lorentz correction, P is the polarisation correction and E_{hkl} is the correction for the primary and secondary extinction. S and A can be easily computed, since they depends on the known diffraction geometry. P corresponds to the polarisation of the primary beam and can be calculated as $P = \frac{1+\cos\Theta_M \cos 2\Theta}{1+\cos\Theta_M}$, where Θ is Bragg angle and Θ_M is the Bragg angle characteristic for the crystal in the monochromator.

The structure factor F_{hkl} depends on the material and its structure:

$$F_{hkl}\left(\vec{G}_{hkl}, E, T\right) = \sum_n \mathcal{F}_n = \sum_n f_n\left(\vec{G}_{hkl}, E\right) e^{-M_n(\vec{G}_{hkl},T)} e^{2\pi i \vec{G}_{hkl}\cdot\vec{r}_n} \tag{2.11}$$

where G_{hkl} is the diffraction vector, T is the temperature, E is the energy of the incident X-ray beam, f_n is the atomic form-factor and r_n the position corresponding to the n-th atom in the unit cell. M_n is the correction for temperature due to the thermal fluctuations of the atoms.

In Equation 2.10, the most difficult correction to deal with is E_{hkl}. The extinction is an effect following from the dynamical theory of diffraction. It has been found out that kinematical theory works well for the crystals with the high number of defects, because it neglects the multiple scattering inside the sample and the following interference of the beams. For the purpose of further study it is necessary to work with the mosaic crystal, where the sample is composed of the mutually slightly misoriented mosaic blocks, where the structure of each block is considered as ideally perfect [87, 90].

The primary extinction then reflects the intensity loss during the diffraction at different planes in one mosaic block - each scattering introduces the phase shift of $\frac{\pi}{2}$, therefore the interference of the waves differing by even number of scattering leads to the intensity loss. The primary extinction is negligible, when the blocks are sufficiently small. Secondary extinction is responsible for the decrease of the intensity caused by the mutual misorientation of the mosaic blocks. The correction for the secondary extinction can be neglected when the misorientation of the blocks is sufficiently large.

To evaluate the extinction correction, it is necessary to choose an appropriate physical model. The simplest approach is to take the spherical crystal with the spherical blocks [91].

$$E_{hkl} = y_p y_s \tag{2.12}$$

$$y_i = \left(1 + 2x_i + \frac{A_i(\Theta)x_i^2}{1 + A_i(\Theta)x_i}\right)^{-\frac{1}{2}} \tag{2.13}$$

$$x_i = \frac{3}{8}\frac{r^2}{\Lambda_{hkl}^2}, \qquad x_s = \frac{3}{8}\frac{rR}{\Lambda_{hkl}^2}\frac{1}{1+\frac{r}{\lambda}\frac{\sin\Theta}{g}} \tag{2.14}$$

where r is the radius of the blocks, R is the radius of the crystal, Λ_{hkl} is the extinction length for the Bragg reflection hkl, λ is the wavelength of the incident beam and g corresponds to the misorientation of the blocks described by the Lorentz distribution function $\frac{2g}{1+(4\pi x g)^2}$. Function $A_i(\Theta)$ and $B_i(\Theta)$ can be approximated [91] by:

$$A_p(\Theta) = 0.20 + 0.45\cos 2\Theta \tag{2.15}$$

$$B_p(\Theta) = 0.22 - 0.12\,(0.5 - \cos 2\Theta)^2 \tag{2.16}$$

$$A_s(\Theta) = 0.025 + 0.285\cos 2\Theta \tag{2.17}$$

$$B_s(\Theta) = 0.15 - 0.2\,(0.75 - \cos 2\Theta)^2\,, \qquad \cos 2\Theta > 0 \tag{2.18}$$

$$B_s(\Theta) = -0.45\cos 2\Theta, \qquad \cos 2\Theta < 0 \tag{2.19}$$

The case of asymmetric extinction correction can be obtained in the sense of ellipsoidal crystals, blocks and distribution function for misorientation. The derivation in [92] leads to the effective values of r, R and g for the individual Bragg reflections.

$$r' = \frac{1}{\sqrt{\vec{u}_1^{\top}\mathcal{E}_r\vec{u}_1}} \tag{2.20}$$

$$R' = \frac{1}{\sqrt{\vec{u}_1^{\top}\mathcal{E}_R\vec{u}_1}} \tag{2.21}$$

$$\eta' = \frac{1}{\sqrt{\vec{D}^{\top}\mathcal{E}_\eta\vec{D}}} \tag{2.22}$$

$$g' = \frac{1}{\pi\eta'} \tag{2.23}$$

where $\vec{u}_0$ and $\vec{u}_1$ are the normalized directional vectors of the incident and exit beam with respect to the sample and $\vec{D} = \vec{u}_0 \times \vec{u}_1$ is the vector perpendicular to the scattering plane. $\mathcal{E}_r$, $\mathcal{E}_R$ and $\mathcal{E}_\eta$ are the matrix representations of the ellipsoids corresponding to the crystal shape, the shape of mosaic blocks and the misorientation distribution function - i.e. matrices with principal values $\frac{1}{a_i^2}$, where a_i are the lengths of the semi-axes.

Ratio between $L2_1$ and $B2'$ content

For the evaluation of the $L2_1/B2'$ content ratio, we need to compute the structure factor 2.11 with the consideration of the $L2_1$ and $B2'$ unit cells (see Figures 1.1 and 1.2). The structure of the $L2_1$ ordered unit cell is close to the diamond, since it consists of the four interpenetrating face centered cubic (*fcc*) unit cells. This leads to the conditions for the intensity of Bragg reflections:

- the whole structure is *fcc*, therefore only Bragg reflections hkl with the indices all even or all odd are allowed
- Bragg reflections with $h + k + l \neq 4n, n \in \mathbb{N}$ have a low intensity, due to the similarity of the structure with the diamond

In the B2′ ordered unit cell, the atoms Y and Z (see the Section 1.1.2) become equivalent. This leads to a higher symmetry of the structure and the Bragg reflections with all indices odd are extinct. Therefore, we can connect the $L2_1/B2'$ content ratio with the ratio of the structure factors as:

$$\rho = \frac{\left(\frac{|F_{hkl=odd}|^2}{|F_{hkl=even}|^2}\right)_{exp}}{\left(\frac{|F^{L2_1}_{hkl=odd}|^2}{|F^{L2_1}_{hkl=even}|^2}\right)_{theor}} \tag{2.24}$$

where *theor* means theoretically calculated from Equation 2.11 and *exp* means calculated from the experimental data with the use of Equation 2.10. According to Equation 2.24, $\rho = 1$ then corresponds to the fully $L2_1$ ordered structure and $\rho = 0$ to the sample with B2′ ordering only. The parameters for the extinction correction E_{hkl} should be evaluated from Bragg reflections with the indices all even, since the corresponding $|F_{hkl=even}|^2$ is the same for $L2_1$ and B2′ ordering.

Structure modulation

The simplest case of the harmonic modulation can be described by the introduction of the sinusoidal wave for the modulation of the atomic positions. For the displacement of the n-th atom in the m-th unit cell we can write:

$$\vec{u}^m_n = \vec{U} \sin\left(2\pi\vec{q} \cdot \left(\vec{R}_m + \vec{r}_n\right)\right) \tag{2.25}$$

where $\vec{q}$ is the modulation vector, $\vec{U}$ is the modulation amplitude (when $U = 0$, there is no modulation), $\vec{r}_n$ is the position of the n-th atom in the unit cell and $\vec{R}_m$ is the vector pointing to the m-th unit cell. When we know the basic structure of the material, we can evaluate the $\vec{q}$ directly from the 2Θ positions of the satellite maxima. Introduction of the modulation wave 2.25 leads to the change of the contribution of individual atoms to the structure factor 2.11:

$$\mathcal{F}_n\left(\vec{G}_{hkl}, p\right) = f_n\left(\vec{G}_{hkl} + p\vec{q}\right) e^{-M_n(\vec{G}_{hkl}+p\vec{q},T)} e^{2\pi i \vec{G}_{hkl}\cdot\vec{r}_n} J_p\left(2\pi\left(\vec{G}_{hkl} + p\vec{q}\right)\cdot\vec{U}\right) \tag{2.26}$$

where p is the satellite order with respect to the main maximum hkl and J_p is the Bessel function of the p-th order. Therefore, the amplitude $\vec{U}$ can be obtained from the fit of the satellite intensities. However, more complex cases of modulation waves, such as a harmonic wave with higher order or a zig-zig modulation (as in Figure 1.3b), can be treated only by introducing a big unit cell with sufficiently large volume, where we distort the atomic positions in the desired manner and compute the structure factor from this big set of atoms.

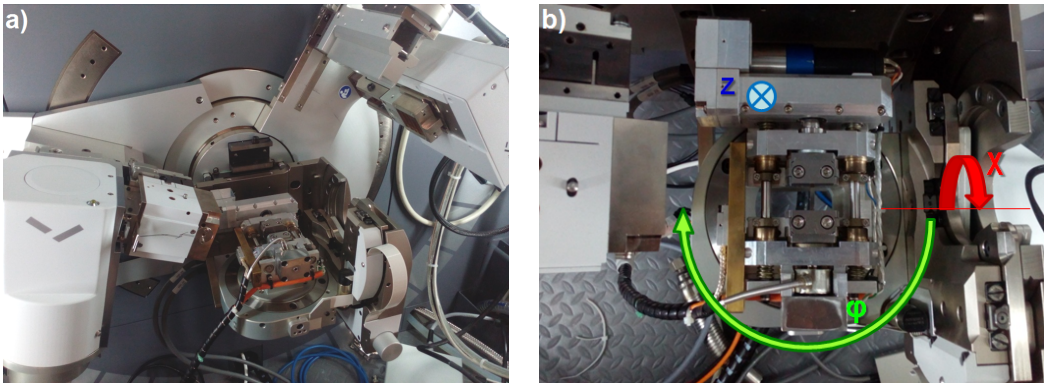

Figure 2.5: **a)** The photo of tensile stage mounted inside the diffractometer, **b)** Possible movements of the sample holder. The rotations are limited due to the stage dimensions to $\varphi \in [-20, 5]$ deg and $\chi \in [-3, 3]$ deg.

X-ray diffraction in-situ in tension

To study possible force induced reorientation (see Section 1.2) by the means of X-ray diffraction we performed the diffraction measurement in-situ in tension. For this purpose, we mounted the tensile stage (possible load up to 4 kN) inside the Panalytical Empyrean diffractometer equipped with Cu X-ray tube, hybrid monochromator in the incident beam optics, and GaliPix 3D detector on the diffracted beam. The sample cannot be cooled in this experimental arangement, therefore the measurement needed to be performed at room temperature and the off-stoichiometric Ni_2MnGa with martensitic phase at room temperature was a basic prerequisite for the experiment. The measurements were done on the sample N50M28G22 and N50M28G22$_{RC}$ prepared additionally by Ross Colman.

The photo of tensile stage mounted inside the diffractometer is shown in Figure 2.5a. It needs to be mentioned that we are limited in the movement and rotations of the sample due to the stage dimensions (indicated in Figure 2.5b). The φ rotation is limited to the range of $[-20, 5]$ deg and the χ tilt cannot be bigger than ± 3 deg. This fact may cause difficulties when aligning the Bragg reflections for various φ.

The best sample shape for a tensile experiment is the dog bone - the deformation is confined to the narrow center region and the probability of fracture occurring at the ends of the specimen is reduced. Optimally, the dog bone shaped sample needs to be several centimeters long. However, since we need to work with single crystalline sample, the preparation of the specimen of such dimensions could be difficult. For that reason, the first attempts of the measurement were performed on the sample N50M28G22 which had the shape of cca 2 cm long. The dog-bone shaped sample was manufactured additionally as well from the single crystalline ingot N50M28G22$_{RC}$. Therefore in summary, the three following options were tested concerning the sample shape and its attachment in the stage:

1. **the clamps** - the sample was held by the clamps on its ends (see Figure 2.6a)

2. **the glue** - the ends of the sample were glued to the steel plates which were held by the clamps (see Figure 2.6b)

3. **the dog-bone shape** - the sample was manufactured to the dog-bone shape and placed on the special holders held by the clamps (see Figure 2.6c)

The individual attachment options are discussed in detail in Chapter 6 together with all results leading from the tensile experiment.

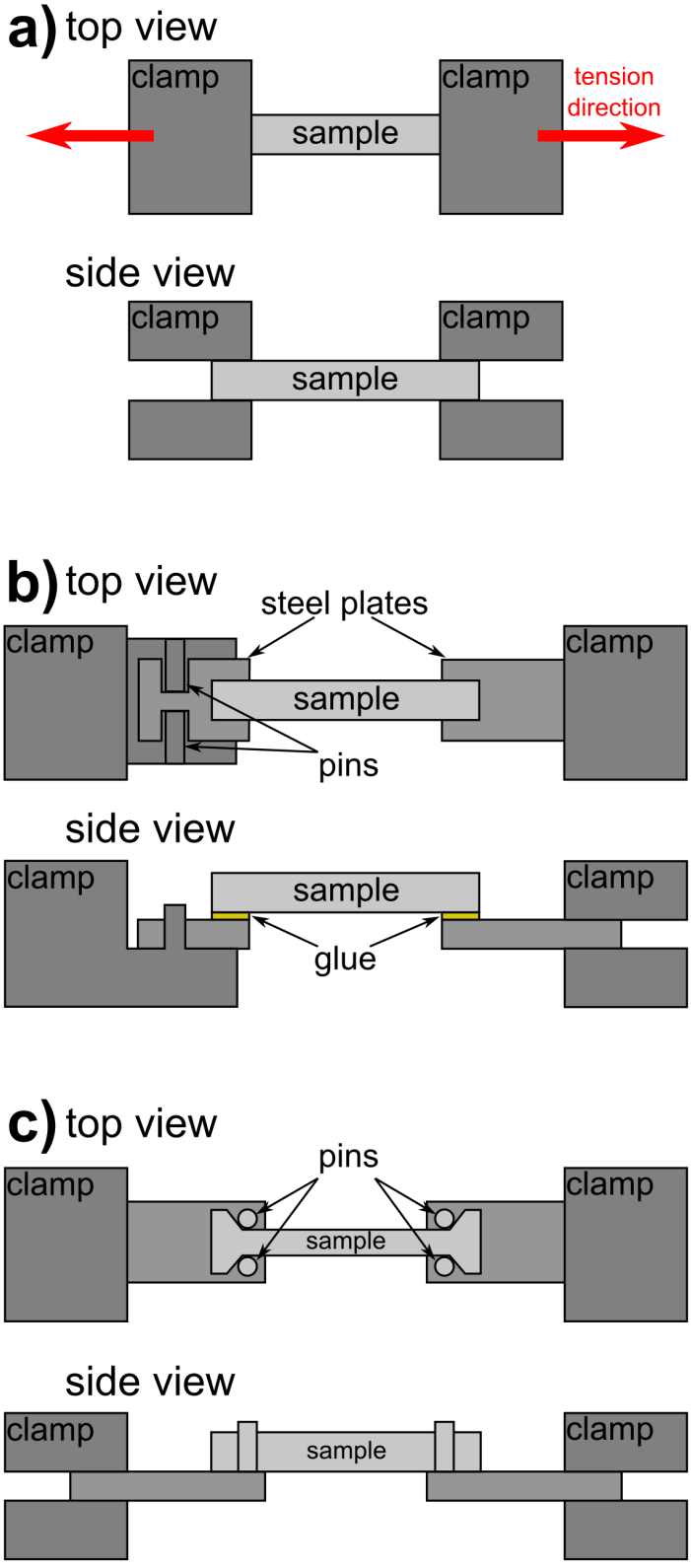

Figure 2.6: Tested sample attachments **a)** sample held directly by the clamps, **b)** sample glued on the steel plates, **c)** dog-bone shaped sample

3. Samples preparation and basic characterisation

This chapter will be dedicated to the basic characterisation of prepared samples and also to the comparison of the single crystals resulting from Bridgman and floating zone method. The part of the presented results was published in the Journal of Alloys and Compounds [51].

3.1 Laue diffraction

For the characterisation and further orientation of the single crystals by Laue diffraction, the specimens were cut from the middle part of the as grown ingots. The measured lauegrams shown in Figure 3.1 for samples NMG and NMG_{FZ} confirm that grown samples are single crystals and that they grow along different crystallographic directions depending on the used preparation method. The crystal from Bridgman method grew with the [111] crystallographic direction parallel to the growth direction whilst the crystal from floating zone grew with the growth direction parallel to [100]. This is very important feature since [100] orientation is favourable for MSM effect [4, 5, 6, 93]. Jiang et al.[94] also reported [100] orientation for Ni_2MnGa single crystal grown the floating zone method. It needs to be also mentioned that orientations presented here were achieved without use of any oriented single crystalline seed.

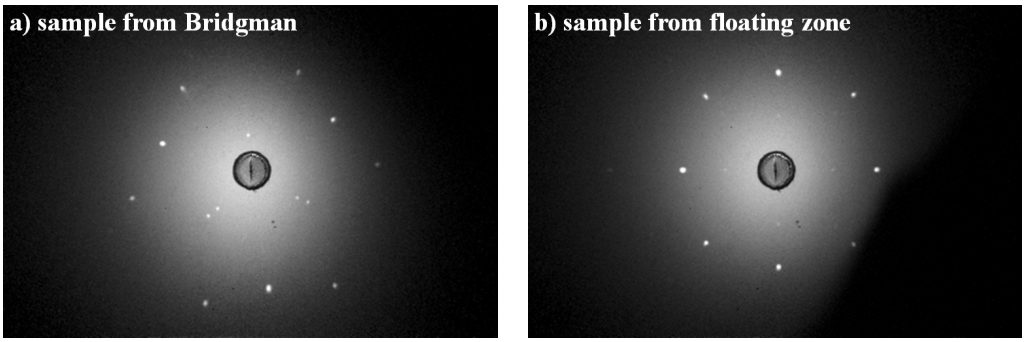

Figure 3.1: Lauegrams of the resulting single-crystals NMG and NMG_{FZ}. Plane of the pictures is perpendicular to the direction of growth. **a)** Sample from Bridgman, three-fold symmetry corresponding to the center 111, **b)** sample from the optical furnace, four-fold symmetry corresponding to the center 100.

3.2 Electron microscopy and XRF

The electron microscopy revealed the unwanted issue of the usage of boron-nitride crucibles during the single crystal growth by Bridgman method. The micrographs from the electron microscope in Figure 3.2 illustrate the surface topography of the specimen cut from the middle part of NMG and NMG_{FZ} ingots. The polished surface of the NMG sample contains several perpendicularly oriented grooves.

Previous study of Ni_2MnGa alloys doped with boron[95] showed similar surface disruptions. Because the melt was in contact with the boron-nitride crucible during the growth in Bridgman method, some amount of boron might diffuse into the material forming precipitates and causing the cracks. According to several other studies, when boron diffuses inside the material, it creates new phases which nucleate along the defects and grain boundaries.[95, 96] The precipitate might be τ-boride $Ni_{20}Ga_3B_6$ [97] with Ni-Ga interatomic distances sharply different from that of Ni_2MnGa. The surface grooves or cracks are the result of this mismatch on the boundaries of these phases. In contrast there are no grooves in the sample from the FZ which was grown without crucible and its surface seems to be grooveless (Figure 3.2). Moreover, in the preparation by Bridgman method we change the boron-nitride crucible to Al_2O_3 crucible and no grooves were observed in the prepared single crystals.

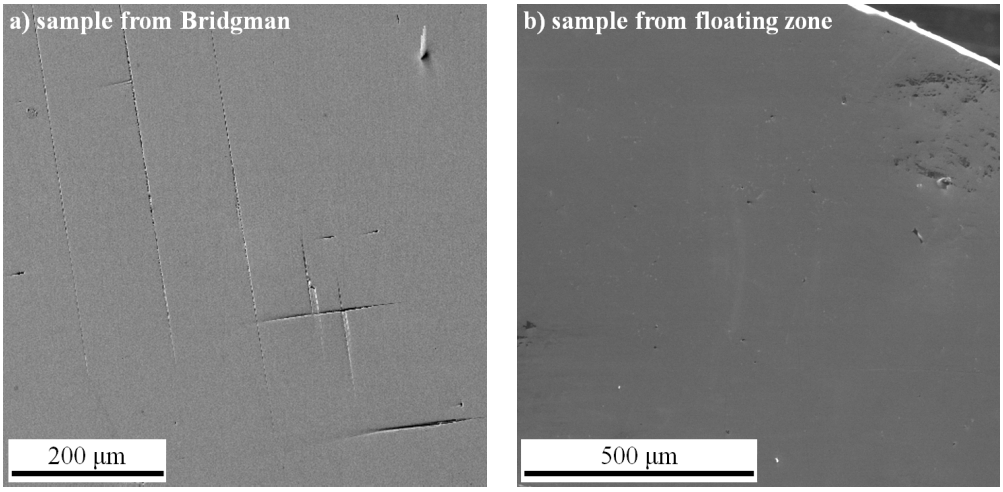

Figure 3.2: Surface topography obtained by the secondary electron contrast in SEM. **a)** The sample from Bridgman method, **b)** the sample from the floating zone.

To study the composition and the homogeneity of the prepared single crystals, the EDX measurements were performed. The EDX maps and linescans in Figures 3.3 provide the comparison of the composition distribution in the samples NMG and NMG_{FZ}. In the NMG_{FZ} single crystal before annealing, the compositional inhomogeneity is apparent occurring in the form of islands (Figure 3.3c). The diameters of these islands are 80-100 μm. The line scan across these islands shown in Figure 3.3d clearly shows that the variation is mostly in Mn and Ga, i.e. the Mn excess is compensated by Ga deficiency and vice versa, while Ni content is almost constant across the cut.

To reveal the three-dimensional shape of the inhomogeneity islands a cut at plane perpendicular to abovementioned observed surface and parallel to the direction of the growth was made. Figure 3.4 shows stripes suggesting the columnar shape of these composition islands. These columns can penetrate through the whole volume. The differences between Mn and Ga content in the columns are about one percent with respect to the surrounding area. After annealing, the compositional inhomogeneities disappeared and composition map of the annealed NMG_{FZ} sample (Figure 3.3e) indicated a similar homogeneity as the sample NMG from Bridgman method (Figure 3.3a).

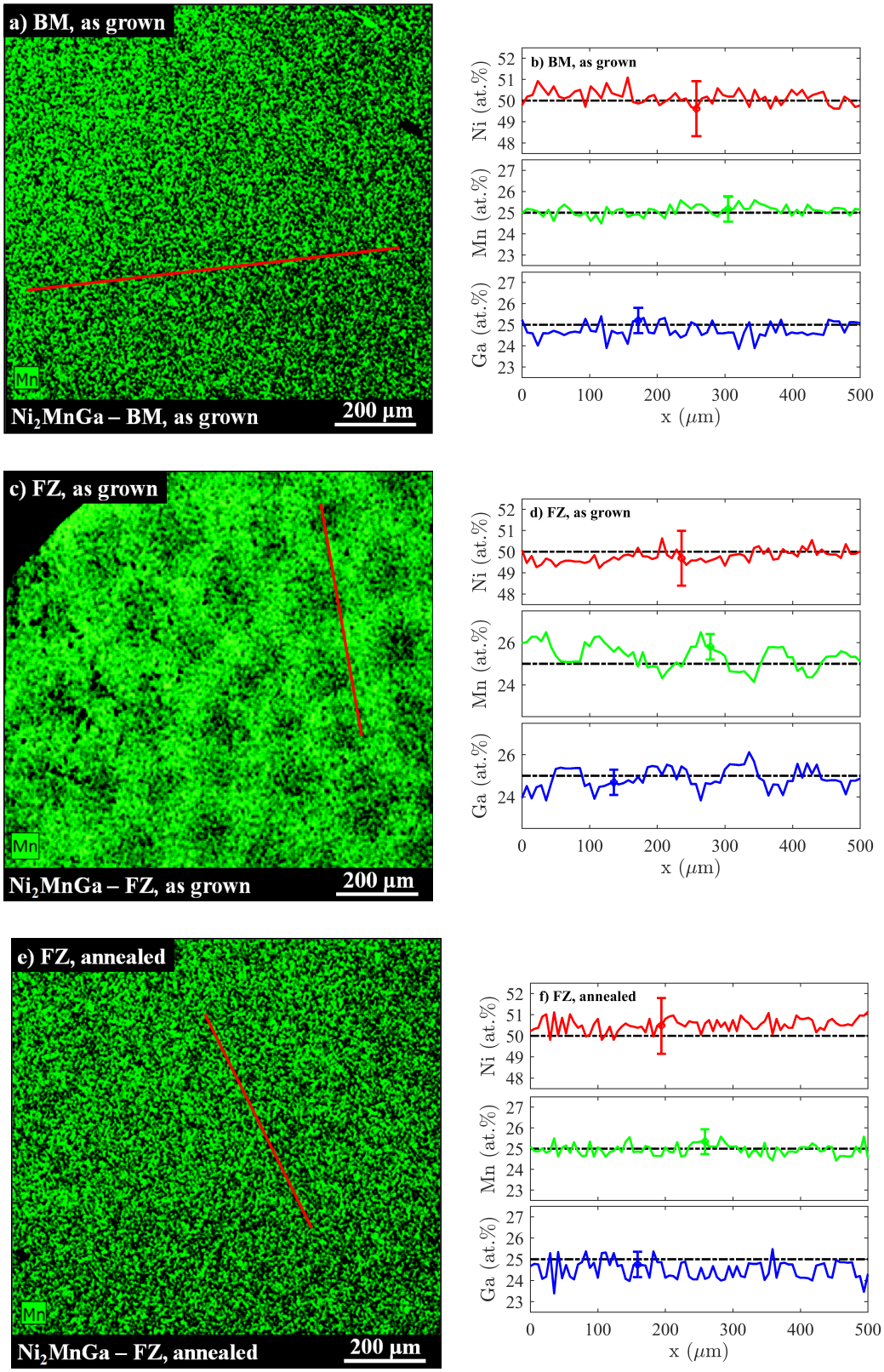

Figure 3.3: Composition maps of Mn and linescans obtained from EDX. Green pixels – Mn excess, black pixels – Mn deficiency. **a,b)** As grown NMG sample (from Bridgman), **c,d)** as grown NMG_{FZ} sample (from floating zone), **e,f)** annealed NMG_{FZ} sample. Planes of the maps are perpendicular to the direction of growth. Linescans in **(b)**, **(d)** and **(f)** are measured along the red lines highlighted in maps. Error bars indicating average uncertainty for the each element are marked.

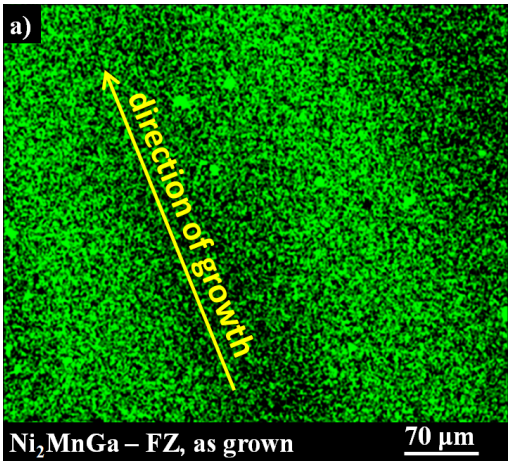

Figure 3.4: Composition map of Mn obtained from EDX on as grown sample from floating zone. Plane of the map is parallel to the direction of growth.

Time for the homogenization annealing can be estimated from the known diffusion parameters. We used the diffusion coefficients from [98] and solve the 1D Fick's law at 1000°C with the initial state with one 80 μm inhomogenity found in FZ sample (as in Figure 3.3c). We estimated that our sample should be annealed for 2 days to homogenize the spatial distribution of Mn. In contrast, the homogenization annealing on the sample from Bridgman may be redundant, as the sample composition determined by EDX was already homogeneous.

The annealed NMG sample (figure not shown) from Bridgman exhibited the same homogeneity as the as grown sample. This is the consequence of the preparation procedure - the single crystal growth by Bridgman method in the vertical induction furnace was slow (0.5 mm/h) in comparison to the floating zone (80 mm/h). Therefore, newly grown part of single crystal near the hot zone stayed several hours at temperatures close belove the melting point and it was already partly homogenized.

The EDX measurement on the samples with indium revealed the necessity of a longer time for a homogenisation annealing. There are EDX maps in Figure 3.5 for the sample NMGIn10 measured for the as grown sample, the sample after 2 days of homogenisation and 5 days of homogenisation. It can be clearly seen that the indium is inhomogeneously distributed in the sample right after the single crystal growth (Figure 3.5j). After 2 days of a homogenisation annealing, the spatial distribution of Ni, Mn and Ga is sufficiently homogenized. However, 2 days of the homogenization annealing at 1000°C used previously for stoichiometric Ni_2MnGa [51] (and used to dissolve the Mn inhomogeneities mentioned above) was still not enough to homogenize the indium distribution. The indium atoms are much heavier than Ni, Mn and Ga, therefore it is more difficult for them to diffuse through the material. For that reason we performed the homogenization annealing for 5 days. The resulting EDX map in Figure 3.5l shows that indium spatial distribution was already successfully homogenized.

The measurement along the as grown single crystalline ingots revealed the possibility of macrosegregation of individual elements. The results for the sample NMGIn10 (Bridgman method) and NMG_{FZ} (floating zone) are shown in Figures 3.6a and 3.6b. The black dashed lines correspond to the mean compositions

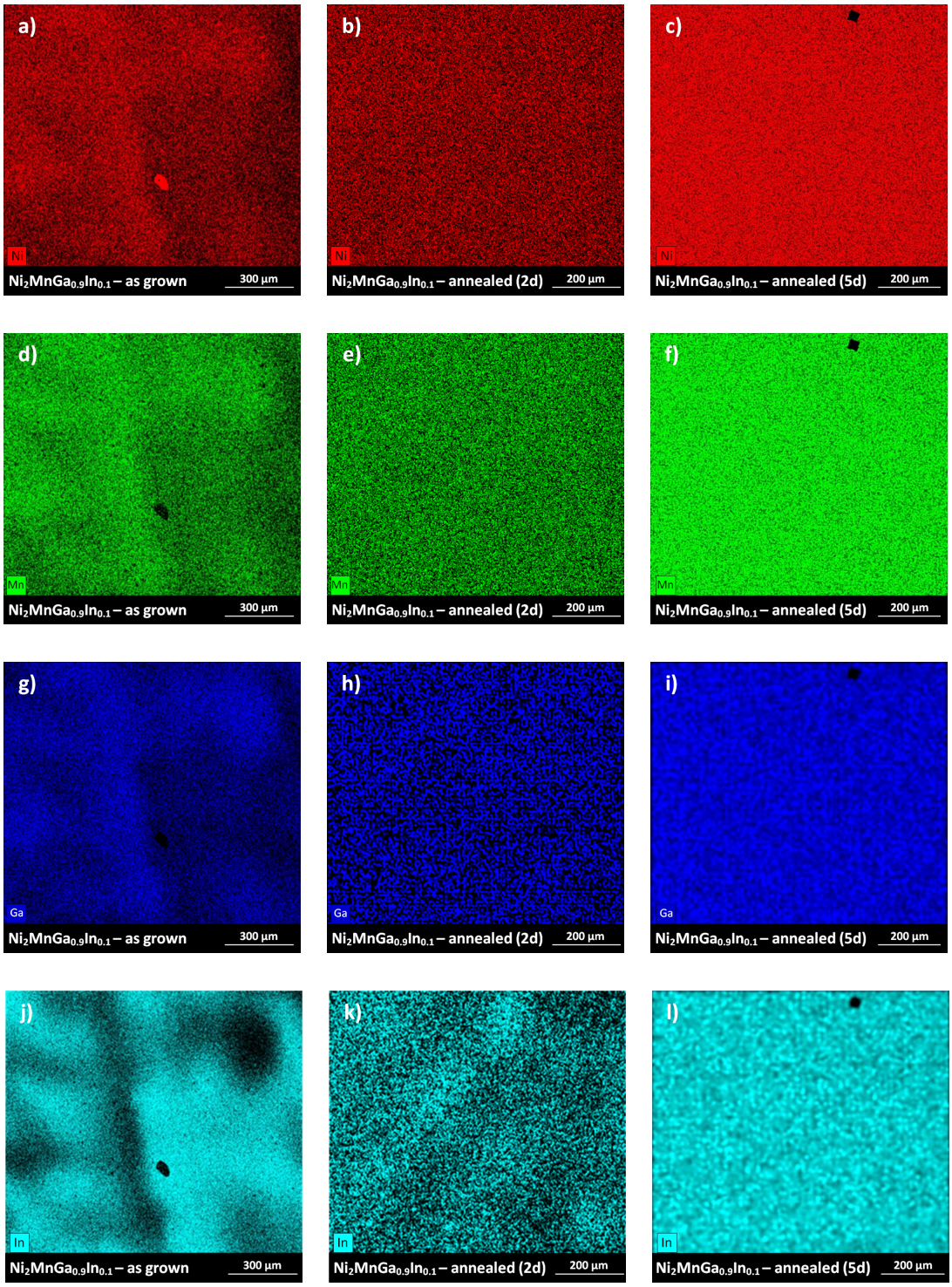

Figure 3.5: Spatial distribution of elements measured by EDX on NMGIn10 sample. **a,d,g,j)** as grown, **b,e,h,k)** after 2 days of homogenization, **c,f,i,l)** after 5 days of homogenization.

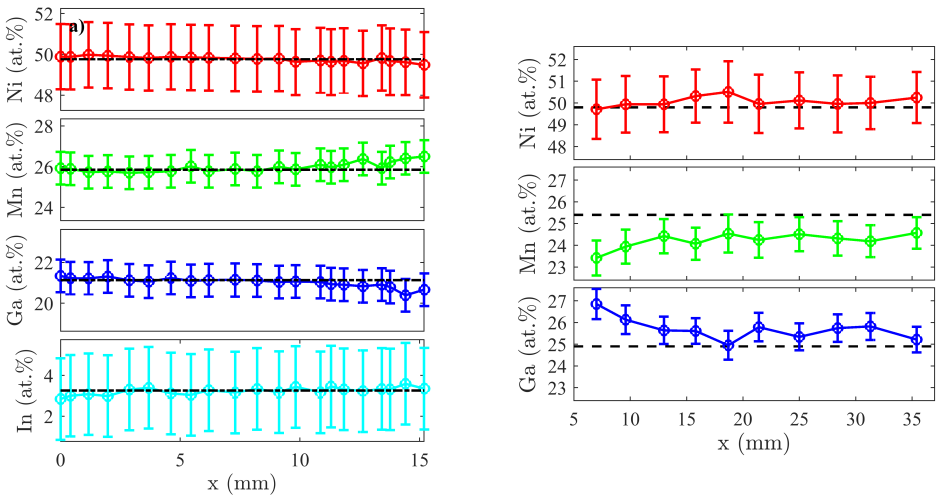

Figure 3.6: The composition of the as grown single crystals measured by EDX along the ingot. The zero on the horizontal axis corresponds to the ingot neck (the growth start). **a)** NMGIn10 sample, **b)** NMG_{FZ} sample. The black dashed lines correspond to the mean compositions shown in Table 3.1.

shown in Table 3.1. The error bars for individual element concentrations are computed as $\sigma_i = \sqrt{\sigma_{stat}^2 + \sigma_{sys}^2}$, where σ_{stat} are the errors obtained from the fit of EDX spectra and σ_{sys} is the relative error of 2 % (the usual estimation for the systematic error of EDX). However, 2 % of relative error corresponds to the major contributory elements. Therefore, we estimated the error for indium content as $\sqrt{\sigma_{Ni}^2 + \sigma_{Mn}^2 + \sigma_{Ga}^2}$, where σ_i are the concentration errors of the other elements in the compound. The dependence in Figure 3.6a shows that the composition of the sample NMGIn10 along the as grown ingot is constant in the range of the error bars. However, there is an evidence of a macrosegregation, especially for the Mn and Ga, since their concentrations differ at the start and at the end of the ingot. Opossitely, the macrosegregation is more evident for the sample NMG_{FZ} where the relative change of Mn and Ga concentration along the ingot is about 2 at.%. Moreover, the composition of the as grown sample NMG_{FZ} (Figure 3.6b) seems to be slightly different inside the sample and on the border, since the EDX measurement shown in Figure 3.6b was performed on the polished surface of the as grown ingot and the average composition corresponding to the dashed lines was measured on the cross-section from the middle of the ingot.

The single crystals prepared by Bridgman method and homogenized for 5 days were taken for the further analysis - the specimens were cut from the middle part of the ingots. For each studied sample the composition was quantified by EDX at 10 different points and averaged to obtain the mean composition. The results showed out that it is hard to reach the exact target composition. Despite of extra Mn and Ga added before the preparation, some of the resulting compositions are several percents off from the nominal values. Moreover, there is no significant trend in the offsets of the resulting compositions, although the preparation process is the same for all samples grown by Bridgman method. The composition of the several samples was additionally checked by XRF (the same pieces of the prepared samples). All resulting values are summarized in Tables 3.1 and 3.2.

label	nominal composition	x_{nom}	composition from EDX	x_{EDX}
NMG, ag*	$Ni_{50}Mn_{25}Ga_{25}$	0.000	$Ni_{50.1}Mn_{25.1}Ga_{24.7}$	0.000
NMG	$Ni_{50}Mn_{25}Ga_{25}$	0.000	$Ni_{50.6}Mn_{25.3}Ga_{24.1}$	0.000
NMG_{FZ}, ag*	$Ni_{50}Mn_{25}Ga_{25}$	0.000	$Ni_{49.8}Mn_{25.4}Ga_{24.9}$	0.000
NMG_{FZ}	$Ni_{50}Mn_{25}Ga_{25}$	0.000	$Ni_{50.5}Mn_{25.0}Ga_{24.5}$	0.000
NMGIn2	$Ni_{50}Mn_{25}Ga_{24.5}In_{0.5}$	0.020	$Ni_{49.4}Mn_{26.6}Ga_{23.4}In_{0.6}$	0.025
NMGIn5	$Ni_{50}Mn_{25}Ga_{23.75}In_{1.25}$	0.050	$Ni_{49.8}Mn_{26.5}Ga_{22.4}In_{1.3}$	0.055
NMGIn10	$Ni_{50}Mn_{25}Ga_{22.5}In_{2.5}$	0.100	$Ni_{49.8}Mn_{25.8}Ga_{21.1}In_{3.3}$	0.135
NMGIn15	$Ni_{50}Mn_{25}Ga_{21.25}In_{3.75}$	0.150	$Ni_{50.2}Mn_{26.5}Ga_{19.3}In_{4.0}$	0.172
NMGIn25p	$Ni_{50}Mn_{25}Ga_{18.75}In_{6.25}$	0.250	$Ni_{49.2}Mn_{26.3}Ga_{18.6}In_{5.9}$	0.241
NMGIn50	$Ni_{50}Mn_{25}Ga_{12.5}In_{12.5}$	0.500	$Ni_{51.0}Mn_{25.5}Ga_{10.7}In_{12.8}$	0.545
NMGIn75p	$Ni_{50}Mn_{25}Ga_{6.25}In_{18.75}$	0.750	$Ni_{48.8}Mn_{24.9}Ga_{5.9}In_{20.4}$	0.776
NMGIn_p	$Ni_{50}Mn_{25}In_{25}$	1.000	$Ni_{49.0}Mn_{24.8}In_{26.2}$	1.000

Table 3.1: Comparison of the nominal values of samples composition and the values obtained by EDX. Parameter x corresponds to the labeling $Ni_2MnGa_{1-x}In_x$ and reflects the content of In with respect to Ga and In together, $x = \frac{\text{In}}{\text{In+Ga}}$.
$*$) as grown

label	nominal composition	x_{nom}	composition from XRF	x_{XRF}
NMG	$Ni_{50}Mn_{25}Ga_{25}$	0.000	$Ni_{50.4}Mn_{25.5}Ga_{24.6}$	0.000
NMGIn2	$Ni_{50}Mn_{25}Ga_{24.5}In_{0.5}$	0.020	$Ni_{49.5}Mn_{24.9}Ga_{25.1}In_{0.5}$	0.020
NMGIn5	$Ni_{50}Mn_{25}Ga_{23.75}In_{1.25}$	0.050	$Ni_{50.0}Mn_{25.0}Ga_{23.8}In_{1.2}$	0.050
NMGIn10	$Ni_{50}Mn_{25}Ga_{22.5}In_{2.5}$	0.100	$Ni_{49.9}Mn_{24.4}Ga_{22.4}In_{3.3}$	0.128
NMGIn15	$Ni_{50}Mn_{25}Ga_{21.25}In_{3.75}$	0.150	$Ni_{50.7}Mn_{24.5}Ga_{21.1}In_{3.7}$	0.149

Table 3.2: Comparison of the nominal values of samples composition and the values obtained by XRF. Parameter x corresponds to the labeling $Ni_2MnGa_{1-x}In_x$ and reflects the content of In with respect to Ga and In together, $x = \frac{\text{In}}{\text{In+Ga}}$.

The concentrations in Table 3.1 following from EDX measurement have errors corresponding to the error bars in Figure 3.6. Because of the calibration with the standard, XRF measurement had a higher accuracy than EDX and the values obtained from XRF (if measured) are used in next chapters. The corresponding errors for the concentration of Ni, Mn and Ga are 0.5 at.% However, the indium concentrations obtained by XRF still have a relative error about 40 % due to the low signal of indium peaks in the measured spectra.

3.3 DSC

The DSC measurements were performed to obtain the B2′ →$L2_1$ ordering temperature, which is crucial to know for the samples annealing, and the melting temperature, which is also important for the annealing and for the single crystal growth as well. The measurement has been performed on the samples NMG, NMGIn2, NMGIn5, NMGIn10, NMGIn15, NMGIn25p, NMGIn50, NMGIn75p and NMIn_p to cover the whole composition range with respect to the indium content.

The results of the DSC measurements are shown in Figure 3.7 for the samples NMG, NMGIn25p, NMGIn50, NMGIn75p and NMIn_p. The anomaly corresponding to a melting has a peak-like shape and it is clearly seen, that the indium content monotonically decreases the melting temperature from 1120°C (for NMG) to 950°C (for NMIn_p). However, the multi-peak shape of the melting anomaly measured on the samples NMGIn25p, NMGIn50, NMGIn75p during heating indicates not sufficient chemical homogeneity of these samples. Even thought they were also homogenized by the annealing procedure described in Section 2.1.3, the samples NMGIn25p and NMGIn75p are polycrystals prepared by arc-melting. The samples could contain grains with a slightly different chemical composition which could cause the melting anomaly peak splitting. After remelting, the corresponding anomalies reduced to almost one peak observed during cooling (the melting temperatures were derived from these curves).

The anomaly corresponding to the B2′ →$L2_1$ ordering temperature is much weaker and can be seen in the inset of Figure 3.7 (only the heating cases are shown for the better visibility). The positions of the anomalies are depicted in Figure 3.8 with the polynomial fits of their temperature dependence.

3.4 X-ray diffraction

To obtain the lattice parameters at room temperature and information about the mosaicity, a reciprocal space mapping was performed on the samples NMG and NMG_{FZ} (before and after annealing as well) and on the reference sample $NMG_{AdaptaMat}$ (X-ray diffraction on the samples with indium will be presented in Chapter 5). The reciprocal space maps for several diffractions were measured for each sample (the maps for diffraction 400 are shown in Figures 3.9 and 3.10). Resulting lattice parameters were obtained by the fitting of the system of Bragg equations 2.7 (the same procedure used in [19]) and they are listed in Table 3.3. Their values are very similar to the parameters found in literature, e.g. in [5, 58]. For both preparation methods, the lattice parameters are slightly smaller after

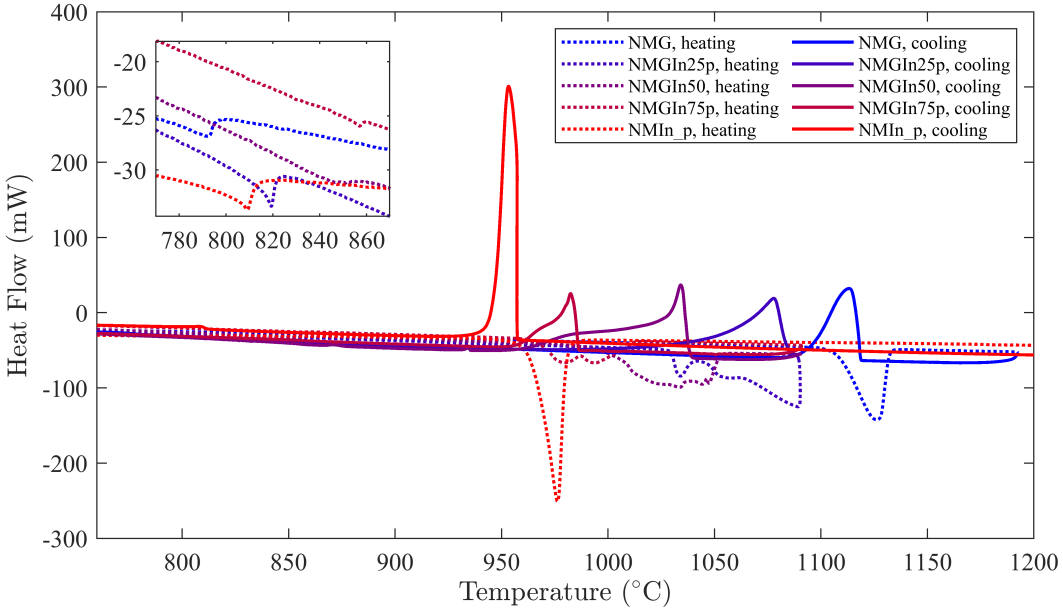

Figure 3.7: The DSC scans measured on the prepared samples. For the better visibility, only the curves measured during heating are shown in the inset.

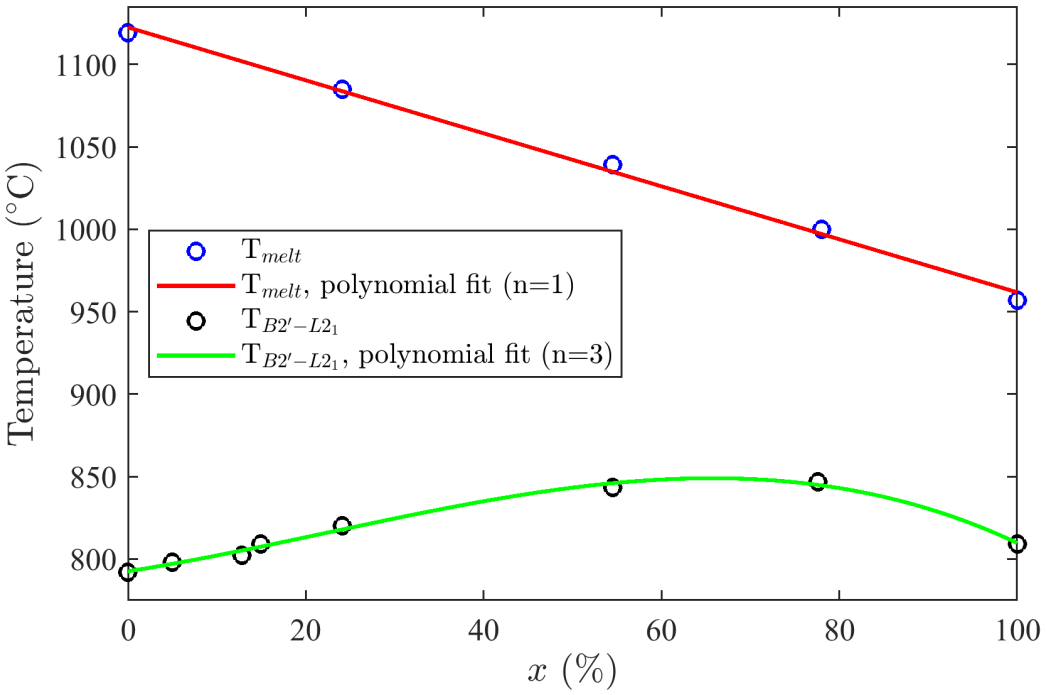

Figure 3.8: The dependence of the melting temperature and the temperature of B2′ →L2$_1$ transition on the indium content

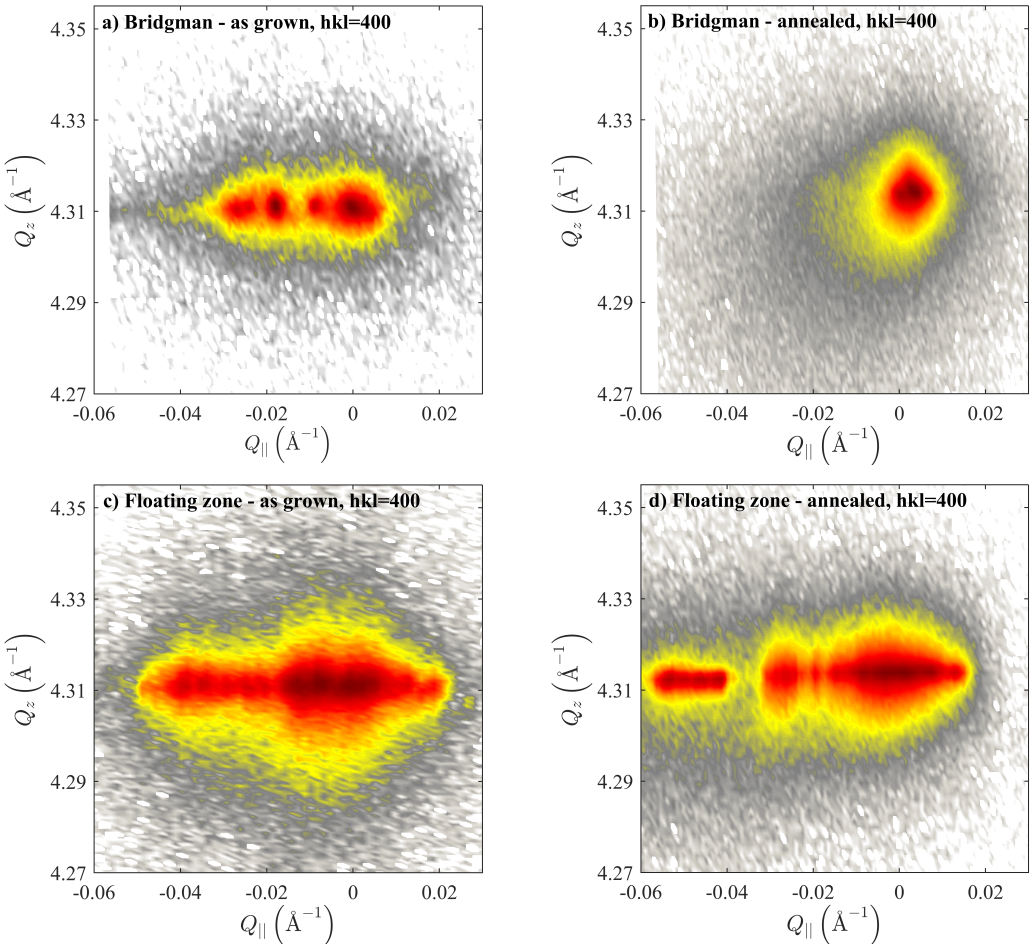

Figure 3.9: Reciprocal space maps of Bragg reflection 400. **a)** NMG, as grown **b)** NMG, annealed **c)** NMG_{FZ}, as grown **d)** NMG_{FZ}, annealed

annealing. As the structure parameters are dependent on composition [58, 99] it may indicate that the ratio between elements changed due to evaporation (mostly Mn) during the annealing. The difference in Mn content can be so small that it cannot be measured by EDX, because the error bar is 1-2 percentage point (Figure 3.6a and 3.6b). The shift of lattice parameters due to assumed deficiency of Mn is corroborated by comparison with the reference sample $NMG_{AdaptaMat}$ having the largest lattice parameter and the largest content of Mn with composition $Ni_{50}Mn_{26}Ga_{24}$ (austenitic phase at room temperature).

The samples mosaicity can be inferred from the reciprocal space maps of 400 diffraction spot shown in Figure 3.9. The stronger the mosaicity is the larger is the spread over the angle of incidence which for the symmetrical diffraction 400 corresponds to the horizontal axis. The mosaic spread in degrees is listed in Table 3.3. Figure 3.9 shows that the mosaic spread in the sample NMG_{FZ} from floating zone is larger than in the sample NMG from Bridgman, but for both preparation methods the mosaic spread is comparable with the reference $NMG_{AdaptaMat}$ (Figure 3.10).

The cuts of diffraction profiles along Q_z are shown in Figure3.11. The full widths at half maximum (FWHM) along Q_z are listed in Table 3.3. The highest FWHM can be seen for the as grown sample NMG_{FZ}. It corresponds to

the spread of lattice parameters which is connected to the composition inhomogeneities observed by EDX (see Figures 3.3c and 3.3d) and the dependence of lattice parameters on the composition mentioned above. The composition of the annealed NMG_{FZ} sample is more homogeneous and the FWHM of diffraction 400 is decreased to a lower value $3.2 \cdot 10^{-3}$ Å^{-1} comparable to the FWHM of diffraction 400 measured on reference sample $3.0 \cdot 10^{-3}$ Å^{-1}.

To probe the structural order the intensity ratios between diffractions with all indices odd and all indices even were measured. Diffractions with all indices odd are allowed in the $L2_1$ ordering and not in the more symmetrical $B2'$ ordering. Structure factors of diffractions with all indices even remain the same in both phases. Experimentally, we can measure integrated intensities which are proportional to the square of the absolute value of structure factor (described in Section 2.2.6). The ratio between the volume content of $L2_1$ and $B2'$ ordering is then evaluated from the Equation 2.24. The parameters of the extinction correction was estimated from the fit of the integrated intensities of the diffraction with all indices even, since their intensity should remain the same in the both types of ordering.

The computed volume ratios of $L2_1$ are listed in the Table 3.3. It has to be mentioned that these values has a deviation about 10 % due to a mosaicity (each block corresponds to different intensity value) and the statistics resulting from the intensity ratio between different pairs of diffractions (111/400, 333/400, 111/620, 513/620, ...). The samples were cut to the same shape and placed in the same orientation, to minimise the effect of extinction in a volume ratios comparison. Because of a bad statistics corresponding to the intensity difference between individual mosaic blocks, the volume ratio ρ for reference sample is not listed in the table, because the following deviation is above 20 %. However, the other values show that the annealing significantly increased the amount of the $L2_1$ in the sample and the annealed sample NMG_{FZ} contains mostly $L2_1$ ordering.

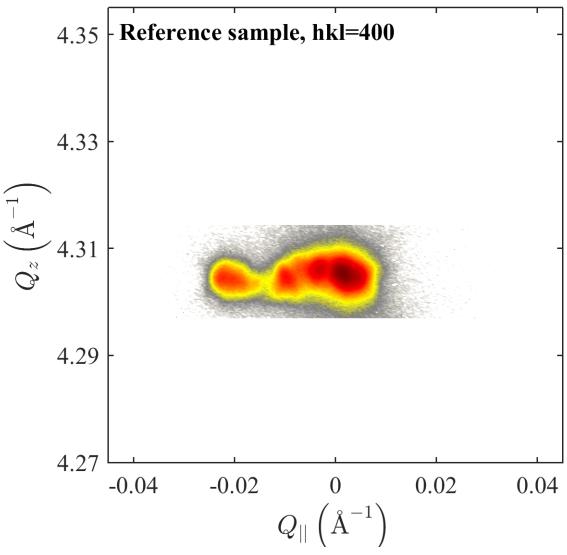

Figure 3.10: Reciprocal space map of Bragg reflection 400 measured on the reference austenitic sample $NMG_{AdaptaMat}$

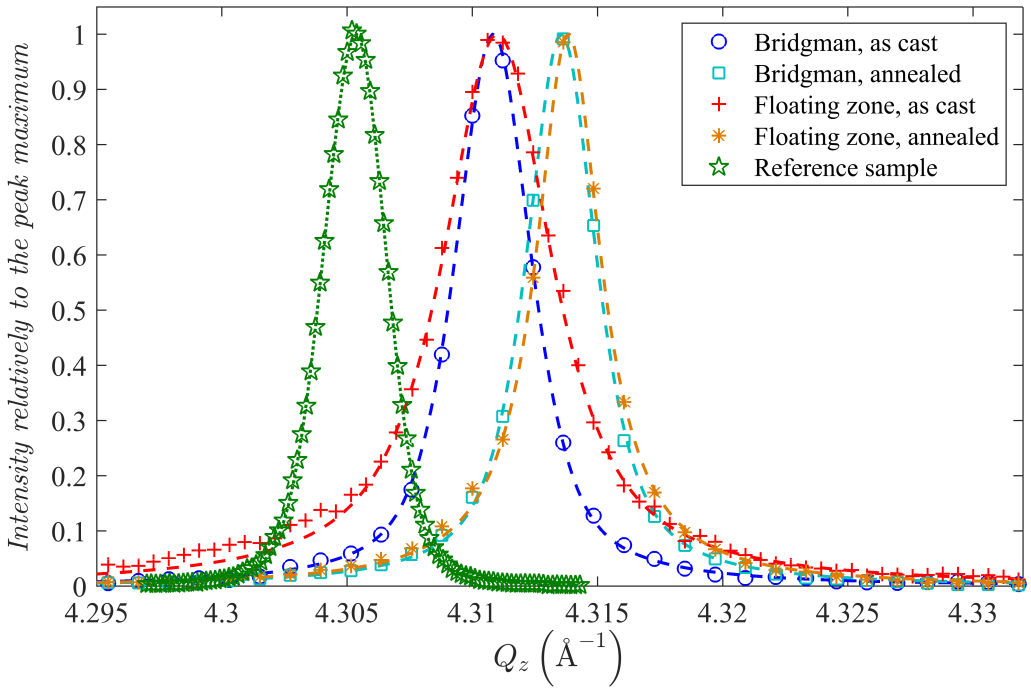

Figure 3.11: Q_z cuts of the diffraction 400 (cuts taken through the highest maxima in the maps in Figures 3.9 and 3.10)

Sample	a (Å)	FWHM$_{Q_z}$ (Å^{-1})	Mosaic spread (deg)	ρ
NMG, as grown $Ni_{50.1}Mn_{25.1}Ga_{24.7}$	5.8284(7)	$3.6 \cdot 10^{-3}$	0.4	0.62
NMG, annealed $Ni_{50.6}Mn_{25.3}Ga_{24.1}$	5.8246(2)	$3.4 \cdot 10^{-3}$	0.1	0.77
NMG$_{FZ}$, as grown $Ni_{49.8}Mn_{25.4}Ga_{24.9}$	5.8283(3)	$5.2 \cdot 10^{-3}$	0.8	0.78
NMG$_{FZ}$, annealed $Ni_{50.5}Mn_{24.9}Ga_{24.5}$	5.8261(6)	$3.2 \cdot 10^{-3}$	1.0	1.00
NMG$_{AdaptaMat}$ $Ni_{50}Mn_{26}Ga_{24}$	5.8375(3)	$3.0 \cdot 10^{-3}$	0.4	-

Table 3.3: Samples identification and average compositions obtained by EDX (see Table 3.1), lattice parameters, FWHM, mosaic spread and the volume ratio ρ of $L2_1$ ordering in the sample (computed from the Equation 2.24 and averaged from the all possible combination of measured diffractions)

4. Measurement of physical properties

4.1 Temperature dependence of electrical resistivity and magnetisation

To detect the temperatures of phase transitions the temperature dependences of the electrical resistivity and of the magnetisation in the applied magnetic field of 0.01 T were measured. The temperature dependences of the electrical resistivity and the magnetisation for all prepared samples are shown in Figure 4.1 and 4.2, respectively. The martensitic transformation is clearly seen in both figures. The temperature of martensitic transformation decreases with increasing indium content and there is no martensitic transformation observed in the samples with the indium content $x > 0.05$. The steep increase of magnetisation at high temperatures during cooling indicates ferromagnetic-paramagnetic transition at Curie temperature (T_C). The pre-martensitic transformation can be clearly visible in magnetisation data as well. The values of the pre-martensitic transformation temperature (T_P) and of T_C were obtained from the first derivatives of the magnetisation curves. The sharp decrease in magnetisation at low temperatures corresponds to the martensitic transformation - the temperature of martensitic transformation T_M was obtained by the tangential method (see Section 1.1.4). All critical temperatures are listed in Table 4.1. The decreasing tendency of the critical temperatures with respect to increasing indium content can be clearly seen from the resulting values.

x_{XRF}	$T_C(K)$	$T_P(K)$	$T_M(K)$
0.000	372.3	246	196
0.020	376.0	230	152
0.050	375.3	215	103
0.128	362.1	177	-
0.149	355.8	150	-

Table 4.1: Critical temperatures of the studied samples. x_{XRF} - indium content, T_C – Curie temperature, T_P – pre-martensitic transformation temperature, T_M – martensitic transformation temperature (see the Section 1.1.4)

It needs to be mentioned that the annealing can have an influence on the transformation temperatures as well. According to [100], the heat treatment can increase the temperature of the martensitic transformation in the order of tens of Kelvins. The heat treatment also decreases the temperature hysteresis of the martensitic transformation. This shift can be associated with the increasing $L2_1$ order in the sample, as it was studied by Santamarta, et al. [76] on similar alloy Ni-Fe-Ga. According to [76], our heat treatment procedure should lead to high $L2_1$ order. However, one can compare the temperature dependence of magnetization measured on the as grown and the annealed sample Ni_2MnGa published in our previous work [51]. The change in the dependences is mostly in the tran-

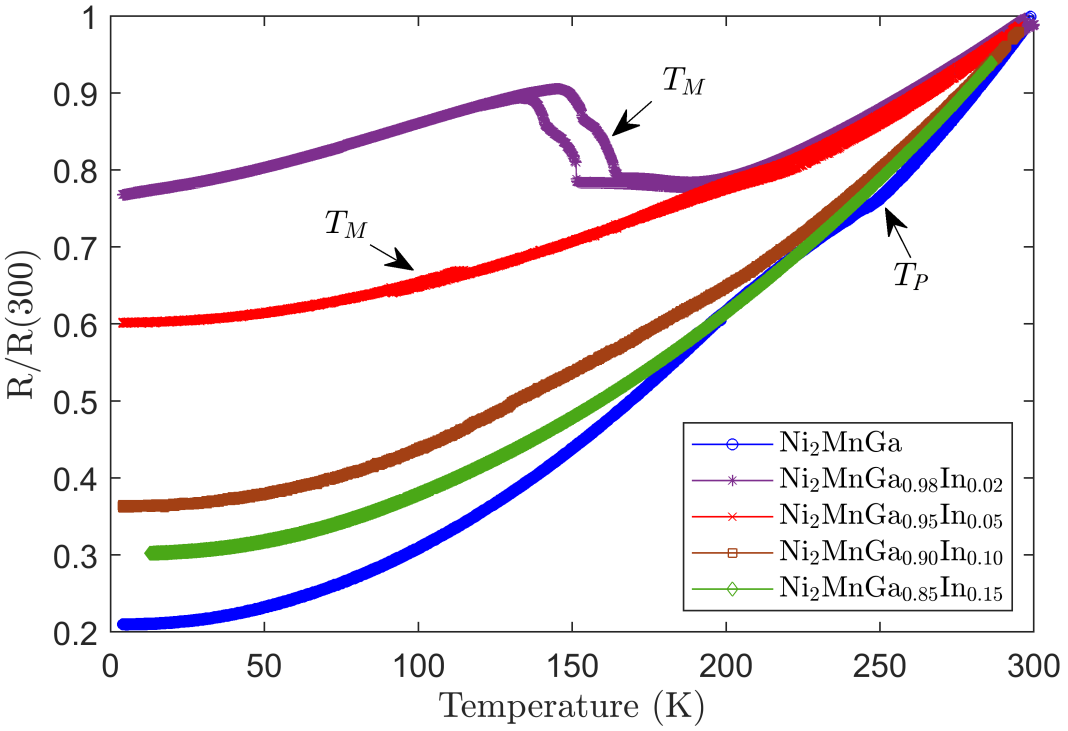

Figure 4.1: The temperature dependence of the electrical resistivity (relatively to the value at 300 K) for the samples with different indium content. The electrical current was oriented along the crystallographic direction [100] in austenite.

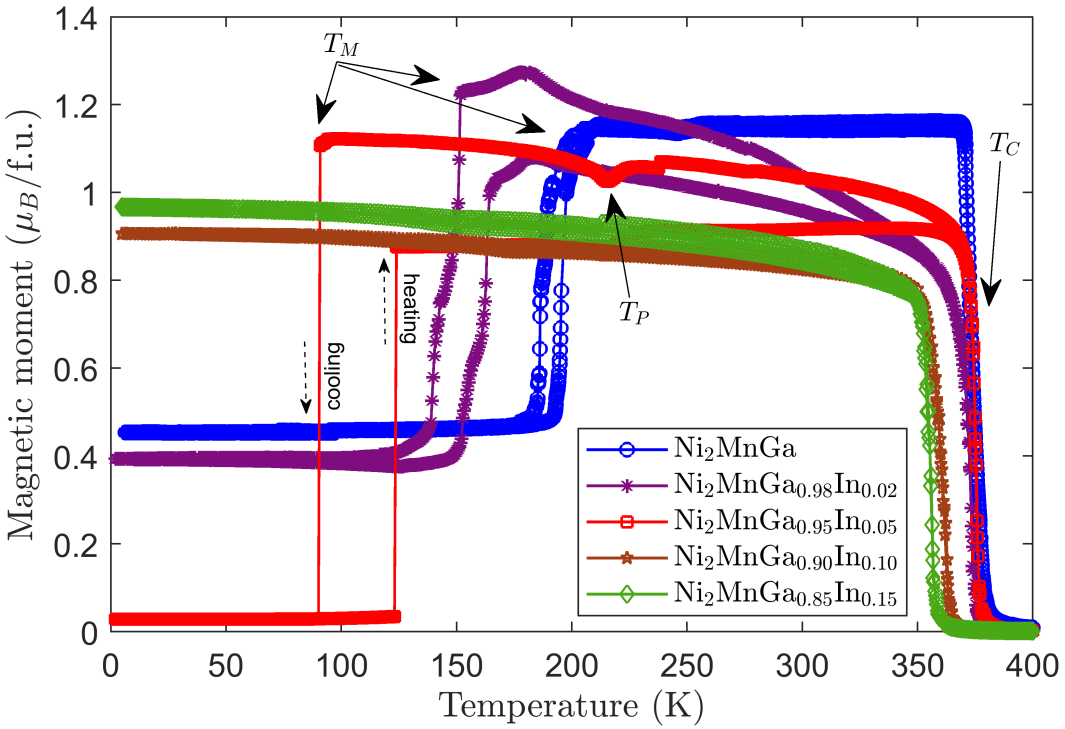

Figure 4.2: The temperature dependence of the magnetisation in the applied magnetic field of 0.01 T for samples with different indium content. The applied field was oriented along the crystallographic direction [100] in austenite.

sition width (because of the homogenization) and the increasing visibility of the anomaly corresponding to the pre-martensitic transformation, while the change in the position and the hysteresis of the transition is minor. Therefore, we do not expect any further significant influence of the annealing on the transformation temperatures.

4.2 Magnetisation at different magnetic fields

The magnetisation loops of austenitic and martensitic phases were measured for samples Ni_2MnGa (NMG) and $Ni_2MnGa_{0.95}In_{0.05}$ (NMGIn5). The loops for the NMG sample are shown in Figure 4.3a and loops for NMGIn5 are given in Figure 4.3b. The nearly instant saturation of austenite in both materials reflects the very low magnetocrystalline anisotropy. In contrast, the martensite structure shows different loops depending on the actual arrangement of martensitic variants with high uniaxial magnetocrystalline anisotropy. The measurement of Ni_2MnGa martensite, red curve in Figure 4.3a, reflects that sample contains at least two variants as deduced from the initial fast saturation followed by nearly linear part till 1 T. The samples attached to the holder firmly by GE glue ended up as almost single variants with a-axis along the field (a-variant) after the martensitic transformation. This corresponds to nearly linear magnetisation curve from the beginnning till about 1 T field, as depicted in Figure 1a and 1b with the red curve. Usually, setting the external magnetic field to 1 T is sufficient to reorient the sample [61] and create a new variant with the easy c-axis pointing along the field (c-vatriant). However, the GE glue blocked the reorientation, and the a-variant persisted during the whole measurement of the magnetisation loop. That is seen clearly from the fact that the reverse (field decreasing) part of the loop follows nearly exactly the direct (field increasing) part.

The sample attachment and measurement procedure for the second measurement attempt on the sample NMGIn5 was changed to create c-variant lying along the field after the transformation. The sample was wrapped only by a teflon foil, to avoid blocking of reorientation by glue as mentioned above. Then it was heated to 400 K to be above the Curie temperature, which is approximately 380 K for both samples (see Section 4.1). The field was set to 7 T, which was followed by cooling down to 10 K. Such field cooling through the martensitic transformation results typically in c-variant [101]. The hysteresis loop of this field-cooled sample is shown in Figure 4.3b as the yellow line. The character of the curve with fast saturation in small field confirms that we obtained c-variant, which is evident also from the comparison with the red curve.

By considering the Clausius-Clapeyron equation 2.6, the shift of T_M in the external magnetic field can be estimated. From the measurements shown in Figure 4.3a and 4.3b we obtain $M_M - M_A = 2.70\ \frac{\mathrm{A{\cdot}m^2}}{\mathrm{kg}}$ and $M_M - M_A = 1.02\ \frac{\mathrm{A{\cdot}m^2}}{\mathrm{kg}}$ for NMG and NMGIn5 sample, respectively. Let us assume that $T_M \approx T_M^{0.01\mathrm{T}}$. According to previous results (see Section 4.1) we have $T_M^{\mathrm{NMG}} = 196$ K and $T_M^{\mathrm{NMGIn5}} = 103$ K. Next, let us consider $L = 5.5 \cdot 10^3\ \frac{\mathrm{J}}{\mathrm{kg}}$ (the latent heat for Ni_2MnGa taken from [102]). Using the Equation 2.6, one can expect the shift of T_M with the possible slope $0.10\ \frac{\mathrm{K}}{\mathrm{T}}$ and $0.02\ \frac{\mathrm{K}}{\mathrm{T}}$ for NMG and NMGIn5, respectively.

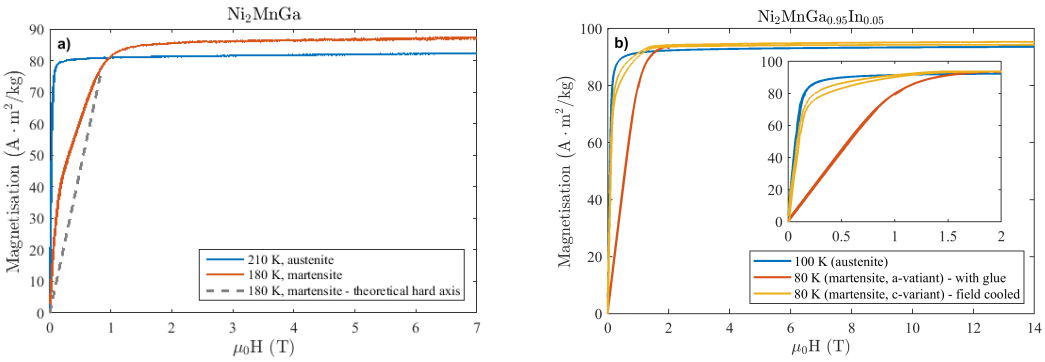

Figure 4.3: Magnetisation loops measured on **a)** Ni_2MnGa sample **b)** $Ni_2MnGa_{0.95}In_{0.05}$ sample (inset shows detail for the field from 0 to 2 T)

The temperature dependences of magnetisation were measured at different magnetic fields up to 7 T (Figure 4.4). Anomalies corresponding to the pre-martensitic transformation were observed at 246 K (NMG) and at 215 K (NMGIn5) only for the measurements at 0.01 T (not shown in Figure 4.4) and they were smeared out in higher magnetic fields, therefore its unclear from this measurement wheater T_P shifts with respect to the applied field.

A significant shift could be observed on the transition corresponding to the martensitic transformation around 200 K (NMG) and 100 K (NMGIn5). In smaller magnetic fields M_s decreases to lower temperatures. After M_s reaches its minimum, it increases nearly linearly with field. The temperature shift of M_s is several kelvins for both NMG and NMGIn5 samples. There is a difference in the position of the minimum in $M_s\,(H)$ dependence, which is approximately 0.5 T for NMG and 1.5 T for NMGIn5.

In contrast to $M_s\,(H)$ with the minimum, the $A_s\,(H)$ increases almost monotonically. Both tendencies are best recognized in curves for higher fields shown in the Figures 4.4b and 4.4d.

To cover also large fields in the dependence, the alloyed sample NMGIn5 was additionally measured using PPMS14 instrument. M_s and A_s keep increasing with the field until the largest obtained field of 14 T, see Figure 4.5.

The field dependences of M_s and A_s taken from Figures 4.4 and 4.5 are depicted in Figures 4.6a and 4.6b. It is clearly seen that the field dependence of M_s and A_s cannot be described only by the linear dependence expected from Clausius-Clapeyron equation 2.6, especially in lower fields. However, the data above 2 T can be well fitted with the linear function (their parameters are shown in the corresponding legends of Figures 4.6a and 4.6b). The resulting slopes are bigger than the shift expected form Equation 2.6. This observation implies much smaller latent heat for both samples, i.e. $1.89 \cdot 10^3\ \frac{\mathrm{J}}{\mathrm{kg}}$ for NMG and $0.29 \cdot 10^3\ \frac{\mathrm{J}}{\mathrm{kg}}$ for NMGIn5 than $5.5 \cdot 10^3\ \frac{\mathrm{J}}{\mathrm{kg}}$ taken from [102]. The step increase at 11 T seen on NMGIn5 sample could imply a intermartensitic transition at high magnetic fields. The different behaviour of Ms and As dependence in low magnetic fields can be ascribed to the different mechanism of the austenite to martensite and martensite to austenite transformation. Since only the one configuration/variant of austenite exists, the transformation to martensite should behave in the same way at various fields. On the other hand, the presence of different martensitic

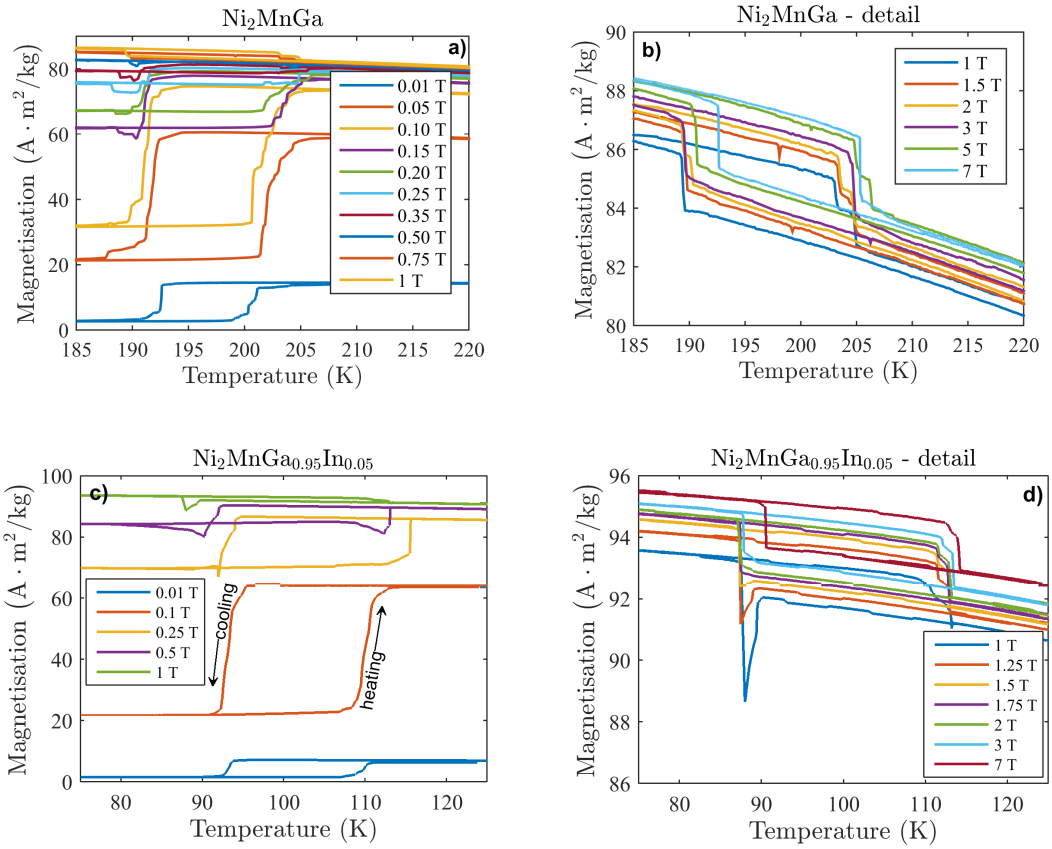

Figure 4.4: **a)** Temperature dependence of magnetisation measured at different magnetic fields up to 1 T on the sample NMG **b)** the detail for the fields from 1 to 7 T **c)** temperature dependence of magnetisation measured up to 1 T on the alloyed sample NMGIn5 **d)** the detail for the fields from 1 to 7 T

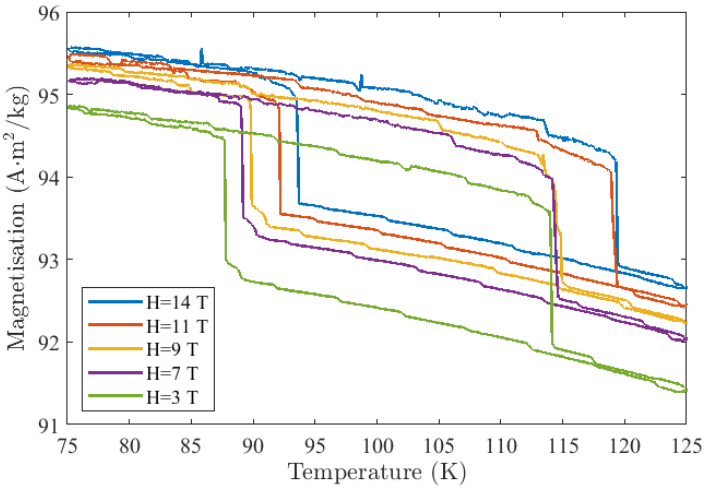

Figure 4.5: Temperature dependence of magnetisation measured on NMGIn5 sample at magnetic fields from 3 T to 14 T

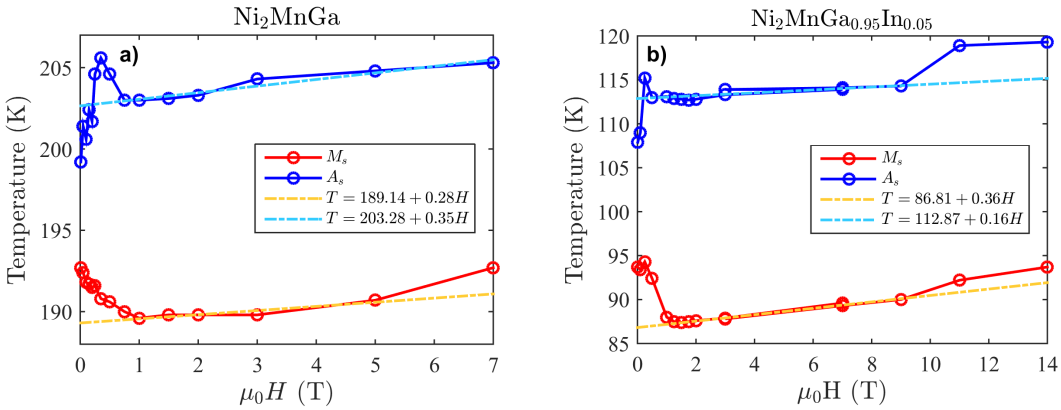

Figure 4.6: The dependence of martensitic transformation temperatures M_s and A_s on the magnetic field **a)** for the sample NMG **b)** for the sample NMGIn5

variants could influence the transformation to austenite and shift it additionally to different temperature.

To explain the shift of M_s and A_s in lower fields, the difference of magnetic energies corresponding to the austenitic and the martensitic phase should be discussed. From the comparison of the hysteresis loops shown in Figure 4.3 it can be seen that the austenite has the larger magnetisation than martensite up to approximately 1 T and 1.5 T for NMG and NMGIn5, respectively. Higher magnetisation means lower magnetic energy. Therefore the lower magnetic energy of austenite at lower magnetic fields tends to decrease the M_s. The martensite has slightly higher magnetisation than austenite at higher fields and thus it should be more energetically preferable, which is accompanied by the increase of M_s.

The situation is more obvious by computing the difference of the magnetic energy densities related to the austenitic and martensitic phases with respect to the applied magnetic field – obtained from the area between the blue and red (or orange) hysteresis loops in Figure 4.3. The computed dependencies are shown in Figure 4.7. They exhibit similar characteristics as $M_s\,(H)$ – there is a dip in the low field region and the transition to the linear dependence is approximately at the same field values.

The obtained linear behaviour of M_s in the high magnetic field region for both samples looks similar to the results reported for the off-stoichiometric thin film of $Ni_{51}Mn_{23}Ga_{26}$ [32], although the slope for NMG sample differs – according to Equation 2.6 it should be caused due to the fact they had larger magnetisation for martensite and T_M was around room temperature. The amount of indium alloying in our NMGIn5 single crystal is obviously not enough to push the slope to the negative values common for the Ni-Mn-Ga samples with In substitution [43, 44, 45]. The obtained rapid dip of $M_s\,(H)$ at the low fields corresponds to the energetic preferability connected to the difference in magnetic energy of austenitic and martensitic phase. However, it has not been previously reported, since most of the studies compared only two (high field and low field) measurements.

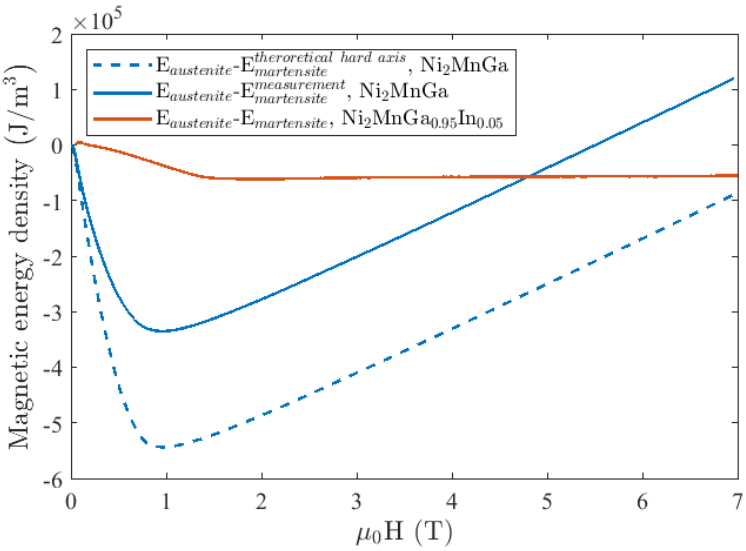

Figure 4.7: Magnetic energy density as the function of the magnetic field computed from the hysteresis loops shown in Figure 4.3. The blue curve corresponds to the magnetic energy density difference between the martensite and austenite in Ni_2MnGa sample (Figure 4.3a), the red curve to the difference in $Ni_2MnGa_{0.95}In_{0.05}$

4.3 Resistivity at different magnetic fields

Similarly to the magnetisation measurement, the electrical resistivities of NMG and NMGIn5 samples were measured at different fields - the direction of the field was perpendicular to the applied electric current. The results are shown in Figure 4.8. The anomaly corresponding to the martensitic transformation is not well visible in the resistivity data - that might be caused again by the GE glue used for the sample attachment (the similar problem is discussed in Section 4.2). The most evident is the change in the slope of the measured dependencies around T_C, which is smeared out with the increasing magnetic field. An evident change in the slope lies also around 245 K and 215 K for NMG and NMGIn5 sample, respectively, which corresponds to the pre-martensitic transformation. T_P is shifted to the higher temperatures with the increasing magnetic field. The shift is more visible in the detail shown in Figure 4.8c.

The temperatures of pre-martensitic transformation for individual measurements were obtained by the fit of the resistivity data with two polynomials of the second order in the vicinity of the transition temperature (one polynomial for the pre-martensitic region, one polynomial for the austenitic region). The values of T_P correspond to the cross-section point of these polynomials. Resulting values are shown in Figure 4.9a and 4.9b. The error bars are estimated from the mutual shift of the resistivity curves measured during cooling and heating (this shift can be seen in Figure 4.8c).

Although, the temperature shift of T_P is not so large and the values have quite big errors in comparison with the overall shift, there is an evident overall increase of the transformation temperature T_P with respect to the applied magnetic field. By the estimation of the $T_P(H)$ with linear function we obtain approximately 0.64 $\frac{\mathrm{K}}{\mathrm{T}}$ for NMG sample and 0.53 $\frac{\mathrm{K}}{\mathrm{T}}$ for NMGIn5 sample, respectively.

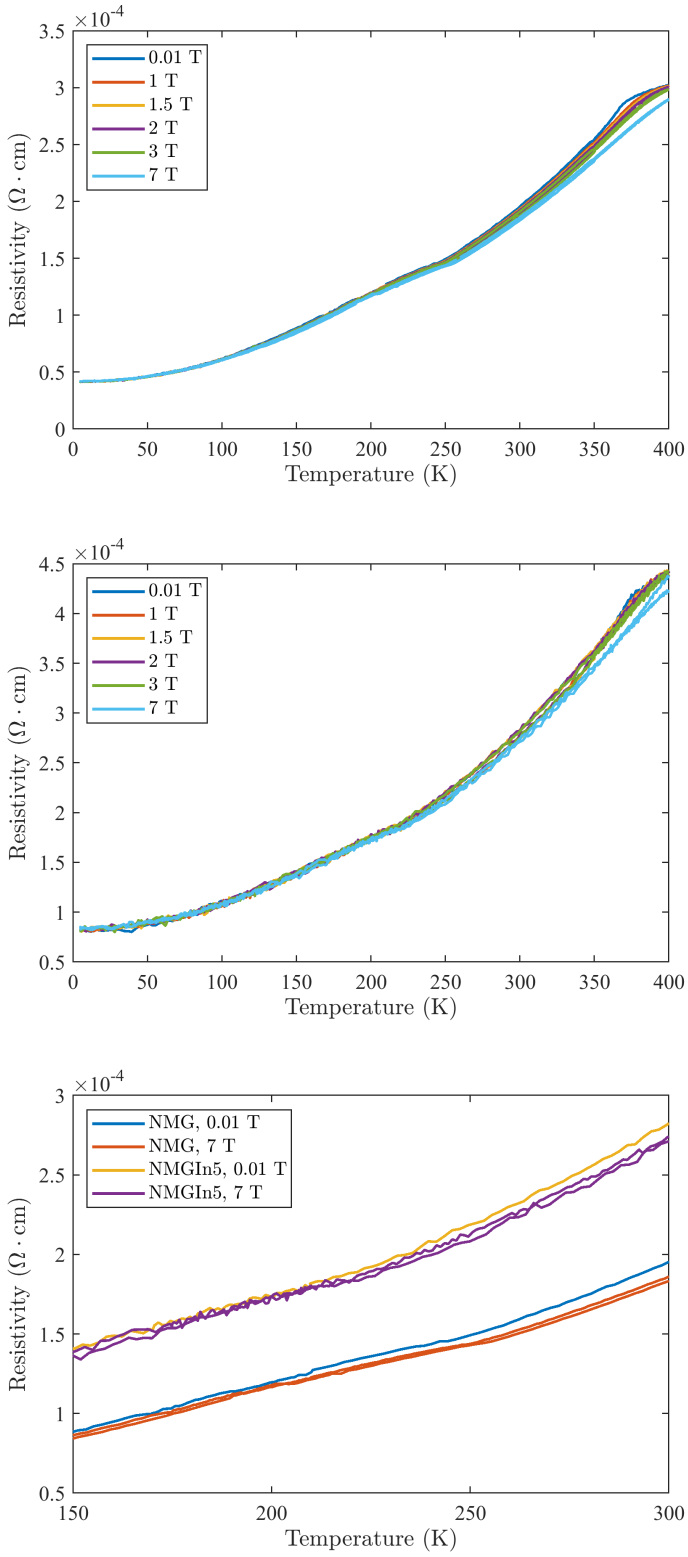

Figure 4.8: The temperature dependence of electrical resistivity measured **a)** on the sample NMG **b)** on the sample NMGIn5. **c)** the detail of the temperature region around pre-martensitic transformation

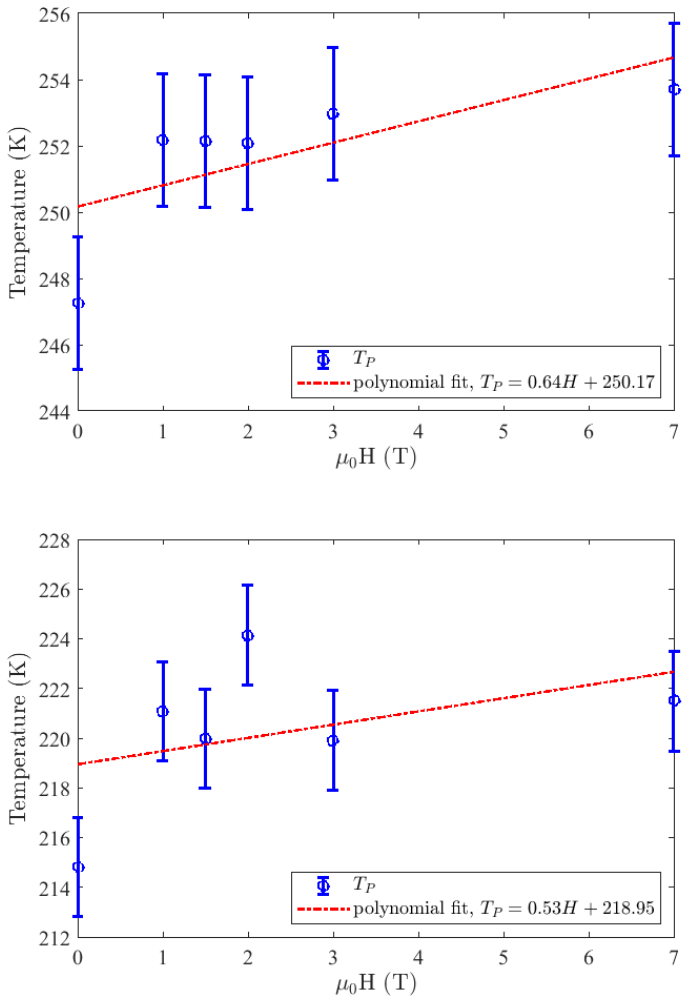

Figure 4.9: The field dependence of the pre-martensitic transformation temperature T_P obtained from the electrical resistivity data **a)** NMG sample **b)** NMGIn5 sample

5. Study of structure by X-ray diffraction

5.1 Lattice parameters and modulation

Low temperature X-ray diffraction measurements were performed on samples Ni_2MnGa, $Ni_2MnGa_{0.98}In_{0.02}$ and $Ni_2MnGa_{0.95}In_{0.05}$, in which the martensitic transformation was clearly observed in the magnetisation data. The reciprocal space maps of the Bragg reflections 200, 400, 600, 620 and the satellite peak $400+\vec{q}$ ($\vec{q}$ is the modulation vector) were measured at various temperatures down to 5 K to map the temperature dependence of the lattice parameters and the modulation. An example of measured reciprocal space maps is shown in Figure 5.1 for the Bragg reflection 620 measured on $Ni_2MnGa_{0.95}In_{0.05}$ during cooling. Due to the presence of the twinning [6, 19] over the planes of the crystallographic form {110} the Bragg reflection 620 corresponding to the austenitic phase is split to the three Bragg reflections 620, $62\bar{0}$ and 260 during the martensitic transformation. This fact complicates the peak indexation, but, on the other hand, it provides more information for the refinement of lattice parameters.

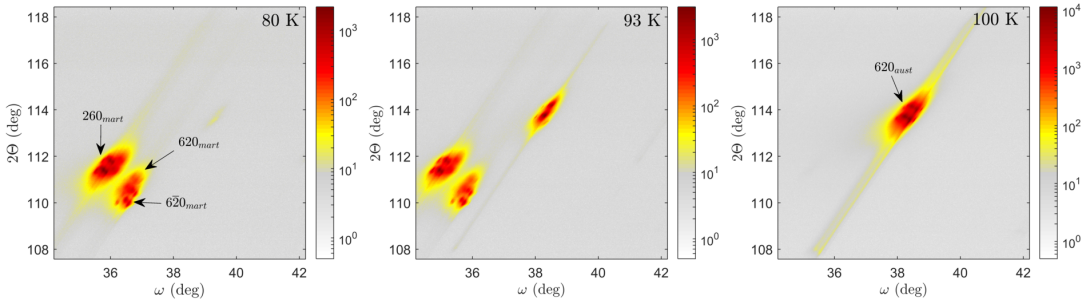

Figure 5.1: Reciprocal space maps of the Bragg reflection 620 measured on the sample $Ni_2MnGa_{0.95}In_{0.05}$ at three different temperatures, 80 K, 93 K and 100 K around the martensitic transformation (during cooling). The splitting to several diffraction spots during the martensitic transformation is clearly visible.

Lattice parameters were obtained by the same procedure as used also in [19, 51]. The refined parameters and the unit cell volume during the heating obtained from 2Θ positions of individual Bragg reflections are shown in Figures 5.2 and 5.3. The cooling case looks very similar, the only difference is the temperature hysteresis, which can be seen also in the magnetisation and the electrical resistivity data (see Figures 4.2 and 4.1). For better visibility the temperature dependences of the monoclinic γ angle were fitted with the function $\gamma = A + B \cdot \exp(C \cdot T)$, where A, B, C are refined parameters and T stands for the temperature.

The high temperature austenitic and pre-martensitic phases are cubic, the low temperature martensite is monoclinic. Lattice parameter a of the cubic austenite and pre-martensite increases with increasing indium amount. Concerning low temperature monoclinic martensite, parameter c increases with increasing indium content as well. Contrary, the lattice parameter a of monoclinic martensite

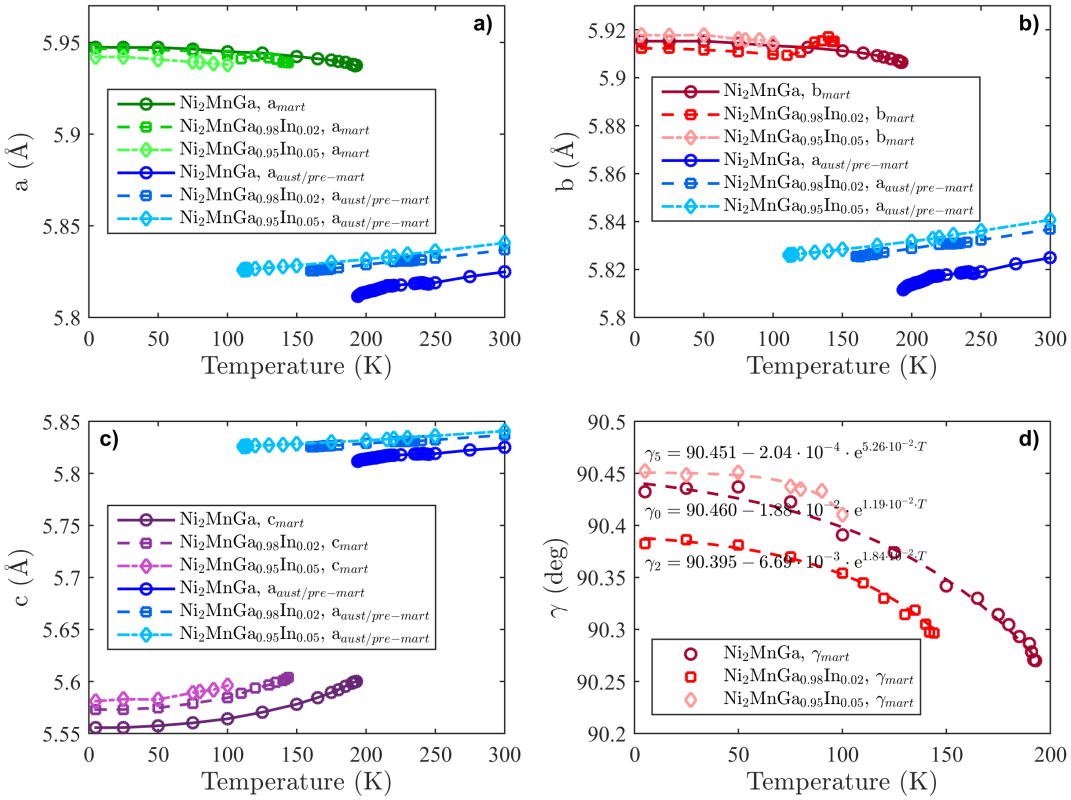

Figure 5.2: Lattice parameters during the heating, the error bars are comparable to the size of markers. **a)** lattice parameter a, **b)** lattice parameter b, **c)** lattice parameter c, **d)** γ angle of the monoclinic martensitic phase and its fit with function $\gamma = \mathrm{A} + \mathrm{B} \cdot \exp(\mathrm{C} \cdot T)$

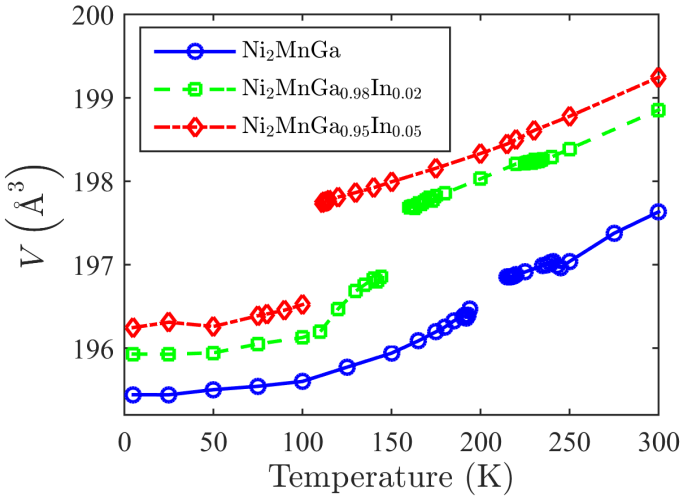

Figure 5.3: Unit cell volume during the heating, the error bars are comparable to the size of markers

is smaller with increasing indium content. Parameter b has a similar temperature dependence as parameter a, but it has no significant dependence on indium content. No significant dependence on indium for γ angle has been observed as well. Increasing indium amount increases the unit cell volume, as it is clearly visible in Figure 5.1. Moreover, indium alloying increase the volume change during the martensitic transformation.

The temperature dependence of the coordinate q of the modulation vector $\vec{q}_{mod} = (q, q, 0)$ obtained from the position of satellite peaks $400 + \vec{q}$ is shown in Figure 5.4. According to the Section 1.1.3, the modulation vector $\vec{q} = (2/5, 2/5, 0)$ or $\vec{q} = (3/7, 3/7, 0)$ for low temperature martensite and $\vec{q} = (1/3, 1/3, 0)$ for pre-martensitic phase could be expected. The values in Figure 5.4 show that our results differ from this expectation. The length of the modulation vector seems to be dependent on temperature. Moreover, the length of the modulation vector is influenced by the indium amount as well. Higher indium content increases the length of modulation vector in the pre-martensitic phase and decreases its length in martensitic phase.

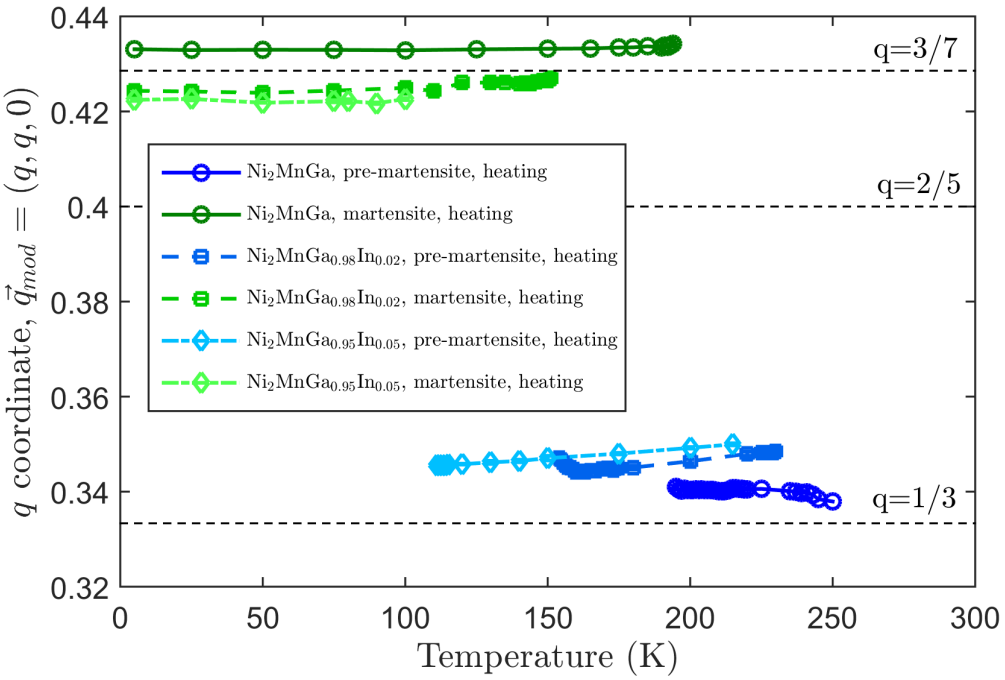

Figure 5.4: The coordinate q of the modulation vector $\vec{q}_{mod} = (q, q, 0)$ as a function of temperature

By considering a model for modulation we can estimate the modulation amplitude. Let us choose the simple sinusoidal modulation of atomic coordinates as in Equation 2.25 which leads to the structure factor described by Equations 2.11 and 2.26. Using mentioned formulae we computed the temperature dependence of the modulation amplitude $|\vec{U}|$ from the ratio of integrated intensities of Bragg reflection 400 and satellite $400 + \vec{q}$. The direction of $\vec{U}$ was chosen along $[\bar{1}10]$ (see i.e. [19, 9, 103]). The results of the evaluation are depicted in Figure 5.5. It can be seen that the modulation amplitude is approximately two times bigger in martensitic phase than in pre-martensite. The modulation amplitude in pre-martensite is decreasing with increasing indium content (see Figure 5.5).

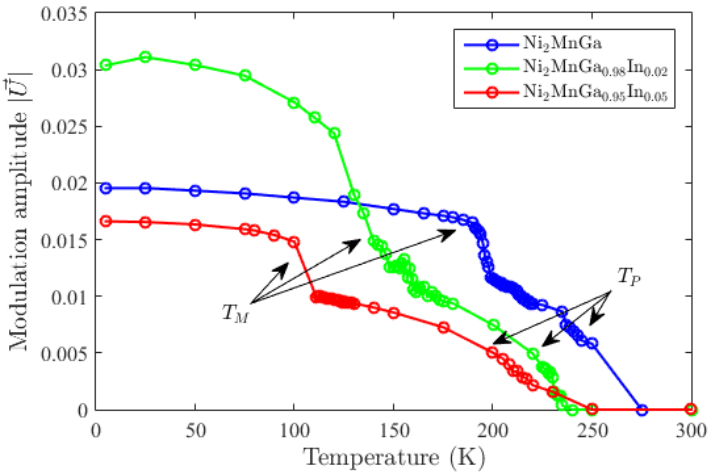

Figure 5.5: Temperature dependence of the length of the modulation amplitude vector $\vec{U} = [-u, u, 0]$ during the heating

The calculated modulation amplitude in Figure 5.5 can be influenced by the fact where In atoms sit in the unit cell. We assumed that indium replaces only gallium, since the structure of Ni_2MnIn is the same as Ni_2MnGa [104] and In and Ga has the same number of the valence electrons. But in general, In could mix with the Ni and Mn as well. Depending on the option where indium sits on different atomic sites, the structure factor and thus the integrated intensity of Bragg reflection 400 and of the satellite peak can change slightly about several percents. However, similar shift of the intensity can be achieved by the change of the ratio between $L2_1$ and $B2'$ ordering in the sample. To find the exact position of In atoms in the unit cell, additional experiments, such as NMR, EXAFS or a measurement of an anomalous diffraction, need to be performed.

5.2 Phase diagram

Temperature versus composition phase diagram constructed from the critical temperatures given in Table 4.1 is shown in Figure 5.6. The composition dependences of the critical temperatures can be fitted with linear function. Slopes of these dependences are then -1.1 K/% (percents of In) for Curie temperature, -5.9 K/% for the temperature of pre-martensitic transformation and the fastest decrease has the martensitic transformation temperature -22 K/%. The critical amount of In when the martensitic transformation is suppressed is for $x \approx 10$ %.

The dashed lines in Figure 5.6 correspond to the results previously published by Khan et al. [34]. A significant difference is clearly visible – Khan et al. observed martensitic transformation in the samples with indium content up to $x \approx 0.14$ (but according to the trend in their data, it should be observable even up to $x \approx 0.20$). This clearly indicates that critical temperatures are dependent on the crystallinity of the sample (polycrystalline versus single crystal) and/or on the sample preparation procedure.

One of previous studies on Ni-Mn-Ga [105] has shown that relatively high residual compressive stress can remain in the polycrystalline buttons after preparation by the arc melting. Other previously published works [64, 106] have also

shown that T_M and T_P can be easily manipulated with relatively small uniaxial or hydrostatic pressure. Since Khan et al. prepared their samples by the arc melting, the remaining residual stress could shift the transition temperatures. Moreover, their polycrystalline samples were annealed for 72 hours at 900°C only, which can be insufficient time to homogenize the indium composition as it is discussed in Chapter 3 (see Figure 3.3).

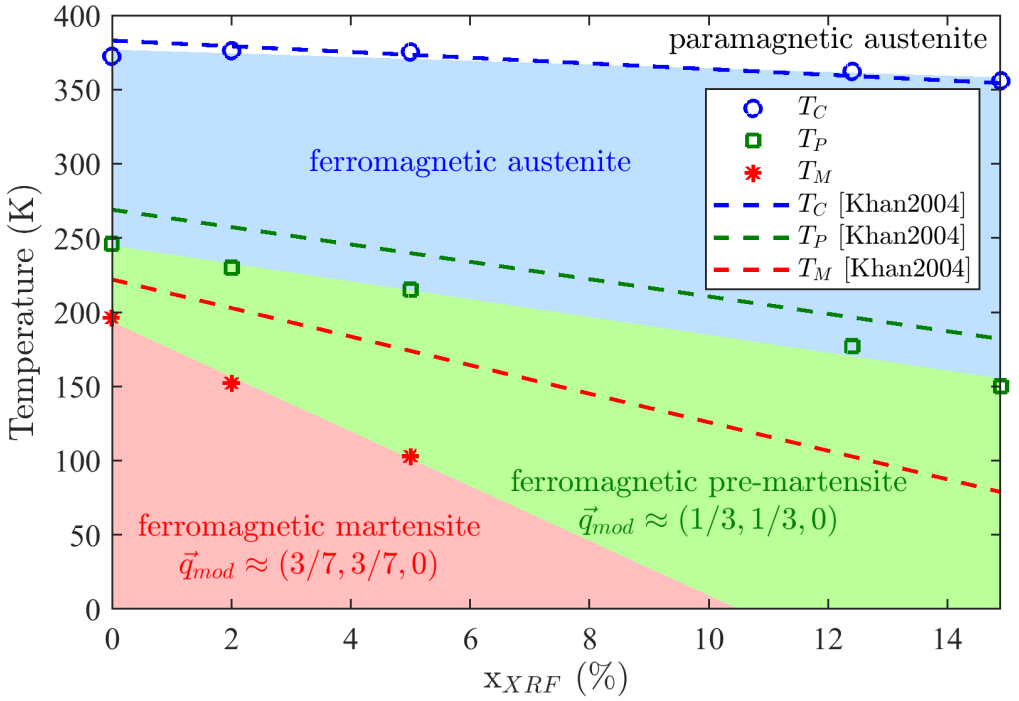

Figure 5.6: $T - x$ phase diagram of $Ni_2MnGa_{1-x}In_x$ based on data from the measured temperature dependences on our prepared single crystals. The dashed lines correspond to data from Khan et al. [34] obtained for polycrystalline samples.

6. X-ray diffraction measured on off-stoichiometric Ni_2MnGa in-situ in tension

In this chapter, the results following from the diffraction experiment performed in-situ in tension will be presented. The motivation for this study was the possible reorientation of the sample induced by an external mechanical force (see the Section 1.2). The attention was paid especially to the evolution of the lattice parameters, the modulation and population of twin variants with respect to the applied tension. Since the reorientation effect is connected to the martensitic phase and we cannot cool the sample during the tensile experiment, we performed the measurements on the samples N50M28G28 and N50M28G28$_{RC}$ which are in the martensitic state at room temperature. Our $Ni_2MnGa_{1-x}In_x$ single crystals have the martensitic transformation bellow the room temperature.

This chapter is divided in several sections according to the sample attachment in the tensile stage mentioned in the Section 2.2.6 and according to the initial states of the sample created by defined pressing.

6.1 The block sample held directly by the clamps and dog-bone shaped sample setup

The attempt with holding the sample with the clamps served as as the preliminary measurement - to see a possible sample behaviour during the tensile experiment. Before the own measurement, the sample was compressed (by hand) along its longest dimension - the purpose was to create a single-variant state. The sample arrangement in this setup is sketched in Figure 2.6a.

With this setup, we came across several issues in the following measurement. First of all, holding by the clamps itself could induce a reorientation inside the sample, at least at the place, where the sample is held. Moreover, the teeth on the clamps cause plastic deformation to the sample ends. The biggest issue was the sample rupture. By applying the tension, the twin variant in the middle part of the sample was created (it can be seen by eye - Figure 6.1). During the increase of the applied tension the twin boundaries were shifted towards the clamps as the twin variant increased its volume. At the point (cca 12 MPa), where the twin boundary reached the end of the sample held by the clamps, the sample cracked. The situation is sketched in Figure 6.2.

The tension required for the movement of twin boundaries should be several MPa [67, 61] (depending also on the twin boundary type - see Section 1.2.1). Unfortunately, the bottom limit for the tension, which can be successfully held by the tensile stage for a long time period is approximately 1 MPa, therefore we are limited in the resolution of the applied tension. However, we were able to observe almost full sample reorientation at 10 MPa.

The reciprocal space maps in Figure 6.3 show the evolution of the diffraction peak 400 for the three steps in tension measured in symmetrical geometry.

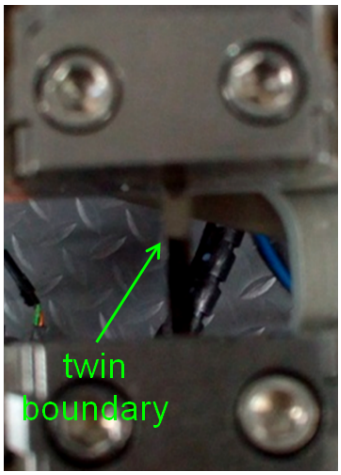

Figure 6.1: Twin boundary on the N50M28G28 sample

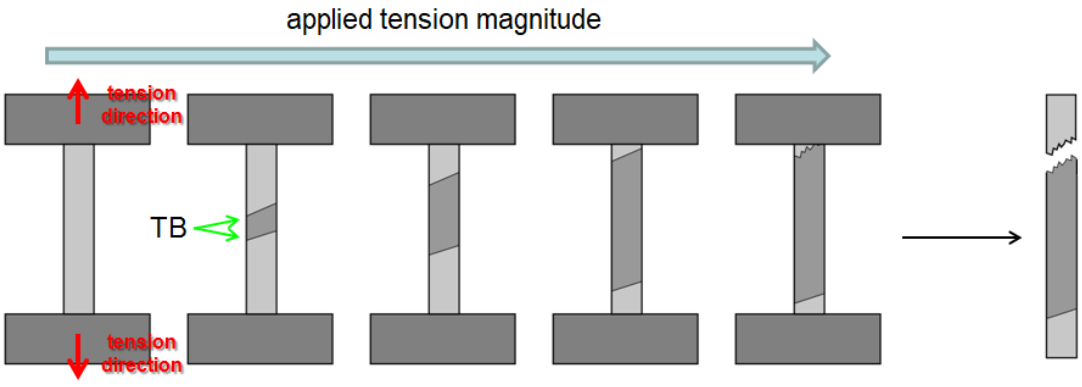

Figure 6.2: Evolution of the twin boundary (TB) during the increase of the applied tension (top view on the sample).

The map in Figure 6.3a corresponds to the initial state, where the sample contained mostly domains with the crystallographic axis a and b pointing along the sample normal in the out of plane direction. Therefore, the peaks corresponding to Bragg reflections 400 and 040 are visible in the map at the same time. During the application of the tension, the intensity of both peaks is changing. Moreover, a new peak corresponding to Bragg reflection 004 appears (see Figure 6.3b) - that corresponds to the creation of the new domain with the out of plane c axis. During the further increase of tension, the intensity of 004 peak increases, whilst the peaks 400 and 040 basically disappear (see Figure 6.3c). The 2Θ-profiles obtained by the integration of the maps over ω angle are shown in Figure 6.4a. Using the Equation 2.10 we can compute relative volume ratios of the individual twin variants, which are shown in Figure 6.4b.

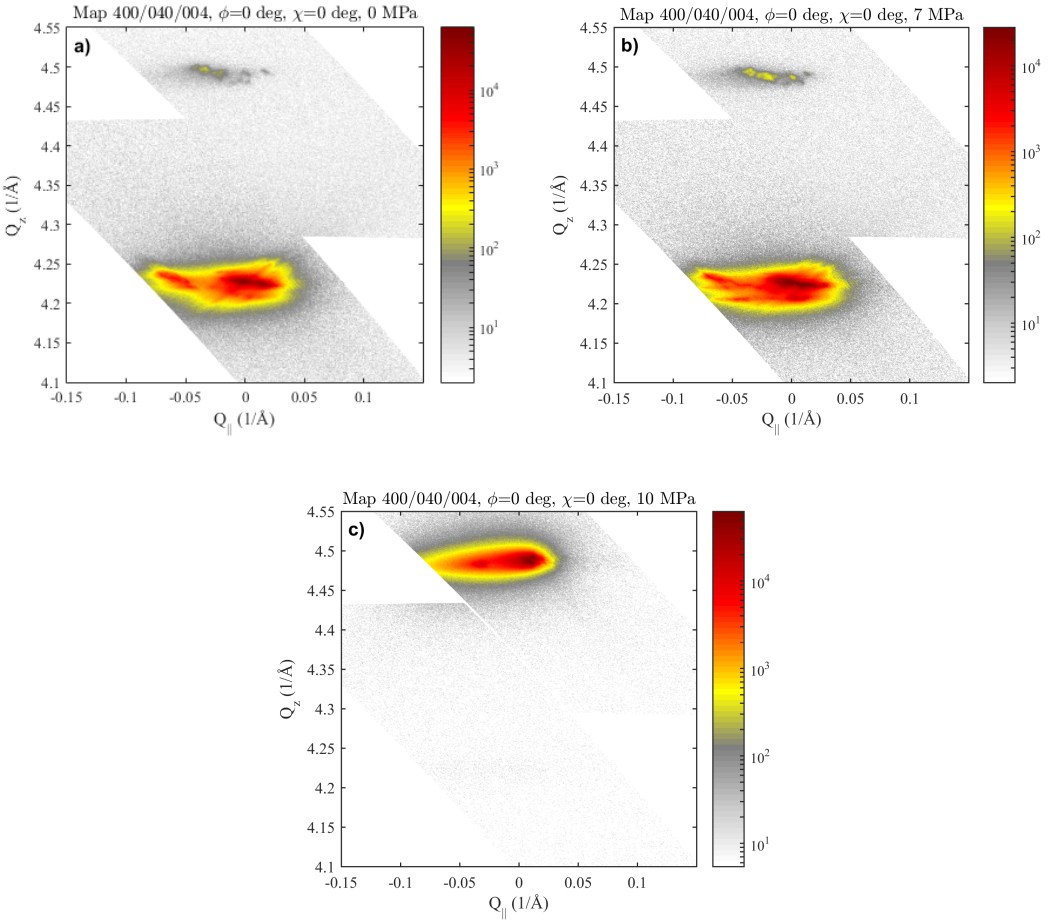

Figure 6.3: The maps of the diffraction peak 400 measured at different tensions **a)** 0 MPa **b)** 7 MPa **c)** 10 MPa

Another attempt was performed on the dog-bone shaped sample prepared from the long single crystal N50M28G2$_{RC}$ by the electrospark cutting. The sample arrangement is shown in Figure 2.6c. However, this attempt was even more unsuccessful (not shown) than holding the sample directly by the clamps. The cutting left probably little cracks on the sample which led to its rupture even already at 3 MPa.

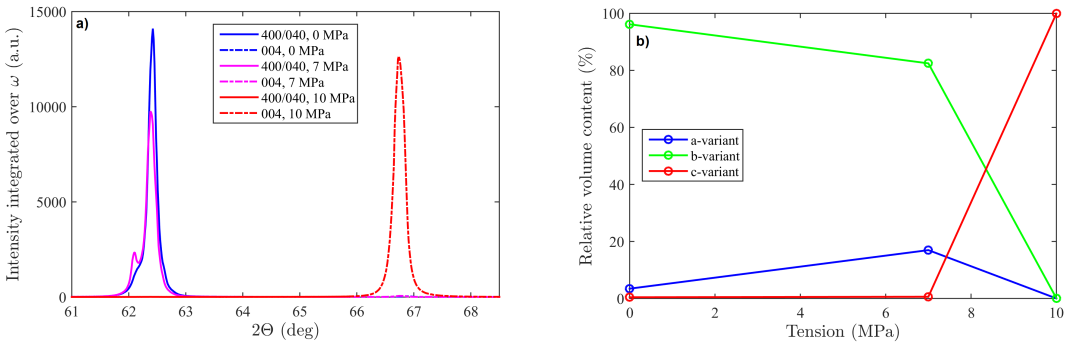

Figure 6.4: **a)** 2Θ-profiles obtained by the integration of the maps in Figure 6.3 over ω angle **b)** the relative volume ratios of individual twin variants computed from the integrated intensities of Bragg reflections 400, 040 and 004

6.2 The block sample with its ends glued to the steel plates

During the third sample arrangement option the specimen was glued onto the steel plates. The arrangement is sketched in Figure 2.6b. Two different initial states of the sample were created before the measurement. The first measurement was performed on the sample compressed beforehand along its longest dimension - this should create a sample variant with the c-axis along the applied tension (let us label it C initial). The second attempt was performed on the sample compressed beforehand along its short dimension - that should create a/b laminate (see Section 1.2.1) along the sample longest dimension (let us label it A/B initial). The first unsuccessful measurements were performed with the montage glue and the superglue - unfortunately, they didn't last more than 8 MPa of tension. The successful attempt was done with the two-components epoxy glue - it lasted 20 MPa and the sample still held on the plates.

Before the X-ray diffraction measurement we decided to perform the tensile experiment in-situ with the optical microscopy. That should help us to directly see what is happening on the sample surface and to determine the values of tension necessary for the twin boundaries motion and the creation of new twins. The time dependence of the tension set during the experiment is shown in Figure 6.5. At first, the sample was gradually tensed upto 19.2 MPa with several intermediate steps (the tensions 3.6 MPa, 6 MPa, 7.6 MPa, 9.2 MPa, 15.2 MPa, 19.2 MPa) where the tension was held for 15 s. Then, the tension was released again with the same steps and the sample was compressed to -15.2 MPa with the intermediate steps of -3.6 MPa, -6 MPa, -7.6 MPa, -9.2 MPa and -15.2 MPa.

The micrographs resulting from the optical microscopy for the sample C initial are shown in Figure 6.6. One can see that a large amount of new twins is created already around 0.8 MPa. This is manifested also in Figure 6.5 around 100 s - the tension started to increase already, but the sample is relaxed during the twinning and therefore a small plateau in the graph is created. The specimen also relaxes at the intermediate tension steps where the tensile stage tries to keep the tension constant. Further increase of the load leads to a creation of one large domain, which boundary propagates through the sample (see Figure 6.6c and 6.6d). One

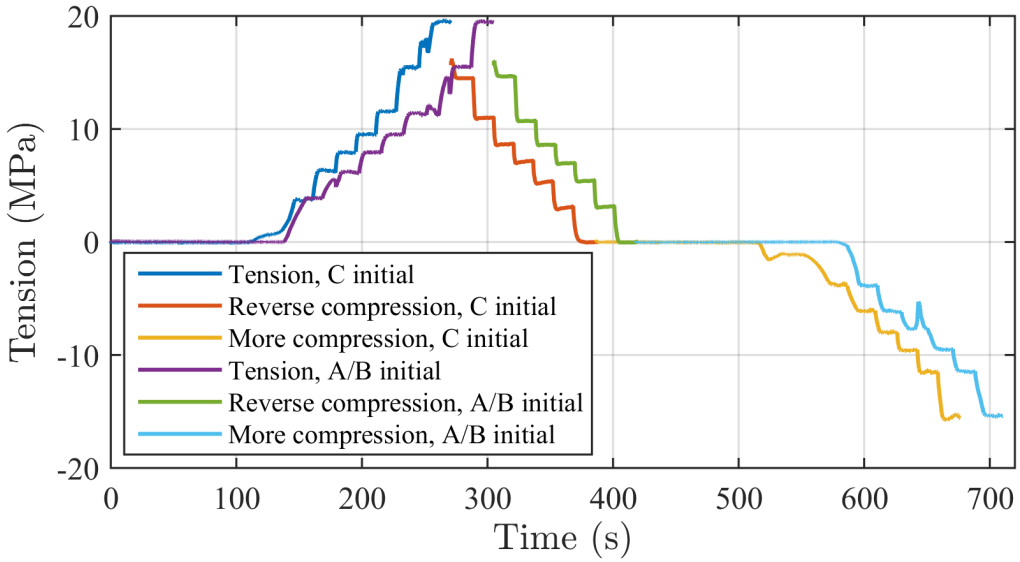

Figure 6.5: The time dependence of the load and tension set during the optical microscopy experiment on samples C initial and A/B initial

can also see that the boundary propagates not only during the increase of the tension but also at the time when the stage tries to keep the tension constant - Figure 6.6c corresponds to the start and Figure 6.6d to the end of the intermediate plateau at 3.6 MPa. Above 6 MPa this boundary propagates very slowly, since it probably met another twin boundary and they mutually block each other. The twin boundaries of the type I and II are also distinguishable, since the angle between the boundaries is approximately 6 deg. During the compression, the domain boundary propagates backwards (see Figure 6.7) and the state similar to the initial one is created.

The micrographs resulting from the optical microscopy for the sample A/B initial are shown in Figure 6.8. In comparison to the sample C initial, one can clearly see the difference - the most of the twin boundaries induced during the tension application lies along the longest direction of the sample. Since a/b laminate twin boundaries should be best visible with the polarised light or electron microscopy [107] these boundaries correspond to the a/c (or b/c) twinning. One can also distinguish the twin boundaries of type I and II as in previous case. The presence of multiple domains is also evident - there are boundaries vertically oriented (with respect to the figure) and another boundaries with mutual orientation about 45 deg - they correspond to the domains rotated rotated 90 deg around the sample longest dimension (therefore the corresponding "vertical line" lies at the sample side).

During the compression, the new b/c twins induced during the tension application are pressed out and the state similar to C initial is created.

The measurement at the same tension values was performed in-situ with the measurement of X-ray diffraction. In contrast to the optical microscopy measurement, the tension at the intermediate steps was held approximately for 40 min, to cover the reciprocal space mapping of the sufficient amount of Bragg reflections. We performed the measurement on Bragg reflections 400, 620, $6\bar{2}0$, 440 and 153 (153 is the only accessible Bragg reflection with rotation in ϕ allowed by

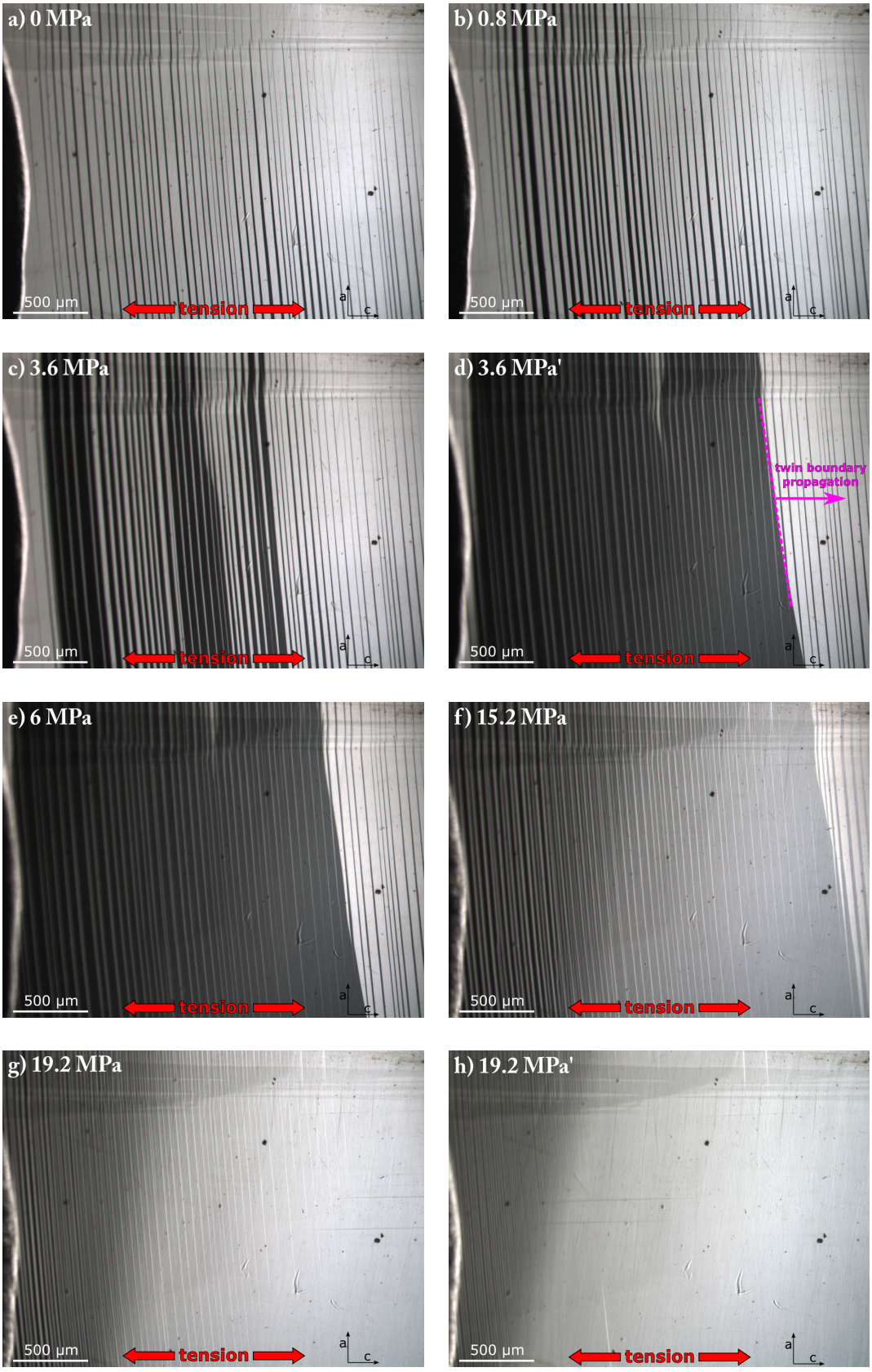

Figure 6.6: The micrographs of the C initial sample surface obtained from the optical microscopy during tension. The tension direction is indicated by the red arrows. The black arrows indicate the presumed crystallographic axes of the initial state.

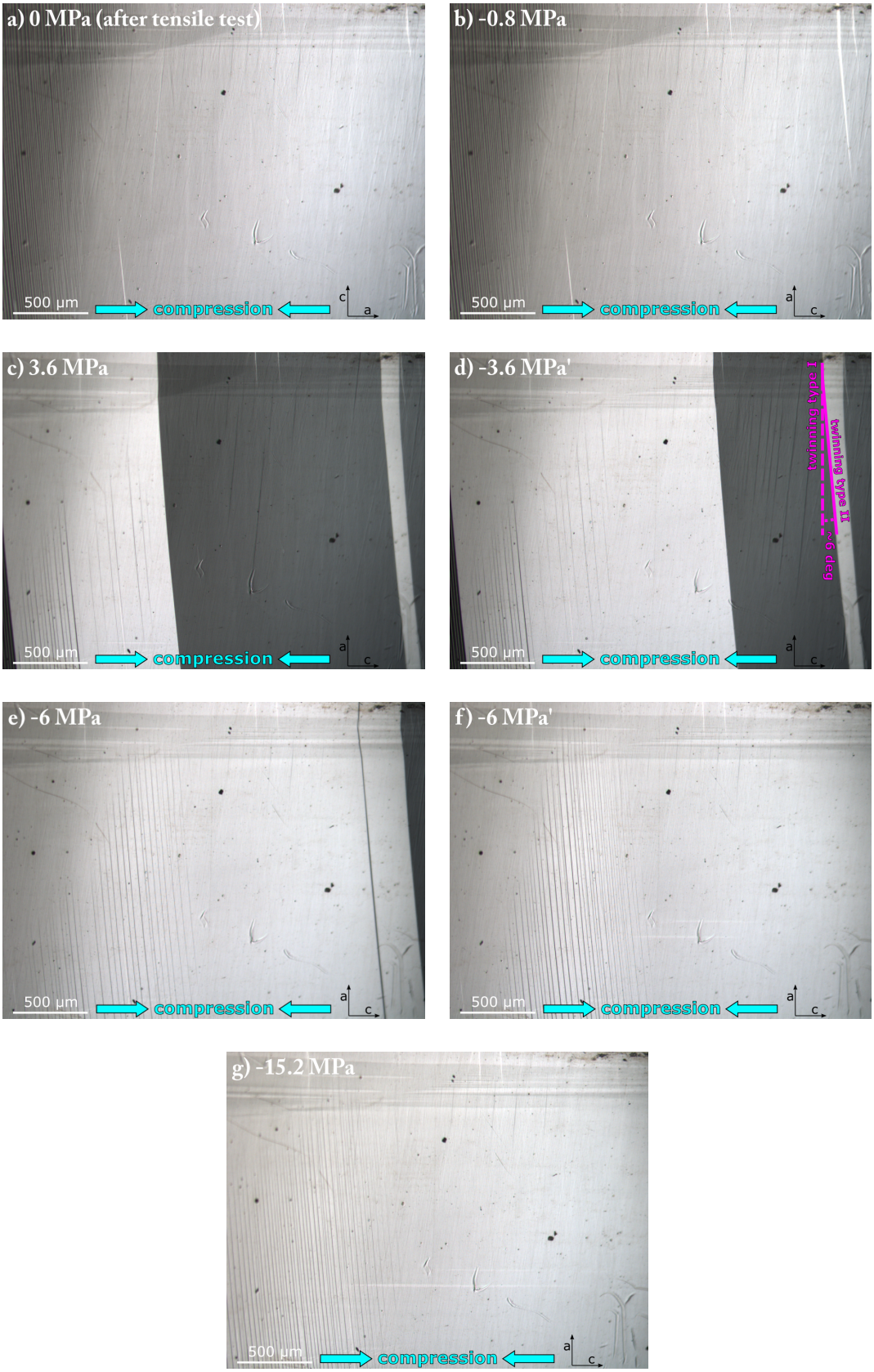

Figure 6.7: The micrographs of the C initial sample surface obtained from the optical microscopy during compression. The compression direction is indicated by the blue arrows. The black arrows indicate the presumed crystallographic axes of the initial state.

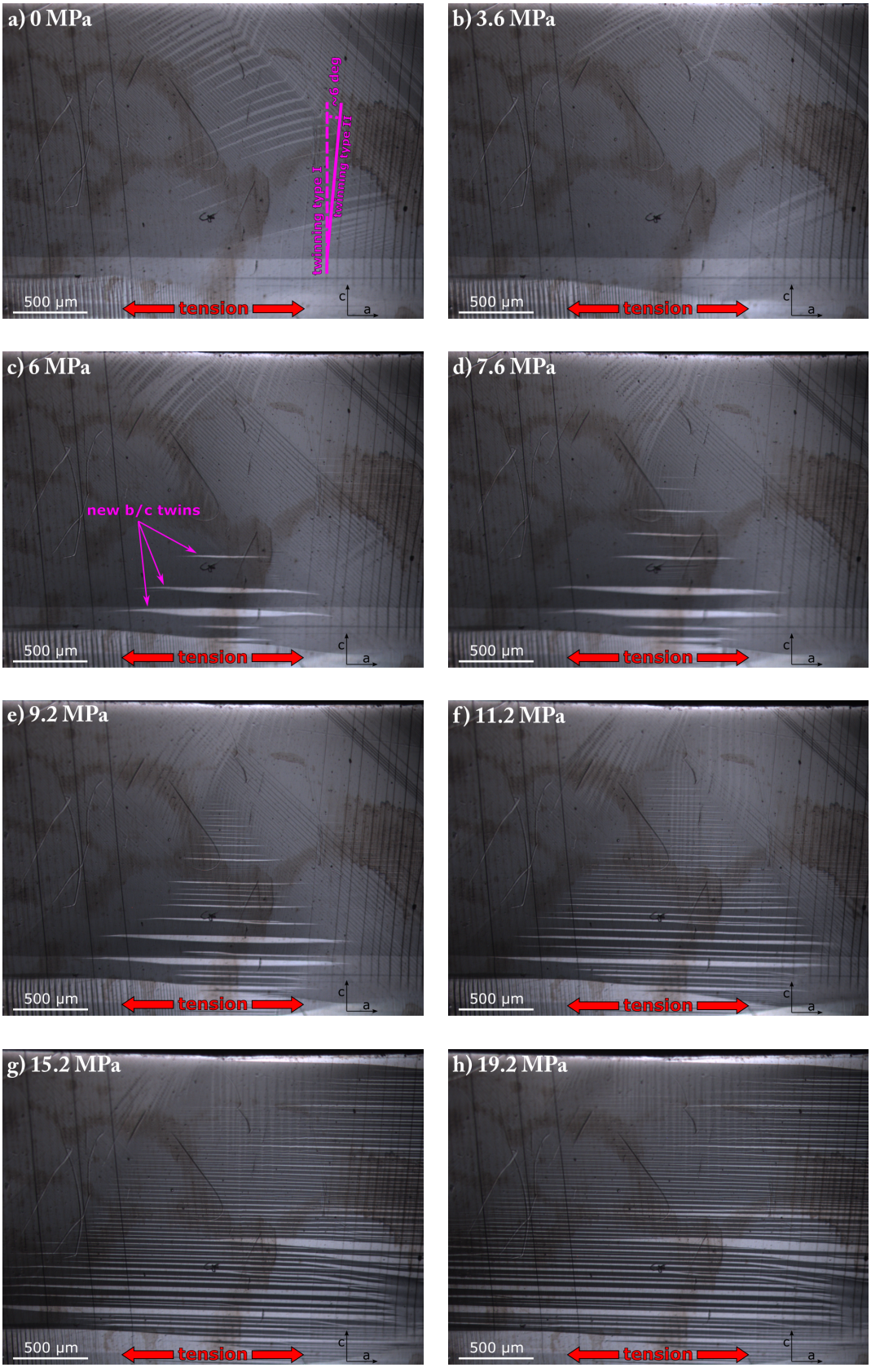

Figure 6.8: The micrographs of the A/B initial sample surface obtained from the optical microscopy during tension. The tension direction is indicated by the red arrows. The black arrows indicate the presumed crystallographic axes of the initial state.

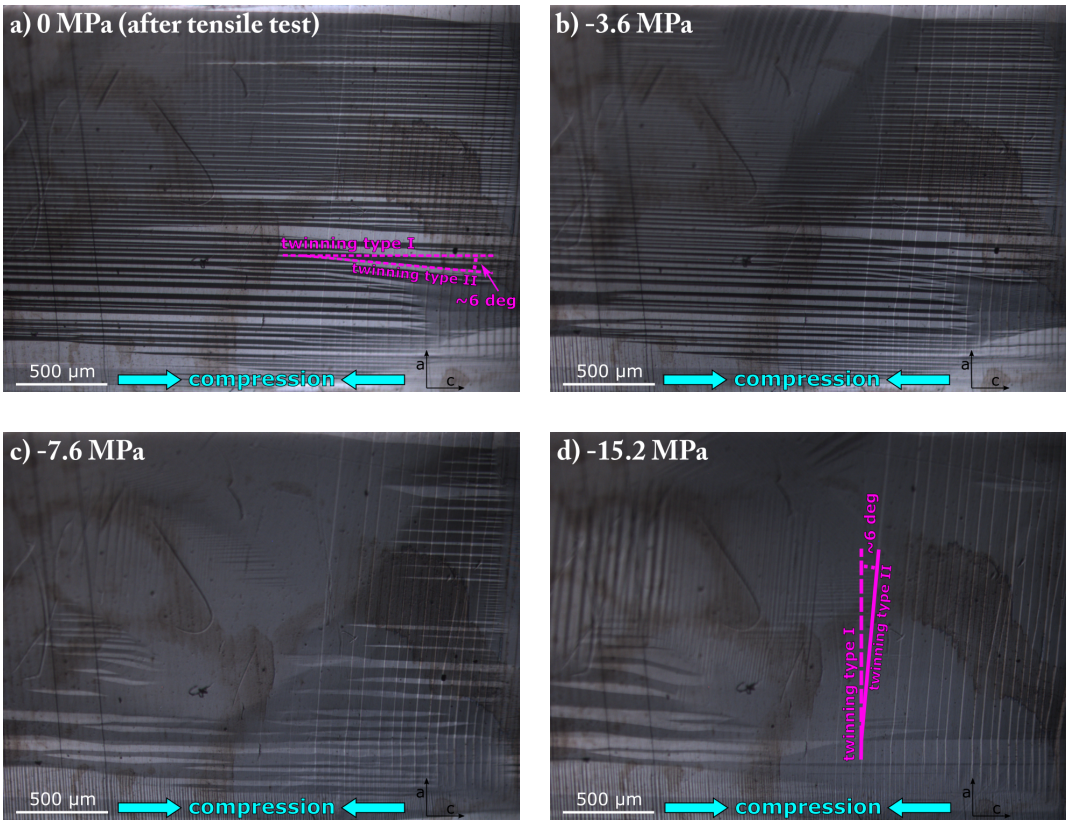

Figure 6.9: The micrographs of the A/B initial sample surface obtained from the optical microscopy during tension. The compression direction is indicated by the blue arrows. The black arrows indicate the presumed crystallographic axes of the initial state.

the movements limits of the stage) and several satellite diffraction between 400 and 620 main maxima, to determine the lattice and modulation parameters.

However, during the fit of the lattice parameters one should be careful with the data processing, since we cannot fit 2Θ positions of the all Bragg reflections from one map at different tensions together as it was done in the case of the low temperature diffraction in Chapter 5. During the tension, the deformation of the differently oriented domains is not the same, therefore the lattice parameters corresponding to individual domain peaks in one reciprocal map should be treated separately.

The data were treated as follows: let's assume that the lattice parameters are the same for each domain at the initial state (even for C initial and A/B initial state together). Therefore, we can use the same procedure for this special case as in Chapter 5. With the known lattice parameters we can compute the orientation (Euler angles) of one domain with respect to the diffractometer axes. The individual orientation of twins can be geometrically well described (see Section 1.2.1). Therefore, we are able to describe all the diffraction spots in each map by an addition of the twins to the original domain and the computation of the positions of corresponding Bragg reflections. After that, we can treat the diffraction spots during the measurement in applied tension separately, since we would know which domain each diffraction spot belongs to.

The reciprocal space maps measured at the C initial state of the sample at 0 MPa are shown in Figure 6.10. To describe all diffraction spots in the reciprocal space maps in Figure 6.10, ten domains were successfully found. The crosses in the maps in Figure 6.10 correspond to the positions of the diffraction spots connected to individual domains, which mutual orientations resulting from the simulations are shown in Table 6.1. It needs to be mentioned that the diffraction spots corresponding to the individual domains may not be seen in each of the maps due to several reasons. The incident angle for each map is different, therefore the irradiated area on the sample differs - due to that the largest number of diffraction spots can be seen in the map 620 (Figure 6.10b), because the corresponding incident angle is the lowest. Next, the incident angle influences the penetration depth and therefore the diffraction spots connected to the domains which do not lie on the sample surface can be seen only at higher incident angles. This is probably the case for the domain D4 - the corresponding diffraction spot is not seen in the map 620 (Figure 6.10b), but its visible in the map $6\bar{2}0$ (Figure 6.10c), which corresponding angle of incidence is high.

The last reason of the absence of the diffraction spot in the map is a low intensity, which is the case of the most of the domains in the map 351 (Figure 6.10d), because the Bragg reflection 351 has a low intensity due to the reasons described in Section 2.2.6. The orientation of the domains with the largest irradiated volume (corresponding to the spots with the highest intensity in the map 260 (Figure 6.10b)) is depicted in Figure 6.12.

The similar procedure was performed for the A/B initial state of the sample. The reciprocal space maps measured at 0 MPa with corresponding domain spots are shown in Figure 6.13. The resulting mutual orientations of the domains for A/B initial state are listed in Table 6.2. The orientation of the domains with the largest irradiated volume corresponding to the spots with the highest intensity in the map 062 (Figure 6.13b)) is depicted in Figure 6.15.

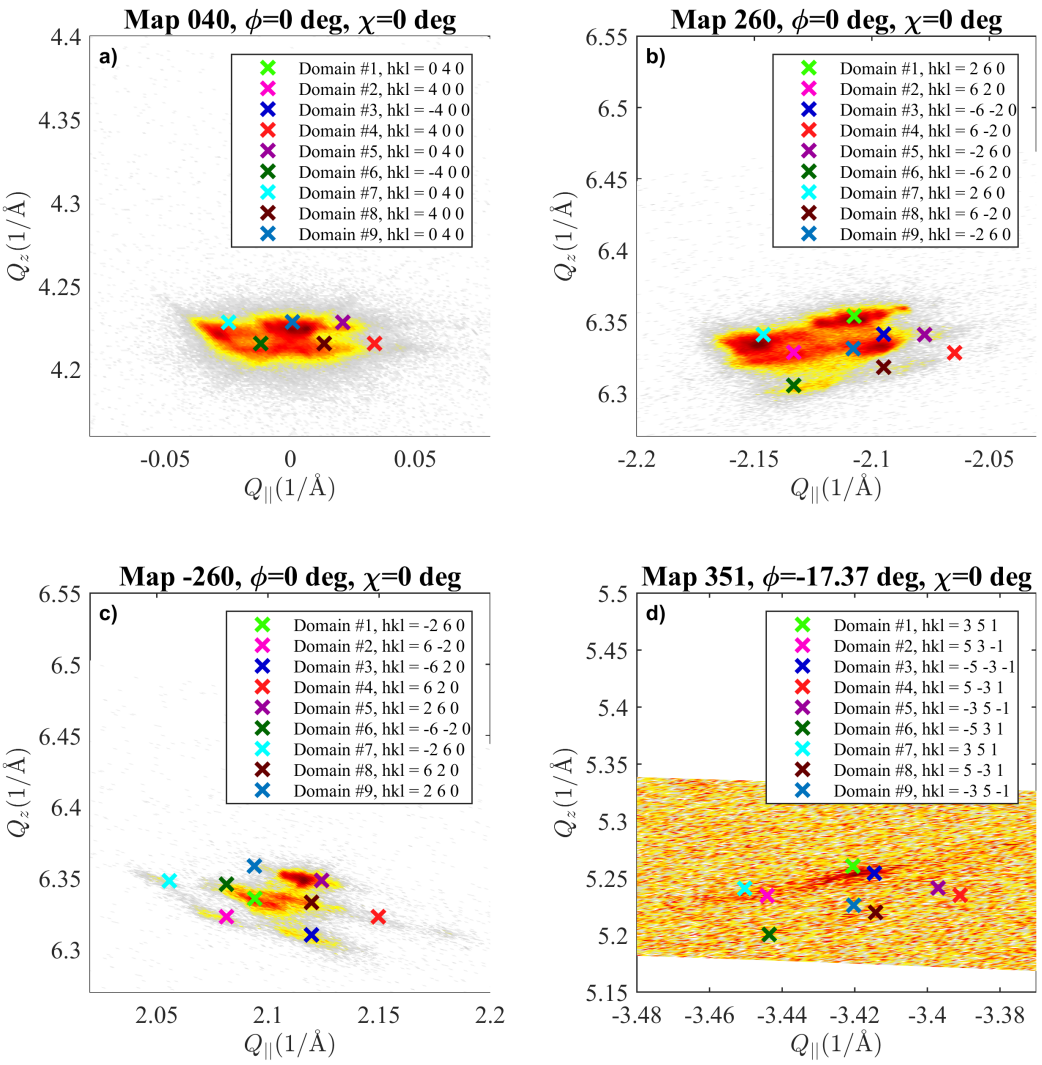

Figure 6.10: The reciprocal space maps measured at the C initial state of the sample at 0 MPa

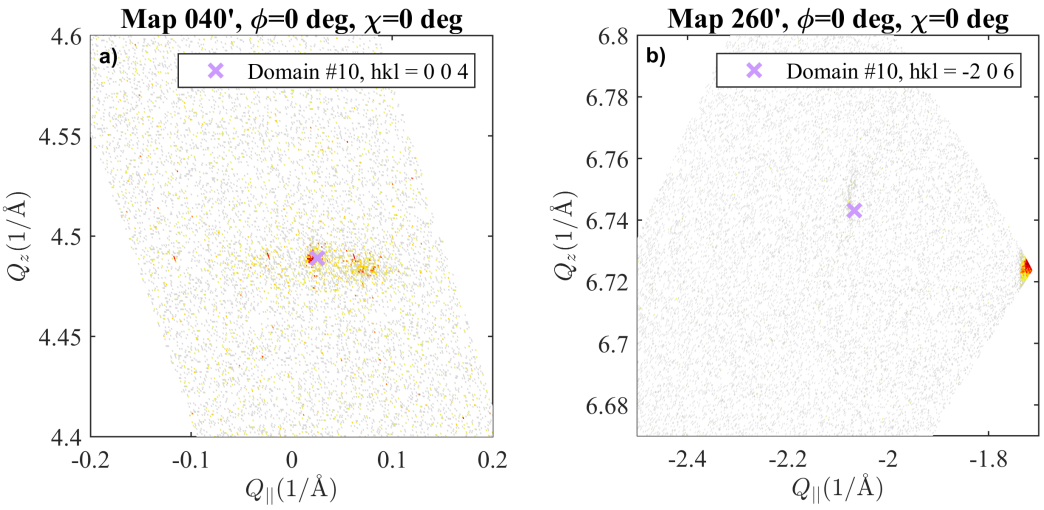

Figure 6.11: The reciprocal space maps corresponding to the domain with the c axis out of plane of the sample measured at the C initial state of the sample at 0 MPa

domain label	domain relation	Euler angle A (deg)	Euler angle B (deg)	Euler angle Γ (deg)
D1	reference domain	-182.1653	-92.0038	0.0004
D2	D1→$CT(\bar{1}10)$	177.8375	87.9962	-89.8646
D3	D1→$CT(110)$	177.8375	87.9962	90.4818
D4	D2→$MT(010)$	-2.1625	92.0038	89.8646
D5	D4→$CT(\bar{1}10)$	177.8375	87.9962	0.2712
D6	D2→$MT(100)$	-2.1625	92.0038	90.4846
D7	D5→$MT(100)$	-2.1625	92.0038	0.3488
D8	D3→$MT(100)$	-2.1625	92.0038	90.1382
D9	D8→$MT(\bar{1}10)$	177.8375	87.9962	-0.0023
D10	D5→$TI((011)$	167.1886	1.4649	-169.3382

Table 6.1: The mutual orientation and the relation of the domains inside the sample at the C initial state obtained from the analysis of X-ray diffraction data. The labels: $CT(hkl)$ compound twinning, $MT(hkl)$ modulation twinning and $TI(hkl)$ twinning of type I over the crystallographic plane (hkl), $TII[uvw]$ twinning of type II along the crystallographic direction $[uvw]$ (see the Section 1.2.2)

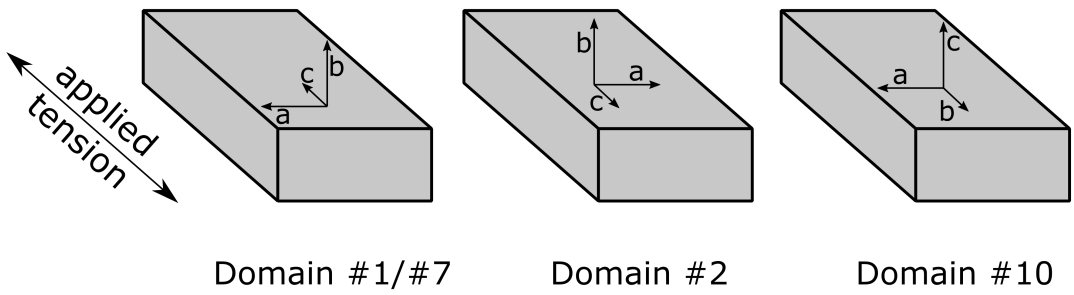

Figure 6.12: The sketch of the orientation of the domains corresponding to the highest intensity in the map 260 measured for the C initial case

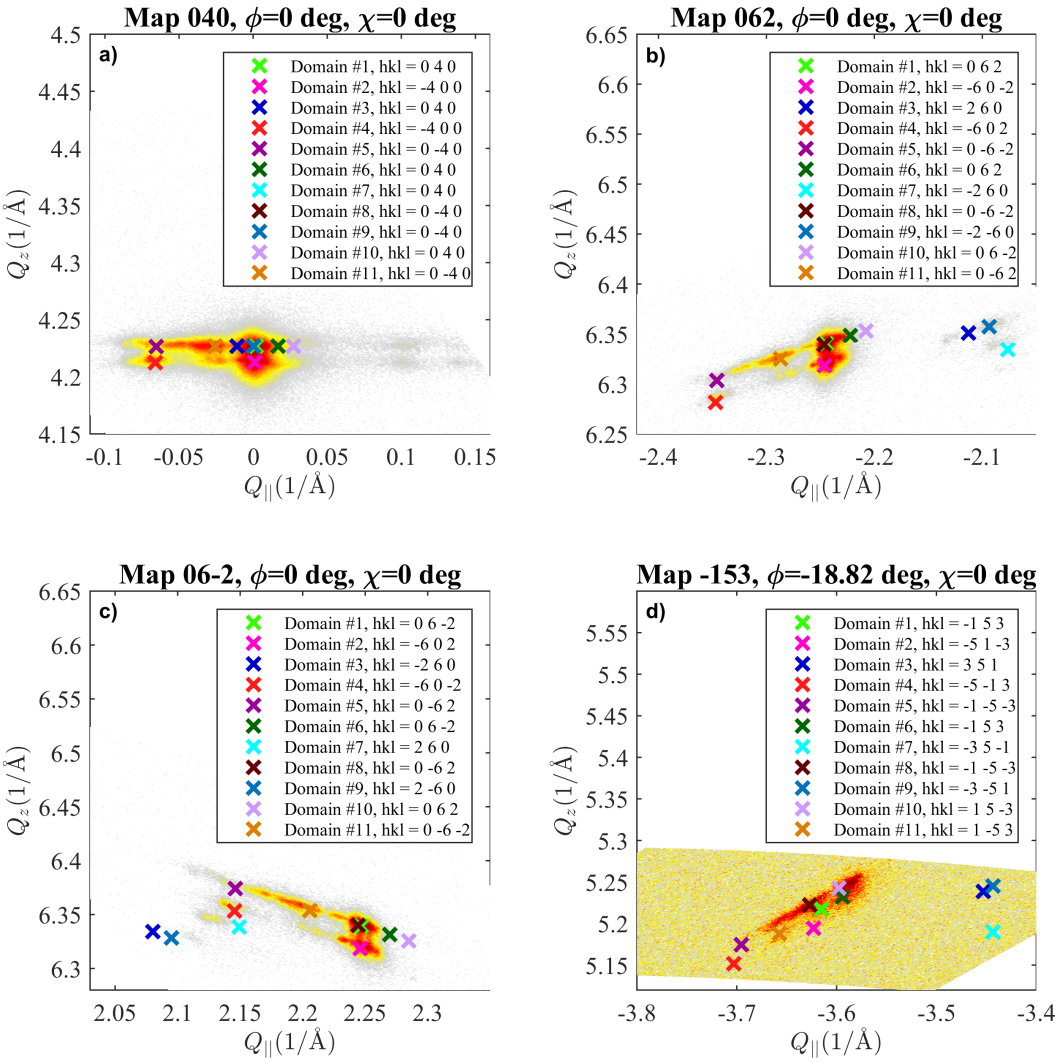

Figure 6.13: The reciprocal space maps measured at the A/B initial state of the sample at 0 MPa

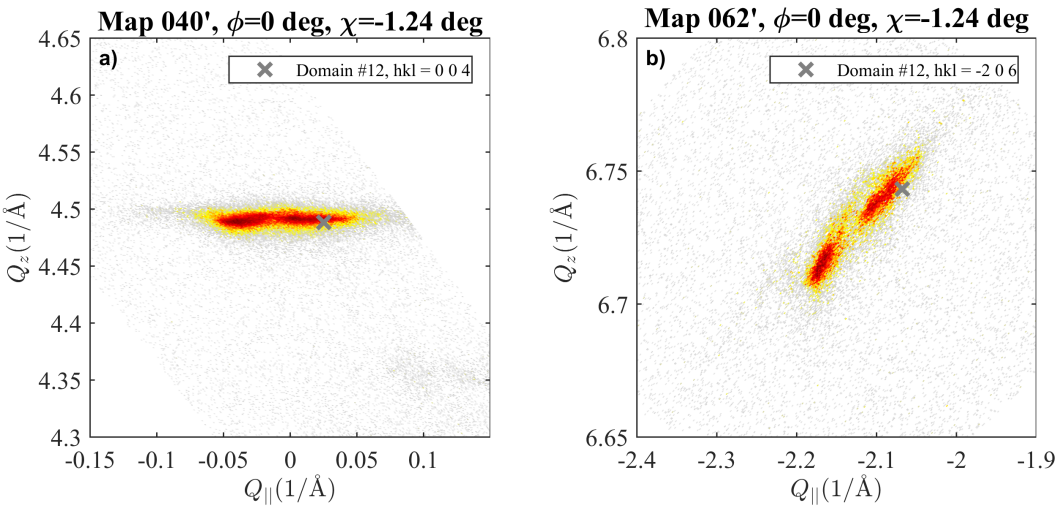

Figure 6.14: The reciprocal space maps corresponding to the domain with the c axis out of plane of the sample measured at the A/B initial state of the sample at 0 MPa

domain label	domain relation	Euler angle A (deg)	Euler angle B (deg)	Euler angle Γ (deg)
D1	reference domain	-94.7440	89.7900	176.5588
D2	D1→$CT(110)$	85.2560	90.2100	-86.0076
D3	D1→$CT(1\bar{1}0)$→ $TI(011)$ →$CT(1\bar{1}0)$	-8.2060	93.5884	179.7395
D4	D3→$CT(110)$→$MT(010)$ →$TI(101)$→$CT(110)$	-94.6091	90.7097	-93.3596
D5	D4→$CT(1\bar{1}0)$	85.3909	89.2903	3.5259
D6	D3→$TI(101)$	-94.5402	89.6093	176.7394
D7	D1→$TI(101)$	178.8841	86.1932	-179.6713
D8	D1→$TII[0\bar{1}1]$ →$TI(0\bar{1}1)$	84.8974	90.2328	3.8214
D9	D8→$TII[\bar{1}01]$	-8.7613	93.7989	-0.4754
D10	D7→$TII[101]$	85.2786	90.5686	-176.2215
D11	D1→$TI(\bar{1}01)$→$MT(010)$ →$TII[101]$	-94.7666	90.1486	-3.7783
D12	D7→$TI(011)$	40.8622	0.4906	-41.9573

Table 6.2: The mutual orientation and the relation of the domains inside the sample at the A/B initial state obtained from the analysis of X-ray diffraction data. The labels: $CT(hkl)$ compound twinning, $MT(hkl)$ modulation twinning and $TI(hkl)$ twinning of type I over the crystallographic plane (hkl), $TII[uvw]$ twinning of type II along the crystallographic direction $[uvw]$ (see the Section 1.2.2)

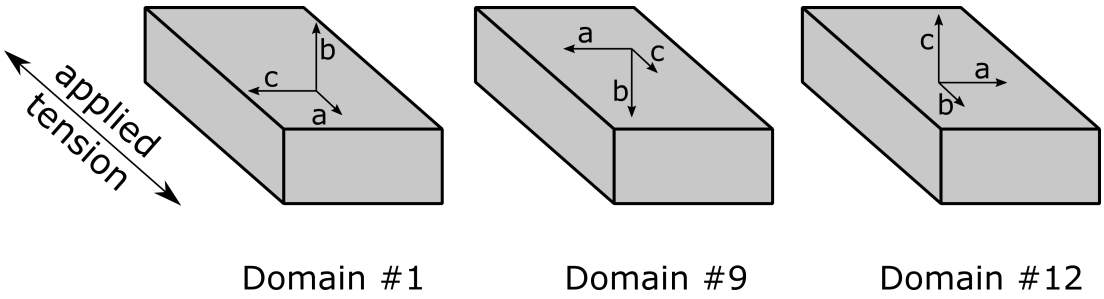

Figure 6.15: The sketch of the orientation of the domains corresponding to the highest intensity in the map 062 measured for the AB initial case

6.2.1 Lattice parameters

Next task was to determine the evolution of the lattice parameters with respect to the applied tension. The lattice parameters in both initial states C and A/B should be the same. With the indexed diffraction spots from previous section, we can fit the lattice parameters at the initial state from their 2Θ positions. With the assumption of monoclinic martensite unit cell we obtain:

$$a_0 = 5.9610(4)\ \text{Å} \quad b_0 = 5.9446(3)\ \text{Å} \quad c_0 = 5.596(2)\ \text{Å} \quad \gamma_0 = 90.31(3)\ \text{deg}$$

To estimate the overall elongation of the sample we look on the graph of the tensile stage position during the measurement shown in 6.16a. The working distance on the sample (the distance between the points where the sample was glued) was 4 mm. Therefore we can compute the relative elongation which is shown in Figure 6.16b. It can be seen that the higher relative elongation can be achieved with the C initial state. This is mostly due to the plateau at the beginning of the tension application which is caused by the creation of a/c and b/c twins and increment of their volume rather than elongation of lattice parameters of individual domains.

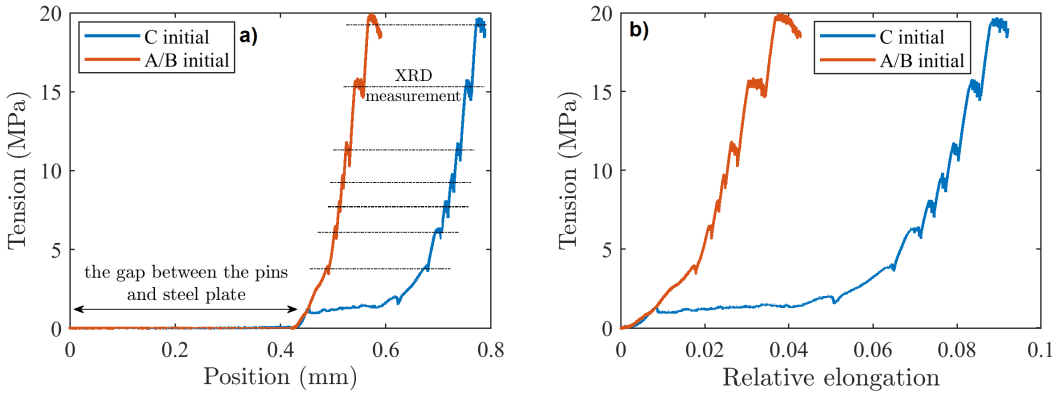

Figure 6.16: **a)** The position of the tensile stage during the experiment. The gap at the beginning of the graph corresponds to the gap between the pins and the steel plate (see Figure 2.6b) **b)** The relative elongation computed from the position of the tensile stage. The working distance of the sample was 4 mm.

To obtain lattice parameters from the diffraction data, the 2Θ positions of individual Bragg reflection spots should be fitted. There are the 2Θ profiles of 400/040/004 Bragg reflections for C initial sample in Figure 6.17 obtained from the reciprocal space maps by integration over ω angle. The profiles were fitted with the pseudo-Voigt functions and the lattice parameters a, b and c computed from the 2Θ positions of the peaks are shown in Figure 6.18. Since the diffraction spots corresponding to several domains lie on the same 2Θ position (see Figure 6.10a and 6.13a), these obtained parameters should correspond to an average value of the corresponding lattice parameters. These parameters also represent the axes with the direction perpendicular to the applied tension.

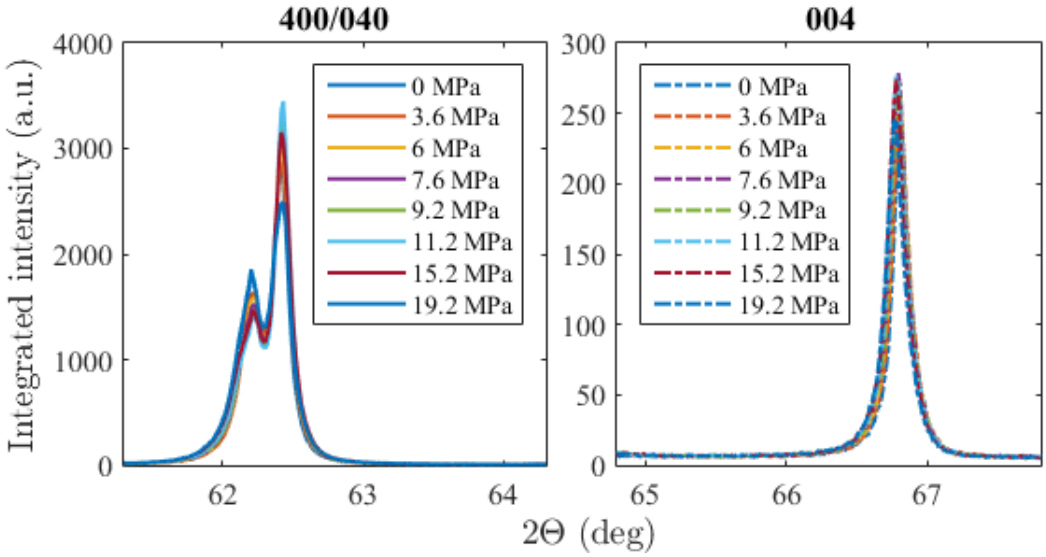

Figure 6.17: 2Θ profiles obtained by the integration over ω angle from maps of Bragg reflection 400/040 and 004 measured in A/B initial case

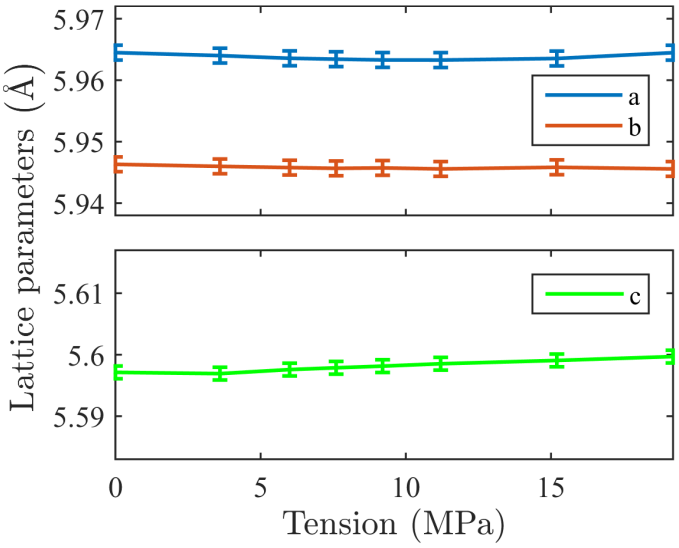

Figure 6.18: The lattice parameters evaluated from the 2Θ profiles shown in Figure 6.17

When we look closely to the parameters in Figure 6.18 we find out, that the relative change is in the order of 10^{-4} which is two orders lower than the elongation shown in Figure 6.16b. Moreover, the absolute change of the lattice parameters in Figure 6.18 is on the border of the sensitivity of the method (see the errorbars in Figure 6.18). The slight shift visible on c parameter is then probably caused mostly by the shift of the sample surface during the tension application and therefore the change in *sycos* correction. For that reasons, we will further neglect the change of the lattice parameters in the directions perpendicular to the direction of the applied tension.

Information of the change of the lattice parameters in the direction of applied tension is in Bragg reflection 351. With the use of both measurement for C and A/B initial cases and information of orientation and diffraction indices of individual domains we can determine the $a(p)$, $b(p)$, $c(p)$, $\gamma(p)$ tension dependencies. However, the rest of the measured reciprocal space maps can be used for the determination of *sycos* parameter (Equation 2.9).

The resulting dependencies are shown in Figure 6.19. - the lattice parameters in the direction of applied tension are elongated, as expected. The relative change of the lattice parameters from the A/B initial case corresponds to the overall relative change shown in Figure 6.16. The change from the C initial case corresponds to the elongation after the plateau in Figure 6.16. As it was said before, the plateau corresponds to the creation of the new a/c or b/c twins and increment of their volume. This should be manifested in the change of integrated intensity of the corresponding diffraction spots, which is connected to the irradiated volume. The integrated intensities from the map 260 (C initial case) and 062 (A/B initial case) are shown in Figure 6.20.

It is clearly seen for the C initial case that the intensity corresponding to domain D1 (c axis along the applied tension) between the measurement at 0 MPa and 3.6 MPa is clearly decreasing. This is accompanied by the increase of the intensity corresponding to domain D12 (b axis along the applied tension). On the other hand, the intensities corresponding to the individual domains during the measurement of A/B initial case are more or less at the same values and no rapid change is observed. Secondly, according to the results in Figure 6.19 and intensities in Figure 6.20 for A/B initial case it seems that the deformation caused by the applied tension happens mostly on the domains with the largest volumes - the most of them have the b axis along the tension.

6.2.2 Structure modulation

According to Section 1.1.3, the structure modulation is manifested by creation of the satellite diffraction spots with indices $hkl \pm n \cdot \vec{q}$, where n is integer and $\vec{q} = (0.4, 0.4, 0)$ is the modulation vector corresponding to 10M modulation. During the measurement of C initial case, several satellites were measured at the reciprocal/scattering plane with ϕ=0 deg rotation only (Figure 6.21). This means that the corresponding crystallographic axis a and b lies perpendicularly to the applied tension and therefore a change of the modulation parameters may be minimal.

Since the a and b in the A/B initial state lies out of plane of the sample surface or along the direction of applied tension, the satellites have to be achieved by the

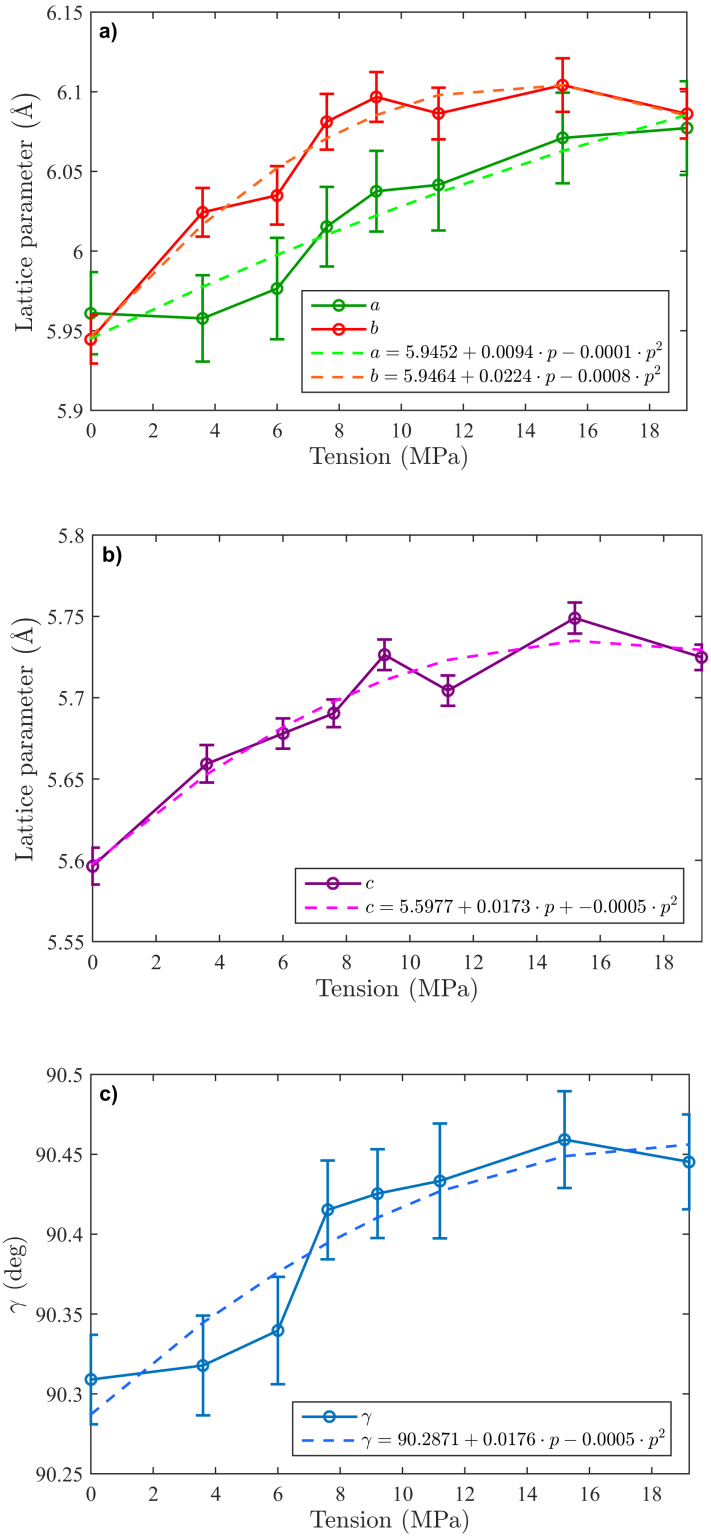

Figure 6.19: The dependence of the lattice parameters on tension

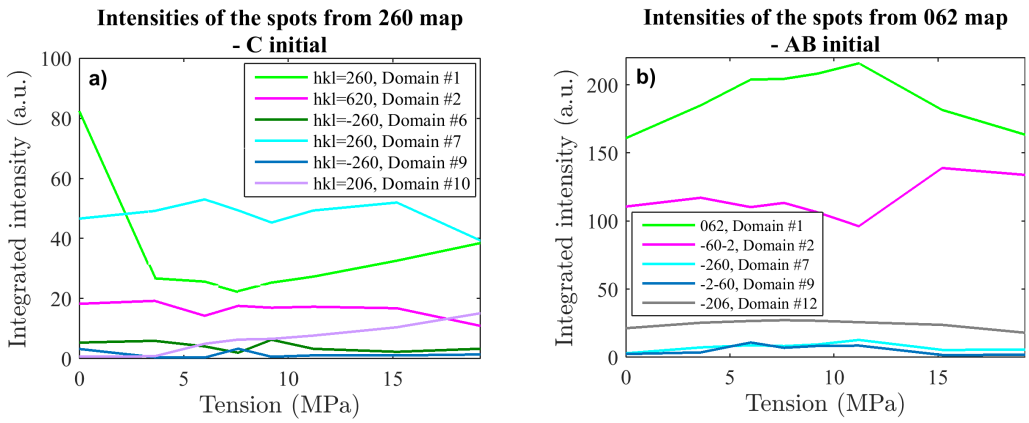

Figure 6.20: The integrated intensity of the peaks during the tension. The line colors correspond to the color of the crosses in Figures 6.10b, 6.11b, 6.13b and 6.14b **a)** the reciprocal space map 260 for C initial case **b)** the reciprocal space map 062 for A/B initial case

rotation in ϕ. The satellites accessed during the measurement in the A/B initial state at 0 MPa are shown in Figure 6.22.

Similarly to the low temperature measurement in Chapter 5, coordinates of the modulation vector were evaluated from 2Θ positions of the satellite diffraction spots. The modulation amplitude was estimated with the use of structure factor 2.26 and Equation 2.10. The resulting parameters are shown in Figure 6.23.

For both C and A/B initial cases, the modulation vector is constant within the range of errorbars and has the value corresponding to 10M modulation (see Figure 6.23a). The modulation amplitude in C initial case is also approximately constant as expected, because the modulation is on the crystallographic planes which are perpendicular to the direction of applied tension. The intensity of the satellites in A/B initial case monotonically decreases with the value of applied tension and therefore the evaluated modulation amplitude decreases as well (Figure 6.23b) towards the zero - the modulation vanishes.

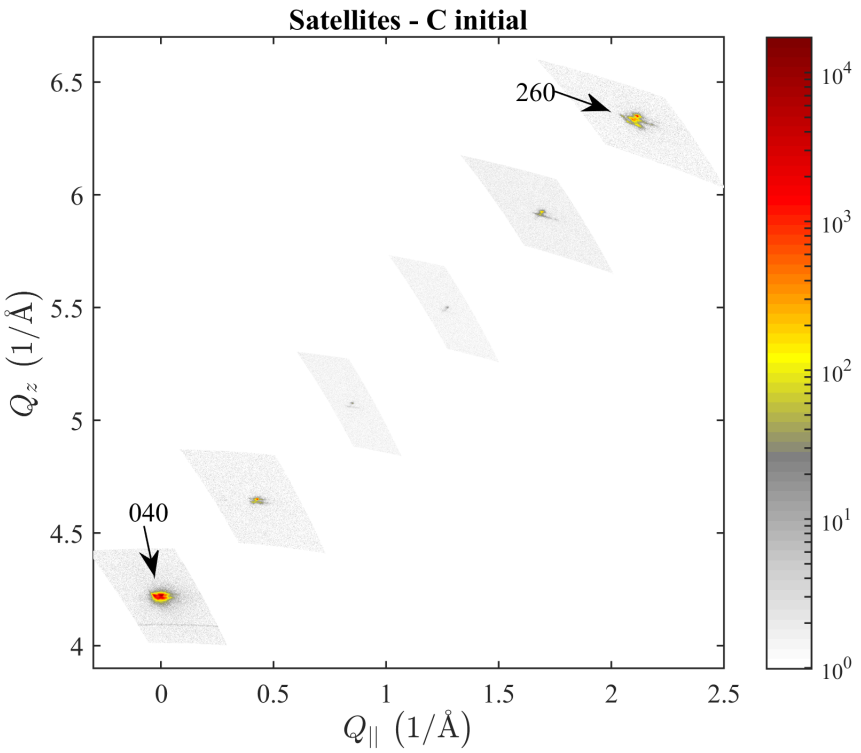

Figure 6.21: The satellite maxima measured on C initial sample at 0 MPa

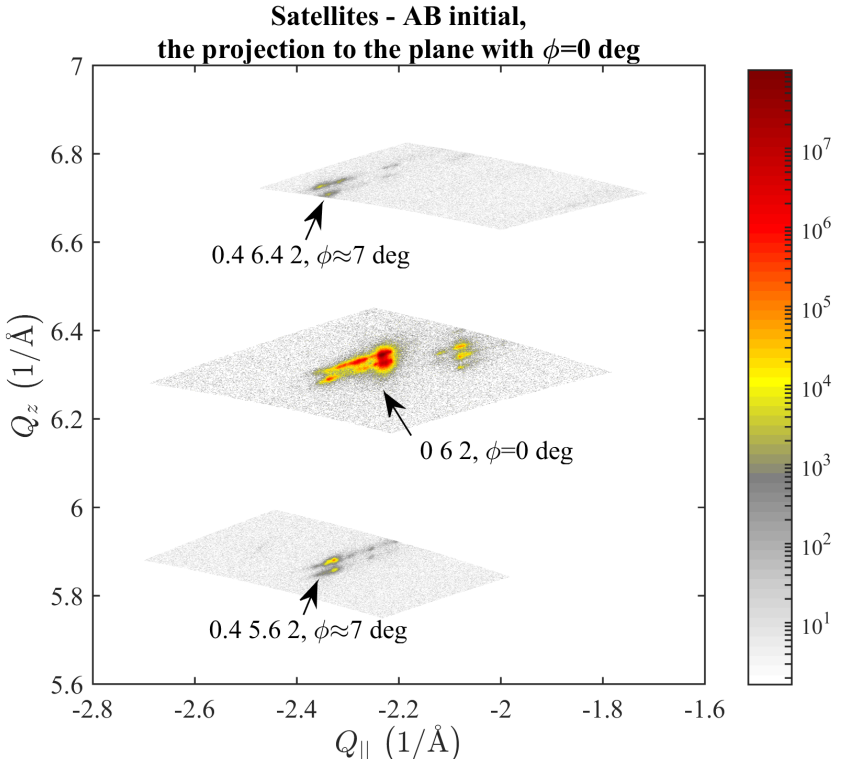

Figure 6.22: The satellite maxima measured on A/B initial sample at 0 MPa

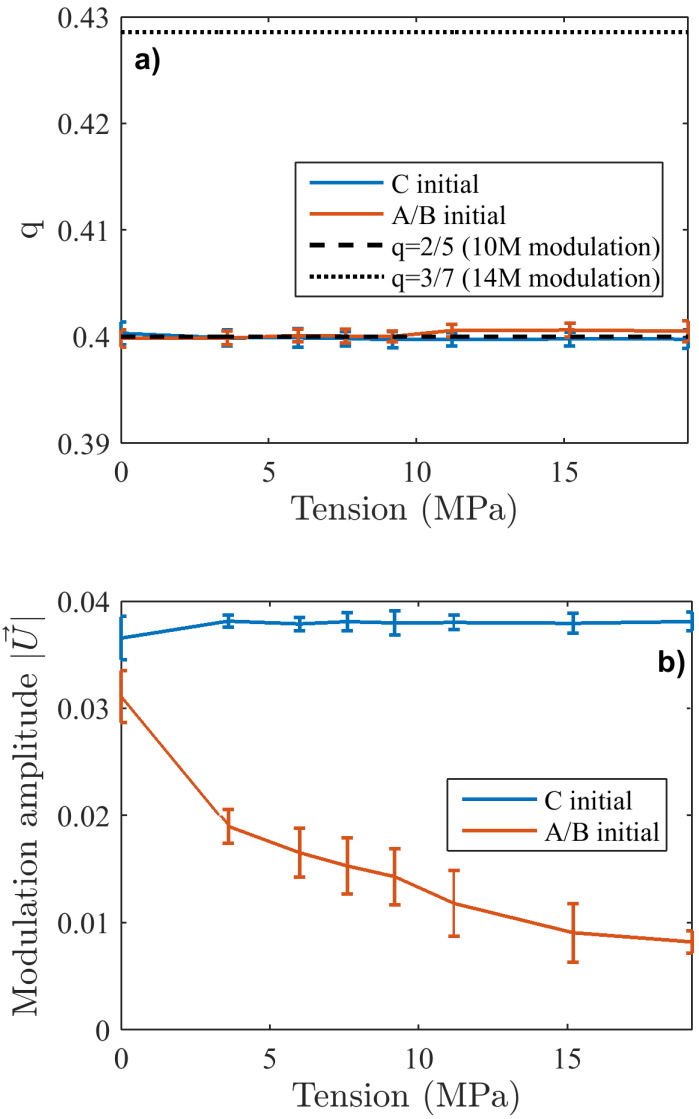

Figure 6.23: The modulation parameters obtained for both C and A/B initial cases. **a)** q-coordinate of the modulation vector $\vec{q}_{mod} = [q, q, 0]$ **b)** The length of the modulation amplitude vector $\vec{U} = [-u, u, 0]$

7. Discussion

Since the transformation temperatures of Ni-Mn-Ga related alloys are strongly compositional dependent, the influence of the concentration of individual elements on the transformation temperatures should be discussed at the first place. Let us focus on the $x - T$ phase diagram of the prepared $Ni_2MnGa_{1-x}In_x$ single crystals. According to the study of systematic trends of transformation temperatures published by Armstrong et al. [29], the increase of T_M in our samples is 54 K/at.%Ni and 30 K/at.%Mn. Taking into account the compositions following from XRF in Table 3.2, the biggest resulting shift of T_M (30 K) is for the sample $Ni_2MnGa_{0.98}In_{0.02}$. The T_M of the sample $Ni_2MnGa_{0.95}In_{0.05}$ should not be affected at all. In the samples with the higher indium concentration no martensitic transformation has been observed. The T_M for Ni_2MnGa sample is in good correspondence with previous results [15]. Therefore, the decreasing trend of T_M in Figure 5.6 is correct despite the fact that T_M for $Ni_2MnGa_{0.98}In_{0.02}$ has a large error caused by the effect of Ni and Mn concentration. According to [29], T_C of our samples within the studied concentrations should not be strongly influenced by the individual concentration of Ni and Mn.

Despite the compositional homogeneity of annealed samples showed by EDX measurement in Chapter 3, there could also remain possible inhomogeneities within the range of errorbars. This fact was proven for example by the magnetisation measurement. There is a temperature dependence of the magnetisation measured on one piece of the annealed NMG sample shown in Figure 7.1 (the measurement performed on a different piece of the sample than shown in Chapter 4). It is clearly seen that the martensitic transformation, shown here as the change of the magnetisation, consists of several steps. These steps can be ascribed to the sample grains with slightly different composition. The individual steps are within the temperature range of 10 K. Concerning the influence of individual elements concentration [29] mentioned in the previous paragraph, this would mean the difference of 0.19 at.%Ni or 0.33 at.%Mn which is bellow the errobar of EDX method.

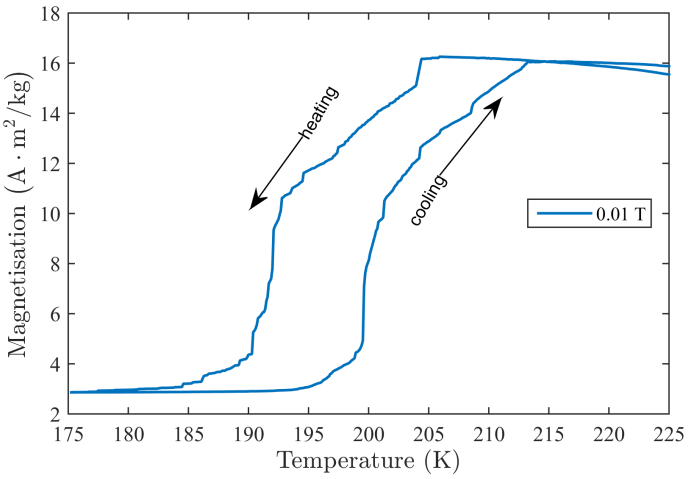

Figure 7.1: The temperature dependence of the magnetisation for one piece of Ni_2MnGa sample (a different piece than shown in Chapter 4)

The magnetisation measurements on Ni_2MnGa and $Ni_2MnGa_{0.95}In_{0.05}$ samples at various magnetic fields showed the systematic shift of martentensitic transformation temperatures and revealed non-trivial dependence of M_s and A_s in the low-field region. The slope of the dependences at high fields points to the decrease of the latent heat with the indium content. The latent heats obtained with the use of Claussius-Clapeyron equation 2.6 are $1.89 \cdot 10^3 \frac{\mathrm{J}}{\mathrm{kg}}$ for Ni_2MnGa and $0.29 \cdot 10^3 \frac{\mathrm{J}}{\mathrm{kg}}$ for $Ni_2MnGa_{0.95}In_{0.05}$. We performed several attempts to compare these values with the experiment. The latent heat of martensitic transformation of Ni_2MnGa has been obtained with the low temperature DSC measurement (shown in Figure 7.2). The corresponding value of latent heat for Ni_2MnGa is $1.83 \cdot 10^3 \frac{\mathrm{J}}{\mathrm{kg}}$ which is close to the value obtained from Claussius-Clapeyron equation. In Figure 7.2, one could also see the multiple peaks around the 200 K which could also corresponds to small compositional inhomogeneities discussed above. However, the measurement for $Ni_2MnGa_{0.95}In_{0.05}$ was not successful - the cooling is performed here with the liquid nitrogen ($T_{boil} = 77$ K) and it was not enough to cool the sample bellow the martensitic transformation.

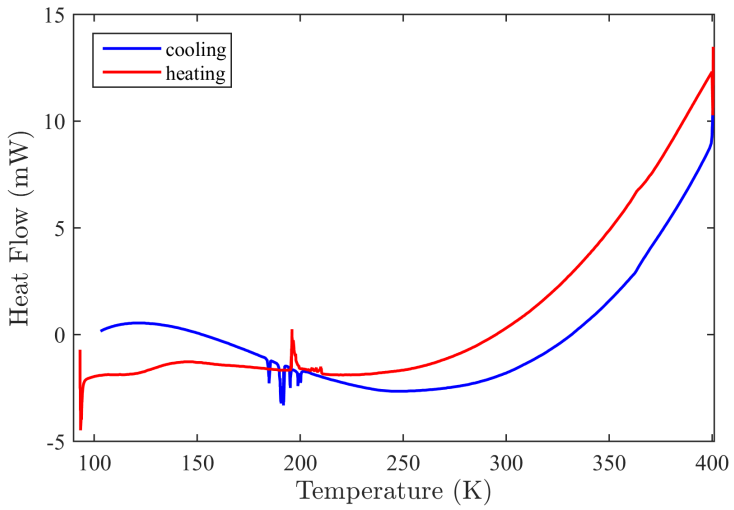

Figure 7.2: Low temperature DSC measurement on Ni_2MnGa

We performed also several attempts of the heat capacity measurement on this sample but it was unsuccessful as well (not shown). The transformation is so strong that the sample jumped from the sample platform everytime the sample crossed the transformation temperature (we tried to stick the sample with apiezon vacuum grease, with the GE glue and also with the STYCAST glue). Therefore, another option is to perform the pressure experiment and study the shift of T_M with respect to the applied pressure. One could expect the systematical shift of T_M in the range of 16.2 $\frac{\mathrm{K}}{\mathrm{GPa}}$ [64]. Then, we could obtain the latent heat from the results with the use of Claussius Clapeyron equation in the form 2.5. The change of the unit cell volume is known from the X-ray diffraction measurement in Chapter 5.

X-ray diffraction was proven as a unique probe for the detailed structural studies of Ni-Mn-Ga related samples as it was presented in Chapters 3, 5 and 6 when we were able to obtain the complete set of lattice parameters and information about the modulation. However, when counting with the integrated intensity the interpretation of data needs to be done very carefully.

As it was shown in Chapter 3, the evaluation of $L2_1$ content in the sample suffers primarily from the presence of a mosaicity and this causes the large errors of the calculated values. That is also the reason why it was impossible to determine the $L2_1$ content in the reference sample $NMG_{AdaptaMat}$ - the resulting value had a large statistical error and was non-physical (higher than 100 %). Due to this drawback, the only option is to count with overall intensity from each of individual reciprocal space map and measure many accessible diffraction spots to have a better statistics.

The low temperature diffraction studies presented in Chapter 5 could be improved with the option of having a monochromator in primary beam and the tilt axis on the sample stage. The presence of the monochromator could eliminate a possible error during the separation of individual diffraction spots (let us compare i.e. the maps in Figures 5.1 and 6.10b). The absence of a tilt axis causes problems during the alignment of asymmetric diffraction spots and makes it almost impossible to measure properly any Bragg reflection with the non-zero rotation in ϕ angle.

Concerning the X-ray diffraction measurement in tension, it needs to be mentioned that the tension values during the individual measurements were not constant and the sample was relaxing (see Figure 6.16). The corresponding error of the tension values is about 0.5 MPa. Therefore, we might have measured the sample in several slightly different states. But according to optical microscopy results, the biggest change in the sample happens mostly during the tension increase.

The long Ni-Mn-Ga sample for the tension experiment could represent the disadvantage of having larger amount of domains inside the sample. Of course, having of several twin domains is necessary to obtain for example enough information for the lattice parameters refinement. On the other hand, this makes the separation of individual diffraction peaks more difficult which plays a role when we count with the integrated intensities. For example, according to the measured reciprocal space maps 040 in Figure 6.10a and Figure 6.13a it seems impossible to separate all peaks. The presence of multiple domains could also lead to the intensity decrease of diffraction spots corresponding to individual domains. The twins may not lie directly on the sample surface. Or they are not irradiated when the angle of incidence and the sample orientation is not the same during the measurement of individual maps. This may be also the case for the satellites measured in A/B initial case (Figure 6.22). It is obvious from their position that they do not belong to the spots with the highest intensity in map 062.

The significant issue of the performed X-ray diffraction measurement in-situ in tension is the limitation in the rotation of the sample stage. Due to this drawback, the only Bragg reflection accessible at non-zero ϕ angle was 351. Because of its very low intensity, the fits of 2Θ-profiles of this Bragg reflection may have introduced a possible error in the resulting lattice parameters. The better option would be a possibility to rotate the stage at least 45 deg to reach Bragg reflection 422 which should have high enough intensity. Of course, the best option seems to be the possibility to rotate the stage for 90 deg to reach another 620 Bragg reflection. But the measurement of this diffraction spot may not be possible due to the fact that the stage at this orientation could shadow the primary or the diffracted beam.

The rotation limitation is also the issue for the measurement of the satellite diffraction spots in A/B initial case. The satellites lie on the plane perpendicular to the scattering plane with $\phi = 0$ deg and therefore the rotation in ϕ angle is necessary to access them. With the possibility of larger rotation we could access the satellites of the higher order and therefore we would have more information about the modulation. Although we found out a significant decrease in the modulation amplitude with the applied tension in the A/B initial case, with more information we could for example use more complex model for the modulation wave than single harmonic wave 2.25.

This discussion summarizes and realistically addresses possible weak points which we realized and had to face up during implementation of research tasks solved in this work. Despite all difficulties and circumstances discussed in this chapter we believe that theoretical approaches and experimental results presented in Chapters 2-6 contain the series of unique, valuable and complex results, have significant scientific potential and are of high interest for the scientific community.

Conclusion

The series of single crystalline $Ni_2MnGa_{1-x}In_x$ samples with different indium content were prepared by Bridgman method. The chemical composition of samples was measured by EDX and XRF. It was proved that a widely used 2 days of homogenization annealing is not enough to homogenize indium distribution in the samples. After 5 days of homogenization annealing at 1000°C the indium distribution is well homogenized.

We demonstrated that Ni_2MnGa single crystals can be grown from premelted precursors with a rapid speed 80 mm/h using the floating zone optical furnace. Moreover, without any seed the preferable orientation of the ingot was [100] along the growth axis. This provides a significant benefit since [100] orientation is the most suitable for MIR. Samples obtained with the fast growth in the floating zone contained composition inhomogeneities which were mostly eliminated by the annealing. The structural qualities of this sample were comparable to the sample prepared with Bridgman method and reference sample. Measurement of the intensity ratio of the 111 and 400 diffractions revealed that the annealing resulted in approximately full $L2_1$ ordering. The reported method of Ni_2MnGa single crystal preparation by floating zone technique may improve the effectiveness and speed of production of these materials and enhance a possibility for a future research. However, the preparation of the samples with indium with the floating zone method was not successful.

The measurements of temperature dependence of the electrical resistivity and the magnetisation were performed to obtain the values of the critical temperatures. The resulting values were put together with the results of low temperature diffraction and the $x - T$ phase diagram was constructed. Contrary to results published earlier on polycrystalline samples [34], the temperature of martensitic transformation decreases much faster with increasing indium content. The transformation was not observed in the samples with the indium content $x > 0.05$ (the transformation should be suppressed at $x \approx 0.10$ according to the phase diagram). The discrepancy between the results obtained from polycrystalline samples and single crystals can be caused by the preparation procedure which can leave the residual stresses inside the sample and influence the critical temperatures.

The X-ray diffraction measurements have shown the clear dependence of the lattice parameters on the indium content. Indium doping obviously increases the unit cell volume. Moreover, indium increases also the volume change during the martensitic transformation. The structural modulation is influenced by the indium doping as well, since the increasing indium content increases the length of the modulation vector in the pre-martensitic phase and decreases its length in the martensite.

The temperature dependences of magnetisation at different magnetic fields for the samples Ni_2MnGa and $Ni_2MnGa_{0.95}In_{0.05}$ were measured. The martensitic transformation temperature is significantly shifted with the increasing magnetic field in Ni_2MnGa and also in $Ni_2MnGa_{0.95}In_{0.05}$ sample. M_s decreases about 5 K at low fields for both compounds and it starts to increase again above in higher fields. The indium doping influences the position of M_s minimum with respect

to the applied field – the minimum lies approximately at 0.5 T and 1.5 T for Ni_2MnGa and $Ni_2MnGa_{0.95}In_{0.05}$, respectively. This effect is caused by the energetic preferability between martensite and austenite based on magnetic energy of both phases with respect to the applied magnetic field. However, the amount of indium inside our $Ni_2MnGa_{0.95}In_{0.05}$ single crystal is obviously not enough to create a negative slope of $M_s(H)$ dependence in the high field region seen for example in [46]. A_s increases almost all the time with the field. In the fields above 2 T, the dependences have approximately a linear behaviour and the slopes of this dependences can be used for the latent heat evaluation. Putting of the resulting slopes of $M_s(H)$ at high fields into Clausius-Clapeyron equation suggests that indium decreases the latent heat of the martensitic transformation and it is $1.89 \cdot 10^3 \ \frac{\mathrm{J}}{\mathrm{kg}}$ for Ni_2MnGa and $0.29 \cdot 10^3 \ \frac{\mathrm{J}}{\mathrm{kg}}$ for $Ni_2MnGa_{0.95}In_{0.05}$.

The resulting rapid decay of $M_s(H)$ at the low fields has not been reported before, since most of the studies presented only the comparison between low and high fields (two points). The decay occurs due to the fact, that the magnetisation of the martensitic phase at a low fields is smaller than in austenite (or pre-martensite). Therefore, the corresponding energy of martensite is higher and austenitic (or pre-martensitic) phase is energetically preferable.

The measurement of the electrical resistivity temperature dependence at different magnetic fields revealed the shift of the pre-martensitic transformation temperature T_P. The slope of the shift is approximately $0.64 \ \frac{\mathrm{K}}{\mathrm{T}}$ for NMG sample and $0.53 \ \frac{\mathrm{K}}{\mathrm{T}}$ for NMGIn5 sample respectively.

The last part of the thesis was dedicated to the measurement of X-ray diffraction in-situ in an applied tension on the off-stoichiometric sample $Ni_{50}Mn_{28}Ga_{22}$, which is in the martensitic phase at a room temperature. From the study performed for two different initial states of the sample obtained by defined pressing, the evolution of the lattice parameters was obtained. If the initial state corresponds to the *c*-axis (the shortest) along the direction of the applied tension the elongation of the sample is done primarily by the induced reorientation - it means by the creation of the new domains suitably oriented to the tension (*a* and *b* axis along the tension) and increasing of their volume. When the volumes of these domains cannot be further increased, the sample elongation is realized by the increase of lattice parameters.

If the initial state corresponds to the situation when mostly *a* and *b* axes lie along the direction of applied tension, the overall elongation happens primarily due to the change of the lattice parameters.

The applied tension also influences the modulation parameters. When *a* and *b* axis lie perpendicularly to the direction of tension, the observable change in their lengths and in modulation is within the range of errorbars. If *a* or *b* lie along the direction of tension, the modulation vector remains also the same, but the modulation amplitude rapidly decreases.

The behaviour of the twin (domain) boundaries motion is influenced by the sample arrangement and the way, how it is attached to the sample holder. The glue is definitely able to stop the domain boundaries motion and can prevent the sample from the whole reorientation. First, it could be seen during the measurement of the magnetisation hysteresis loops - during the martensitic transformation, $Ni_2MnGa_{0.95}In_{0.05}$ sample transformed into the variant corresponding to the hard axis (*a* or *b*) along the direction of the field. MIR did not occur during

the whole measurement of hysteresis loop and the sample remained at the same state. Second, the similar situation was observed during the X-ray diffraction measurement in tension. During the tensile measurement with the glued sample, the full MIR din not occur and the twin boundaries motion was probably blocked by the glue. Contrary, in the preliminary measurement when the sample was held directly by the clamps, the specimen transformed almost fully to variant with c axis out of plane.

This work was a pilot study concerning the preparation and finding of the ideal conditions for the single crystal growth of indium doped Ni_2MnGa shape-memory alloys. The physical properties of prepared samples were studied in detail. A special emphasis was put on the examination of the changes in the real structure in the dependence of temperature, composition and various external conditions such as the application of a magnetic field or tension. It has to be mentioned at this place that nearly all of the measurements presented in this work were performed in our laboratory. This means with the use of standard laboratory equipment (although top level devices). It was necessary to create and to verify the measurement methodology of the theoretical models for the structure description of these materials. Obtained knowledge and experiences can in future serve as a good starting point to more complex, dedicated measurements - for example a detailed study of structure and microstructure of these or analogous materials with the use of advanced synchrotron sources.

Bibliography

[1] A. R. Smith, A. Saren, J. Järvinen, and K. Ullakko. Characterization of a high resolution solid state micropump that can be integrated into microfluidic systems. *Microfluidics and Nanofluidics*, 18:1255–1263, 2015.

[2] Anthony Hobza, Charles L. Patrick, Kari Ullakko, Nader Rafla, Paul Lindquist, and Peter Müllner. Sensing strain with Ni-Mn-Ga. *Sensors and Actuators A: Physical*, 269:137 – 144, 2018.

[3] V. Franco, J.S. Blázquez, J.J. Ipus, J.Y. Law, L.M. Moreno-Ramírez, and A. Condev. Magnetocaloric effect: From materials research to refrigeration devices. *Progress in Materials Science*, 93:112 – 232, 2018.

[4] O. Heczko, N. Scheerbaum, and O. Gutfleisch. *Magnetic Shape Memory Phenomena*, page 399. Springer, US, 2009.

[5] K. Ullakko, J. K. Huang, C. Kantner, R. C. O'Handley, and V. V. Kokorin. Large magnetic-field-induced strains in Ni_2MnGa single crystals. *Applied Physics Letters*, 69(13):1966–1968, 1996.

[6] A. Sozinov, N. Lanska, A. Soroka, and W. Zou. 12% magnetic field-induced strain in Ni-Mn-Ga-based non-modulated martensite. *Applied Physics Letters*, 102(2):021902, 2013.

[7] AA Likhachev, A. Sozinov, and K. Ullakko. Magneto-mechanical cycling and modeling the external stress effect on the magnetic-field-controlled strain response in Ni-Mn-Ga. *Journal de Physique IV*, 115:95–103, 2004.

[8] D. Kellis, A. Smith, K. Ullakko, and P. Müllner. Oriented single crystals of Ni–Mn–Ga with very low switching field. *Journal of Crystal Growth*, 359:64 – 68, 2012.

[9] L. Righi, F. Albertini, L. Pareti, A. Paoluzi, and G. Calestani. Commensurate and incommensurate "5M" modulated crystal structures in Ni–Mn–Ga martensitic phases. *Acta Materialia*, 55(15):5237 – 5245, 2007.

[10] S. Singh, V. Petricek, P. Rajput, A. H. Hill, E. Suard, S. R. Barman, and D. Pandey. High-resolution synchrotron X-ray powder diffraction study of the incommensurate modulation in the martensite phase of Ni_2MnGa: Evidence for nearly 7M modulation and phason broadening. *Physical Review B*, 90(1):014109, Jul 2014.

[11] V.V. Martynov and V.V. Kokorin. The crystal structure of thermally- and stress-induced martensites in Ni_2MnGa single crystals. *Journal de Physique III*, 2(5):739–749, 1992.

[12] Lara Righi, Franca Albertini, Gianluca Calestani, Luigi Pareti, Antonio Paoluzi, Clemens Ritter, Pedro A. Algarabel, Luis Morellon, and M. Ricardo Ibarra. Incommensurate modulated structure of the ferromagnetic shape-memory Ni_2MnGa martensite. *Journal of Solid State Chemistry*, 179(11):3525 – 3533, 2006.

[13] V.A. Chernenko, J. Pons, E. Cesari, and K. Ishikawa. Stress–temperature phase diagram of a ferromagnetic Ni–Mn–Ga shape memory alloy. *Acta Materialia*, 53(19):5071 – 5077, 2005.

[14] U. Gaitzsch, M. Pötschke, S. Roth, N. Mattern, B. Rellinghaus, and L. Schultz. Structure formation in martensitic $Ni_{50}Mn_{30}Ga_{20}$ MSM alloy. *Journal of Alloys and Compounds*, 443(1):99 – 104, 2007.

[15] P. J. Webster, K. R. A. Ziebeck, S. L. Town, and M. S. Peak. Magnetic order and phase transformation in Ni_2MnGa. *Philosophical Magazine B*, 49(3):295–310, 1984.

[16] Gregory B. Olson. *Martensite*. ASM International, 1992.

[17] A. Sozinov, A.A. Likhachev, N. Lanska, O. Söderberg, K. Ullakko, and V.K. Lindroos. Stress- and magnetic-field-induced variant rearrangement in Ni–Mn–Ga single crystals with seven-layered martensitic structure. *Materials Science and Engineering: A*, 378(1):399 – 402, 2004. European Symposium on Martensitic Transformation and Shape-Memory.

[18] N. Lanska, O. Söderberg, A. Sozinov, Y. Ge, K. Ullakko, and V. K. Lindroos. Composition and temperature dependence of the crystal structure of Ni–Mn–Ga alloys. *Journal of Applied Physics*, 95(12):8074–8078, 2004.

[19] Oleg Heczko, Petr Cejpek, Jan Drahokoupil, and Václav Holý. Structure and microstructure of Ni-Mn-Ga single crystal exhibiting magnetic shape memory effect analysed by high resolution X-ray diffraction. *Acta Materialia*, 115:250 – 258, 2016.

[20] V.V. Khovailo, T. Takagi, A.N. Vasilev, H. Miki, M. Matsumoto, and R. Kainuma. On order–disorder (L21-B2') phase transition in $Ni_{2+x}Mn_{1-x}Ga$ Heusler alloys. *Physica status solidi (a)*, 183(2):R1–R3, 2001.

[21] Sanjay Singh, J. Bednarcik, S. R. Barman, C. Felser, and Dhananjai Pandey. Premartensite to martensite transition and its implications for the origin of modulation in Ni_2MnGa ferromagnetic shape-memory alloy. *Physical Review B*, 92:054112, Aug 2015.

[22] J. Kübler, A. R. William, and C. B. Sommers. Formation and coupling of magnetic moments in Heusler alloys. *Physical Review B*, 28:1745–1755, Aug 1983.

[23] Z. H. Liu, M. Zhang, W. Q. Wang, W. H. Wang, J. L. Chen, G. H. Wu, F. B. Meng, H. Y. Liu, B. D. Liu, J. P. Qu, and Y. X. Li. Magnetic properties and martensitic transformation in quaternary Heusler alloy of NiMnFeGa. *Journal of Applied Physics*, 92(9):5006–5010, 2002.

[24] Chun-Mei Li, Hu-Bin Luo, Qing-Miao Hu, Rui Yang, Börje Johansson, and Levente Vitos. Site preference and elastic properties of Fe-, Co-, and Cu-doped Ni_2MnGa shape memory alloys from first principles. *Physical Review B*, 84:024206, Jul 2011.

[25] D.E. Soto-Parra, X. Moya, L. Mañosa, A. Planes, H. Flores-Zúñiga, F. Alvarado-Hernández, R.A. Ochoa-Gamboa, J.A. Matutes-Aquino, and D. Ríos-Jara. Fe and Co selective substitution in Ni_2MnGa: Effect of magnetism on relative phase stability. *Philosophical Magazine*, 90(20):2771–2792, 2010.

[26] Chengbao Jiang, Jingmin Wang, Panpan Li, Ao Jia, and Huibin Xu. Search for transformation from paramagnetic martensite to ferromagnetic austenite: NiMnGaCu alloys. *Applied Physics Letters*, 95(1):012501, 2009.

[27] X. Jin, M. Marioni, D. Bono, S. M. Allen, R. C. O'Handley, and T. Y. Hsu. Empirical mapping of Ni–Mn–Ga properties with composition and valence electron concentration. *Journal of Applied Physics*, 91(10):8222–8224, 2002.

[28] Kenichi Yamaguchi, Shoji Ishida, and Setsuro Asano. Valence electron concentration and phase transformations of shape memory alloys Ni–Mn–Ga–X. *Materials Transactions*, 44:204–210, 01 2003.

[29] A. Armstrong, F. Nilsén, M. Rameš, Colman R. H., Veřtát P., Kmječ T., Straka L., Müllner P., and Heczko O. Systematic trends of transformation temperatures and crystal structure of Ni–Mn–Ga–Fe–Cu alloys. *Shape Memory and Superelasticity*.

[30] Aleksandr N. Vasil'ev, Vasilii D. Buchel'nikov, T. Takagi, Vladimir V. Khovailo, and Emmanuil I. Estrin. Shape memory ferromagnets. *Physics-Uspekhi*, 46(6):559–588, Jun 2003.

[31] R. Kainuma, Y. Imano, W. Ito, Y. Sutou, H. Morito, S. Okamoto, O. Kitakami, K. Oikawa, A. Fujita, T. Kanomata, and K. Ishida. Magnetic-field-induced shape recovery by reverse phase transformation. *Nature*, 439:957–960, 2006.

[32] O. Heczko, M. Thomas, R. Niemann, L. Schultz, and S. Fähler. Magnetically induced martensite transition in freestanding epitaxial Ni–Mn–Ga films. *Applied Physics Letters*, 94(15):152513, 2009.

[33] Zongbin Li, Yudong Zhang, C. F. Sánchez-Valdés, J. L. Sánchez Llamazares, Claude Esling, Xiang Zhao, and Liang Zuo. Giant magnetocaloric effect in melt-spun Ni-Mn-Ga ribbons with magneto-multistructural transformation. *Applied Physics Letters*, 104(4):044101, 2014.

[34] Mahmud Khan, Igor Dubenko, Shane Stadler, and Naushad Ali. Magnetic and structural phase transitions in Heusler type alloys $Ni_2MnGa_{1-x}In_x$. *Journal of Physics: Condensed Matter*, 16(29):5259–5266, Jul 2004.

[35] Petr Cejpek, Petr Doležal, Petr Opletal, Jaroslav Valenta, Kristina Vlášková, and Milan Dopita. Temperature versus composition phase diagram and temperature evolution of structure and modulation of $Ni_2MnGa_{1-x}In_x$ single crystals. *Journal of Alloys and Compounds*, 855:157327, 2021.

[36] V. K. Sharma, M. K. Chattopadhyay, and S. B. Roy. Large inverse magnetocaloric effect in $Ni_{50}Mn_{34}In_{16}$. *Journal of Physics D: Applied Physics*, 40(7):1869–1873, Mar 2007.

[37] F. Kitanishi, K. Nakamura, T. Akiyama, and I. Tomonori. Structural and elastic properties of the magnetic shape memory $Ni_2MnGa_{1-x}In_x$ alloy. *Journal of the Korean Physical Society*, 63:329–332, 2013.

[38] Baris Emre, Süheyla Yüce, Enric Stern-Taulats, Antoni Planes, Simone Fabbrici, Franca Albertini, and Lluís Mañosa. Large reversible entropy change at the inverse magnetocaloric effect in Ni-Co-Mn-Ga-In magnetic shape memory alloys. *Journal of Applied Physics*, 113(21):213905, 2013.

[39] F. Puglielli, V. Mussi, F. Cugini, Amadè N. Sarzi, M. Solzi, C. Bennati, S. Fabbrici, and F. Albertini. Scale-up of magnetocaloric NiCoMnIn Heuslers by powder metallurgy for room temperature magnetic refrigeration. *Frontiers in Energy Research*, 7:150, 2020.

[40] G. Cavazzini, F. Cugini, M.E. Gruner, C. Bennati, L. Righi, S. Fabbrici, F. Albertini, and M. Solzi. Tuning the magnetic and magnetocaloric properties of austenitic Ni-Mn-(In,Sn) heuslers. *Scripta Materialia*, 170:48 – 51, 2019.

[41] S. Fabbrici, G. Porcari, F. Cugini, M. Solzi, J. Kamarad, Z. Arnold, R. Cabassi, and F. Albertini. Co and In doped Ni-Mn-Ga magnetic shape memory alloys: A Thorough structural, magnetic and magnetocaloric study. *Entropy*, 16:2204–2222, 2014.

[42] I. Glavatskyy, N. Glavatska, O.Soderberg, S.-P. Hannula, and J.-U. Hoffmann. Transformation temperatures and magnetoplasticity of Ni–Mn–Ga alloyed with Si, In, Co or Fe. *Scripta Materialia*, 54:1891–1895, 2006.

[43] Daniel Bourgault, Jérémy Tillier, Pierre Courtois, Denis Maillard, and Xavier Chaud. Large inverse magnetocaloric effect in $Ni_{45}Co_5Mn_{37.5}In_{12.5}$ single crystal above 300 K. *Applied Physics Letters*, 96(13):132501, 2010.

[44] L. Huang, D. Y. Cong, L. Ma, Z. H. Nie, Z. L. Wang, H. L. Suo, Y. Ren, and Y. D. Wang. Large reversible magnetocaloric effect in a Ni-Co-Mn-In magnetic shape memory alloy. *Applied Physics Letters*, 108(3):032405, 2016.

[45] L. Chen, F. X. Hu, J. Wang, L. F. Bao, J. R. Sun, B. G. Shen, J. H. Yin, and L. Q. Pan. Magnetoresistance and magnetocaloric properties involving strong metamagnetic behavior in Fe−doped $Ni_{45}Co_{1-x}Fe_xMn_{36.6}In_{13.4}$ alloys. *Applied Physics Letters*, 101(1):012401, 2012.

[46] Thorsten Krenke, Mehmet Acet, Eberhard F. Wassermann, Xavier Moya, Lluís Mañosa, and Antoni Planes. Ferromagnetism in the austenitic and martensitic states of Ni−Mn−In alloys. *Physical Review B*, 73:174413, May 2006.

[47] S. Fabbrici, J. Kamarad, Z. Arnold, F. Casoli, A. Paoluzi, F. Bolzoni, R. Cabassi, M. Solzi, G. Porcari, C. Pernechele, and F. Albertini. From direct to inverse giant magnetocaloric effect in Co-doped NiMnGa multifunctional alloys. *Acta Materialia*, 59(1):412–419, 2011.

[48] A.A. Mendonça, J.F. Jurado, S.J. Stuard, L.E.L. Silva, G.G. Eslava, L.F. Cohen, L. Ghivelder, and A.M. Gomes. Giant magnetic-field-induced strain in Ni_2MnGa-based polycrystal. *Journal of Alloys and Compounds*, 738:509–514, 2018.

[49] Tanja Graf, Claudia Felser, and Stuart S.P. Parkin. Simple rules for the understanding of heusler compounds. *Progress in Solid State Chemistry*, 39(1):1 – 50, 2011.

[50] Petr Cejpek. X-ray diffraction and diffuse scattering from Heusler alloys. Diploma thesis, Charles University, Prague, 2015.

[51] Petr Cejpek, Ladislav Straka, Martin Veis, Ross Colman, Milan Dopita, Václav Holý, and Oleg Heczko. Rapid floating zone growth of Ni_2MnGa single crystals exhibiting magnetic shape memory functionality. *Journal of Alloys and Compounds*, 775:533 – 541, 2019.

[52] Y. Ge, H. Jiang, A. Sozinov, O. Söderberg, N. Lanska, J. Keränen, E.I. Kauppinen, V.K. Lindroos, and S.-P. Hannula. Crystal structure and macrotwin interface of five-layered martensite in Ni–Mn–Ga magnetic shape memory alloy. *Materials Science and Engineering: A*, 438-440:961 – 964, 2006. Proceedings of the International Conference on Martensitic Transformations.

[53] A. Zheludev, S. M. Shapiro, P. Wochner, and L. E. Tanner. Precursor effects and premartensitic transformation in ni_2MnGa. *Physical Review B*, 54:15045–15050, Dec 1996.

[54] V.A. Chernenko, E. Cesari, V.V. Kokorin, and I.N. Vitenko. The development of new ferromagnetic shape memory alloys in Ni-Mn-Ga system. *Scripta Metallurgica et Materialia*, 33(8):1239 – 1244, 1995.

[55] V V Khovailo, T Takagi, A D Bozhko, M Matsumoto, J Tani, and V G Shavrov. Premartensitic transition in $Ni_{2+x}Mn_{1-x}Ga$ Heusler alloys. *Journal of Physics: Condensed Matter*, 13(42):9655–9662, oct 2001.

[56] Cesari E. Seguí, C. and J. Pons. Intermartensitic transformations in ni-mn-ga alloys: A general view. *Advanced Materials Research*, 52:47–55, 2008.

[57] V.V. Kokorin, A.O. Perekos, A.A. Tshcherba, O.M. Babiy, and T.V. Efimova. Intermartensitic phase transitions in Ni–Mn–Ga alloy, magnetic field effect. *Journal of Magnetism and Magnetic Materials*, 302(1):34 – 39, 2006.

[58] Aslı Çakır, Lara Righi, Franca Albertini, Mehmet Acet, Michael Farle, and Selçuk Aktürk. Extended investigation of intermartensitic transitions in Ni-Mn-Ga magnetic shape memory alloys: A detailed phase diagram determination. *Journal of Applied Physics*, 114(18):183912, 2013.

[59] Sebastian Faehler. An introduction to actuation mechanisms of magnetic shape memory alloys. In *ECS Transactions*. ECS, 2007.

[60] Ladislav Straka and Oleg Heczko. Magnetic anisotropy in Ni–Mn–Ga martensites. *Journal of Applied Physics*, 93(10):8636–8638, 2003.

[61] L. Straka, H. Hänninen, and O. Heczko. Temperature dependence of single twin boundary motion in Ni–Mn–Ga martensite. *Applied Physics Letters*, 98(14):141902, 2011.

[62] L. Straka and O. Heczko. Superelastic response of Ni-Mn-Ga martensite in magnetic fields and a simple model. *IEEE Transactions on Magnetics*, 39(5):3402–3404, 2003.

[63] M. Thomas, O. Heczko, J. Buschbeck, L. Schultz, and S. Fähler. Stress induced martensite in epitaxial Ni–Mn–Ga films deposited on MgO(001). *Applied Physics Letters*, 92(19):192515, 2008.

[64] Hidefumi Maeda, Takashi Fukuda, and Tomoyuki Kakeshita. Effect of hydrostatic pressure on martensitic transformation in a ferromagnetic shape memory alloy Ni_2MnGa. *Journal of Alloys and Compounds*, 509(30):7840 – 7843, 2011.

[65] B. A. Bilby and A. G. Crocker. A general method to determine twinning elements. *Proceedings of the Royal Society of London A*, 288:240–255, 1965.

[66] Zhang Y., Li Z., Esling C., Muller J., Zhao X., and Zuo L. A general method to determine twinning elements. *Journal of applied crystallography*, 43:1426–1430, 2010.

[67] L. Straka, O. Heczko, H. Seiner, N. Lanska, J. Drahokoupil, A. Soroka, S. Fähler, H. Hänninen, and A. Sozinov. Highly mobile twinned interface in 10M modulated Ni–Mn–Ga martensite: Analysis beyond the tetragonal approximation of lattice. *Acta Materialia*, 59:7450–7463, 2011.

[68] R.C. Pond, B. Muntifering, and P. Müllner. Deformation twinning in Ni_2MnGa. *Acta Materialia*, 60(9):3976–3984, 2012.

[69] L. Straka, H. Hänninen, N. Lanska, and A. Sozinov. Twin interaction and large magnetoelasticity in Ni-Mn-Ga single crystals. *Journal of Applied Physics*, 109(6):063504, 2011.

[70] Le Zhou, Anit Giri, Kyu Cho, Helge Heinrich, Bhaskar S. Majumdar, and Yongho Sohn. Microstructural and crystallographic characterization of $Ni_{2+x}Mn_{1-x}Ga$ alloys ($x = 0.14, 0.16, 0.19, 0.22, and 0.24$) by transmission electron microscopy. *Metallurgical and Materials Transactions E*, 1(3):239–246, 2014.

[71] A. G. Khachaturyan, S. M. Shapiro, and S. Semenovskaya. Adaptive phase formation in martensitic transformation. *Physical Review B*, 43:10832–10843, May 1991.

[72] S. Kaufmann, U. K. Rößler, O. Heczko, M. Wuttig, J. Buschbeck, L. Schultz, and S. Fähler. Adaptive modulations of martensites. *Physical Review Letters*, 104:145702, Apr 2010.

[73] Oleg Heczko, Petr Cejpek, Jan Drahokoupil, and Václav Holý. Corrigendum to: "Structure and microstructure of Ni-Mn-Ga single crystal exhibiting magnetic shape memory effect analysed by high resolution X-ray diffraction" [Acta Mater. 115 (2016) 250–258]. *Acta Materialia*, 120:464 – 465, 2016.

[74] V. K. Pecharsky and K. A. Gschneidner, Jr. Giant magnetocaloric effect in $Gd_5(Si_2Ge_2)$. *Physical Review Letters*, 78:4494–4497, Jun 1997.

[75] Anders Smith, Christian R.H. Bahl, Rasmus Bjørk, Kurt Engelbrecht, Kaspar K. Nielsen, and Nini Pryds. Materials challenges for high performance magnetocaloric refrigeration devices. *Advanced Energy Materials*, 2(11):1288–1318, 2012.

[76] R. Santamarta, E. Cesari, J. Font, J. Muntasell, J. Pons, and J. Dutkiewicz. Effect of atomic order on the martensitic transformation of Ni–Fe–Ga alloys. *Scripta Materialia*, 54(12):1985 – 1989, 2006.

[77] O. Söderberg, Y. Ge, A. Sozinov, S-P. Hannula, and V. K. Lindroos. Recent breakthrough development of the magnetic shape memory effect in Ni–Mn–Ga alloys. *Smart Materials and Structures*, 14:S223–S235, 2005.

[78] T. Breczko, S. Illyashenko, D. Bykov, O. Korpusov, M. Bramowicz, and R. Grechishkin. Thermomagnetic analysis and domain structure in the phase transition region of Ni-Mn-Ga and Co-Ni-Ga shape memory alloys. *Reviews on Advanced Materials Science*, 20:101–106, 2009.

[79] R.W. Overholser, Manfred Wuttig, and D.A. Neumann. Chemical ordering in Ni-Mn-Ga Heusler alloys. *Scripta Materialia*, 40:1095–1102, 1999.

[80] MGML webpage. [online], `https://mgml.eu/`, Last visit 15. 7. 2021.

[81] J. A. Osborn. Demagnetizing factors of the general ellipsoid. *Physical Review*, 67:351–357, Jun 1945.

[82] M. Beleggia, M. De Graef, and Y. Millev. Demagnetization factors of the general ellipsoid: An alternative to the Maxwell approach. *Philosophical Magazine*, 86(16):2451–2466, 2006.

[83] Giorgio Bertotti. Chapter 3 - Maxwell's Equations in Magnetic Media. In Giorgio Bertotti, editor, *Hysteresis in Magnetism*, Electromagnetism, pages 73 – 102. Academic Press, San Diego, 1998.

[84] Brož Jaromír a kolektiv. *Základy fysikálních měření*. Státní pedagogické nakladatelství, n. p., 1967.

[85] A.A. Likhachev and K. Ullakko. Magnetic-field-controlled twin boundaries motion and giant magneto-mechanical effects in Ni–Mn–Ga shape memory alloy. *Physics Letters A*, 275(1):142 – 151, 2000.

[86] A. N. Vasil'ev, A. D. Bozhko, V. V. Khovailo, I. E. Dikshtein, V. G. Shavrov, V. D. Buchelnikov, M. Matsumoto, S. Suzuki, T. Takagi, and J. Tani. Structural and magnetic phase transitions in shape-memory alloys $Ni_{2+x}Mn_{1-x}Ga$. *Physical Review B*, 59:1113–1120, Jan 1999.

[87] Václav Valvoda, Polcarová Milena, and Pavel Lukáč. *Základy strukturní analýzy*. Nakladatelství a vydavatelství JP, 1992.

[88] Jens Als-Nielsen and Des McMorrow. *Elements of Modern X-ray Physics*. John Wiley & Sons Ltd, 2001.

[89] Juan Rodríguez-Carvajal. Fullprof suite [computer software]. `http://www.ill.eu/sites/fullprof/`, 1993-2006.

[90] J.M. Bijvoet, W.G. Burgers, and G. Hägg. *Early Papers on Diffraction of X-rays by Crystals*. Springer US, 1969.

[91] P. J. Becker and P. Coppens. Extinction within limit of validity of Darwin transfer equations. I. general formalisms for primary and secondary extinction and their application to spherical crystals. *Acta Crystallographica A*, A30:129 – 147, 1974.

[92] P. J. Becker and P. Coppens. Extinction within limit of validity of Darwin transfer equations. III. Non-spherical crystals and anisotropy of extinction. *Acta Crystallographica A*, A31:417 – 425, 1975.

[93] O. Heczko, A. Sozinov, and K. Ullakko. Giant field-induced reversible strain in magnetic shape memory NiMnGa alloy. *IEEE Transactions on Magnetics*, 36(5):3266–3268, 2000.

[94] Chengbao Jiang, Jinghua Liu, Jingmin Wang, Lihong Xu, and Huibin Xu. Solid–liquid interface morphology and crystal growth of NiMnGa magnetic shape memory alloys. *Acta Materialia*, 53(4):1111 – 1120, 2005.

[95] M. Ramudu, A. Satish Kumar, and V. Seshubai. Influence of boron addition on the microstructure, structural and magnetic properties of $Ni_{53.5}Mn_{26.0}Ga_{20.5}$ alloy. *Intermetallics*, 28:51 – 57, 2012.

[96] Yildirim Aydogdu, Ali Sadi Turabi, Mediha Kok, Ayse Aydogdu, Hirobumi Tobe, and Haluk Ersin Karaca. Effects of the substitution of gallium with boron on the physical and mechanical properties of Ni–Mn–Ga shape memory alloys. *Applied Physics A*, 117(4):2073 –2078, 2014.

[97] Dominik Kotzott, Martin Ade, and Harald Hillebrecht. Single crystal studies on boron-rich τ-borides $Ni_{23-x}M_xB_6$ (M=Zn, Ga, In, Sn, Ir) - The surprising occurrence of B4-tetrahedra as a normal case? *Journal of Solid State Chemistry*, 183(10):2281 – 2289, 2010.

[98] G. Erdélyi, H. Mehrer, A.W. Imre, T.A. Lograsso, and D.L. Schlagel. Self-diffusion in Ni_2MnGa. *Intermetallics*, 15(8):1078 – 1083, 2007.

[99] N. Xu, J. M. Raulot, Z. B. Li, J. Bai, B. Yang, Y. D. Zhang, X. Y. Meng, X. Zhao, L. Zuo, and C. Esling. Composition-dependent structural and magnetic properties of Ni–Mn–Ga alloys studied by ab initio calculations. *Journal of Materials Science*, 50(10):3825 – 3834, 2015.

[100] M.F. Qian, X.X. Zhang, L.S. Wei, L. Geng, and H.X. Peng. Effect of chemical ordering annealing on martensitic transformation and superelasticity in polycrystalline Ni–Mn–Ga microwires. *Journal of Alloys and Compounds*, 645:335–343, 2015.

[101] L. Straka, O. Heczko, V. Novák, and N. Lanska. Study of austenite-martensite transformation in Ni-Mn-Ga magnetic shape memory alloy. *Journal de Physique IV France*, 112:911–915, 2003.

[102] N. Scheerbaum, O. Heczko, J. Liu, D. Hinz, L. Schultz, and O. Gutfleisch. Magnetic field-induced twin boundary motion in polycrystalline Ni–Mn–Ga fibres. *New Journal of Physics*, 10(7):073002, Jul 2008.

[103] Ge Yanling. *The Crystal and Magnetic mictostructure of Ni-Mn-Ga Alloys*. PhD thesis, Helsinki University of Technology, 2007.

[104] Ming Yin, Philip Nash, Wei Chen, and Song Chen. Standard enthalpies of formation of selected Ni_2YZ Heusler compounds. *Journal of Alloys and Compounds*, 660:258–265, 2016.

[105] H.B. Xu, Y. Li, and C.B. Jiang. Ni–Mn–Ga high-temperature shape memory alloys. *Materials Science and Engineering: A*, 438-440:1065 – 1070, 2006. Proceedings of the International Conference on Martensitic Transformations.

[106] Fene Hu, Shengxian Wei, Yiming Cao, Zhe Li, Xijia He, Kun Xu, Yuanlei Zhang, Yanru Kang, Huimin Yang, and Qingqing Zhang. Magnetocaloric and barocaloric effects associated with two successive magnetostructural transformations in $Ni_{55.5}Mn_{17.8}Ga_{26.7}$ alloy. *Journal of Alloys and Compounds*, 818:153356, 2020.

[107] R. Chulist, L. Straka, N. Lanska, A. Soroka, A. Sozinov, and W. Skrotzki. Characterization of mobile type I and type II twin boundaries in 10M modulated Ni–Mn–Ga martensite by electron backscatter diffraction. *Acta Materialia*, 61(6):1913–1920, 2013.

List of Figures

List of Tables

List of abbreviations

MSM	Magnetic Shape Memory
MIR	Magnetically Induced Reorientation
MFIS	Magnetic Field Induced Stress
MCE	Magneto-caloric Effect
IMT	Intermartensitic transformation
EDX	Energy Dispersive X-ray Analysis
XRD	X-ray Diffraction

List of the used symbols

Crystallography and diffraction

a, b, c, γ	lattice parameters (of a monoclinic unit cell)
hkl	Miller indices of a crystallographic plane or diffraction indices
(hkl)	crystalographic plane with the indices hkl
hkl	form of crystalographic planes hkl
$[uvw]$	crystalographic direction with the indices uvw
d_{hkl}	interplanar distance of the crystalographic planes hkl
Θ, Θ_{hkl}	Bragg angle, Bragg angle corresponding to the scattering on the crystalographic planes with the indices hkl
ω	angle of incidence
F_{hkl}	structure factor of Bragg reflection hkl
$I_{hkl}^{integrated}$	integrated intensitiy of Bragg reflection hkl
S	correction of the integrated intensity for the irradiated area
A	absorption correction
L	Lorentz correction
P	polarisation correction
E_{hkl}	extinction correction for Bragg reflection hkl
λ	wavelength of the used X-rays
fcc	face-centered cubic (lattice/structure)
$Fm\bar{3}m$	symbol of the space group n. 225
$L2_1$, $B2'$	types of atomic ordering
ρ	relative ratio between $L2_1$, $B2'$ ordering
$\vec{q}_{mod}$	modulation vector
$\vec{U}$	vector of the modulation amplitude
φ	angle of rotation of the sample stage around the vertical axis
χ	angle of tilt of the sample stage around the horizontal axis

Measurement of the physical properties

T	temperature
T_{melt}	melting temperature
T_{boil}	boiling temperature
$T_{B2'\rightarrow L2_1}$	temperature of $B2' \rightarrow L2_1$ transition
T_M	temperature of the martensitic transformation
T_P	temperature of the pre-martensitic transformation
T_C	Curie temperature
M_s	start temperature of the austenite to martensite transformation (during the cooling)
M_f	finish temperature of the austenite to martensite transformation (during the cooling)
A_s	start temperature of the martensite to austenite transformation (during the heating)
A_f	finish temperature of the martensite to austenite transformation (during the heating)
$\vec{M}$	magnetisation
$\vec{H}$	magnetic field

μ_0	permeability of vacuum
N_d	demagnetisation factor
ϵ	density of the magnetic energy
L	latent heat
R	electrical resistivity
p	pressure, tension

List of publications

(to 6.8.2021)

- Kristupas Kazimieras Tikuisis, Jan Wyzula, Lukas Ohnoutek, Petr Cejpek, Klara Uhlirova, Michael Hakl, Clement Faugeras, Karel Vyborny, Akihiro Ishida, Martin Veis, Milan Orlita. Landau level spectroscopy of the PbSnSe topological crystalline insulator. *Physical Review B*, 103(15):155304, 2021.

- T. Krajnak, M. Janecek, P. Minarik, J. Vesely, P. Cejpek, J. Gubicza, P.T. Hung, D. Preisler, F. Novy, A.G. Raab, G.I. Raab, R. Asfandiyarov. Microstructure Evolution and Mechanical Properties of cp-Ti Processed by a Novel Technique of Rotational Constrained Bending. *Metalurgical and Materials Transaction A - Physical Metallurgy and Materials Science*, 50(5):1665 – 1678, 2021.

- Petr Cejpek, Petr Doležal, Petr Opletal, Jaroslav Valenta, Kristina Vlášková, and Milan Dopita. Temperature versus composition phase diagram and temperature evolution of structure and modulation of $Ni_2MnGa_{1-x}In_x$ single crystals. *Journal of Alloys and Compounds*, 855:157327, 2021.

- R. Silber, O. Stejskal, L. Beran, P. Cejpek, R. Antos, T. Matalla-Wagner, J. Thien, O. Kuschel, J. Wollschlager, M. Veis, T. Kuschel, J. Hamrle. Quadratic magneto-optic Kerr effect spectroscopy of Fe epitaxial films on MgO(001) substrates. *Physical Review B*, 100(6):064403, 2019.

- Petr Cejpek, Ladislav Straka, Martin Veis, Ross Colman, Milan Dopita, Václav Holý, and Oleg Heczko. Rapid floating zone growth of Ni_2MnGa single crystals exhibiting magnetic shape memory functionality. *Journal of Alloys and Compounds*, 775:533 – 541, 2019.

- G. Nemeth, K. Horvath, Ch. Hervoches, P. Cejpek, J. Palan, M. Duchek, K. Mathis. Characterization of the Microstructure, Local Macro-Texture and Residual Stress Field of Commercially Pure Titanium Grade Prepared by CONFORM ECAP. *Metals*, 8(12):1000, 2018.

- Kristupas Kazimieras Tikuisis, Lukas Beran, Petr Cejpek, Klara Uhlirova, Jaroslav Hamrle, Marek Vanatka, Michal Urbanek, Martin Veis. Optical and magneto-optical properties of Permalloy thin films in 0.7-6.4 eV photon energy range. *Materials & Design*, 114:31 – 39, 2017.

- Dominik Kriegner, Juergen Furthmuller, Raimund Kirchschlager, Jan Endres, Lukas Horak, Petr Cejpek, Helena Reichlova, Xavier Marti, Daniel Primetzhofer, Andreas Ney, Guenther Bauer, Friedhelm Bechstedt, Vaclav Holy, Gunther Springholz. Ferroelectric phase transitions in multiferroic $Ge_{1-x}Mn_xTe$ driven by local lattice distortions. *Physical Review B*, 94(5):054112, 2016.

- Oleg Heczko, Petr Cejpek, Jan Drahokoupil, Vaclav Holy. Structure and microstructure of Ni-Mn-Ga single crystal exhibiting magnetic shape memory effect analysed by high resolution X-ray diffraction. *Acta Materialia*, 115:250 – 258, 2016.

- L. Beran, P. Cejpek, M. Kulda, R. Antos, V. Holy, M. Veis, L. Straka, O. Heczko. Optical and magneto-optical studies of martensitic transformation in Ni-Mn-Ga magnetic shape memory alloys. *Journal of Applied Physics*, 117(17):17A919, 2015.

A Derivation of the SYCOS correction for the measurement of asymmetric diffraction

The sketch of the measurement of an asymmetric diffraction in the coplanar geometry is shown in Figure A.1. Corresponding to the sketch, point A is the center of the goniometer (goniometer axis), at the point B the beam scatters on the sample, C is the point where the scattered beam is detected and D is the expected position where the scattered beam should enter the detector when the sample is not shifted ($s = 0$).

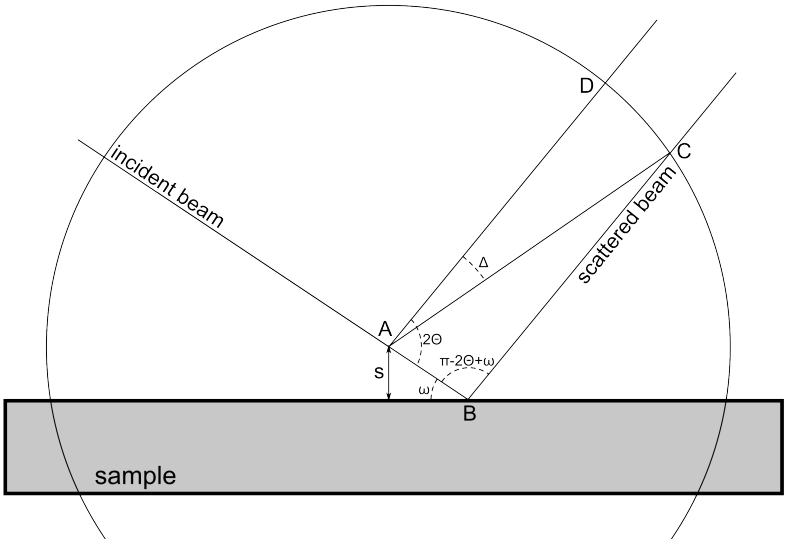

Figure A.1: The sketch of the measurement of an asymmetric diffraction in the coplanar geometry

According to the Figure A.1, we can write for the coordinates of individual points:

$$A = [0, 0] \tag{A.1}$$
$$B = [-s \cot \omega, s] \tag{A.2}$$
$$D = [R \cos (2\Theta - \omega), R \sin (2\Theta - \omega)] \tag{A.3}$$

where R is the radius of the goniometer (corresponding to the distance $|AC| = |AD|$) and s is the shift from the goniometer axis. The task is to find the coordinates of the point C.

Let's find the equation of the line p crossing the points B and C. For its directional vector $\vec{u}$ and its normal $\vec{n}$ we have:

$$\vec{u} = (\cos (2\Theta - \omega), \sin (2\Theta - \omega)) \tag{A.4}$$
$$\vec{n} = (\sin (2\Theta - \omega), -\cos (2\Theta - \omega)) \tag{A.5}$$

With the consideration of the equation for the line $p : ax + by + c = 0$ we obtain:

$$a = \sin(2\Theta - \omega) \tag{A.6}$$
$$b = -\cos(2\Theta - \omega) \tag{A.7}$$
$$c = s\left[\sin(2\Theta - \omega)\cot\omega + \cos(2\Theta - \omega)\right] = sK \tag{A.8}$$

The point C is the intersection of the line p and the circle with the equation $R^2 = x^2 + y^2$. Now, we have to solve the system of the equations:

$$R^2 = x^2 + y^2 \tag{A.9}$$
$$ax + by + c = 0 \tag{A.10}$$

The derivation of y leads to:

$$y_\pm = \frac{-\frac{bc}{a^2} \pm \sqrt{R^2\left(\frac{b^2}{a^2} + 1\right) - \frac{c^2}{a^2}}}{\frac{b^2}{a^2} + 1} \tag{A.11}$$

When we put the formulas A.8 into A.11 we obtain:

$$y_\pm = sK\cos(2\Theta - \omega) \pm \sin(2\Theta - \omega)\sqrt{R^2 - s^2K^2} \tag{A.12}$$

The y-coordinate of the C point corresponds to the solution y_+, because for y_- the detector would lie under the sample. When we put y_+ back in the equation for the line p, we can compute the x-coordinate. Together we have:

$$x_C = -sK\sin(2\Theta - \omega) + \cos(2\Theta - \omega)\sqrt{R^2 - s^2K^2} \tag{A.13}$$
$$y_C = sK\cos(2\Theta - \omega) + \sin(2\Theta - \omega)\sqrt{R^2 - s^2K^2} \tag{A.14}$$

The resulting correction for the 2Θ angle corresponds to the angle $\angle DAC$. It can be computed as:

$$\begin{aligned}\cos\Delta &= \frac{\overrightarrow{D-A}\cdot\overrightarrow{C-A}}{\left|\overrightarrow{D-A}\right|\left|\overrightarrow{C-A}\right|} \\ &= \frac{x_C x_D + y_C y_D}{R^2} \\ &= \frac{\sqrt{R^2 + s^2K^2}}{R} = \sqrt{1 - \frac{s^2K^2}{R^2}}\end{aligned} \tag{A.15}$$

Let's label $S = \frac{2s}{R}$ and we obtain the final formula for the 2Θ correction:

$$\Delta = \operatorname{sgn}(S)\arccos\left(\sqrt{1 - \frac{S^2}{4}\left[\sin(2\Theta - \omega)\cot\omega + \cos(2\Theta - \omega)\right]^2}\right) \tag{A.16}$$

Additionally, let's consider the symmetric case for Bragg-Brentano geometry where $\omega = \Theta$. We have $K = \sin\Theta\cot\Theta + \cos\Theta = \sin\Theta\frac{\cos\Theta}{\sin\Theta} + \cos\Theta = 2\cos\Theta$ and therefore:

$$\cos\Delta = \sqrt{1 - \frac{4s^2\cos^2\Theta}{R^2}} \tag{A.17}$$

Let's assume that the correction is small and because the shift s is much smaller than the radius of the goniometer, so $\Delta \ll 1$ and $s \ll R$. Therefore, we can use the Taylor expansion for the terms in Equation A.17 as:

$$1 - \frac{\Delta^2}{2} = 1 - \frac{4s^2 \cos^2 \Theta}{2R^2} \tag{A.18}$$

And we obtain:

$$\Delta = \frac{2s}{R} \cos \Theta \tag{A.19}$$

The resulting values of the function A.16 are shown in Figure A.2. The curves are plotted for the vertical shift $s = 0.1$ mm and the goniometer radius $R = 320$ mm (Panalytical X'Pert Pro MRD diffractometer) which corresponds to $S = 6.25 \cdot 10^{-4}$. The classical formula A.17 for Bragg-Brentano geometry corresponds to the curve with $\omega_{offset} = 0$ deg ($\omega = \Theta + \omega_{offset}$). The difference for the asymmetric geometry can be clearly seen at low angles - especially for negative ω_{offset} where the change is caused by low incident angles and corresponding dominance of the term $\cot \omega$ in Equation A.16.

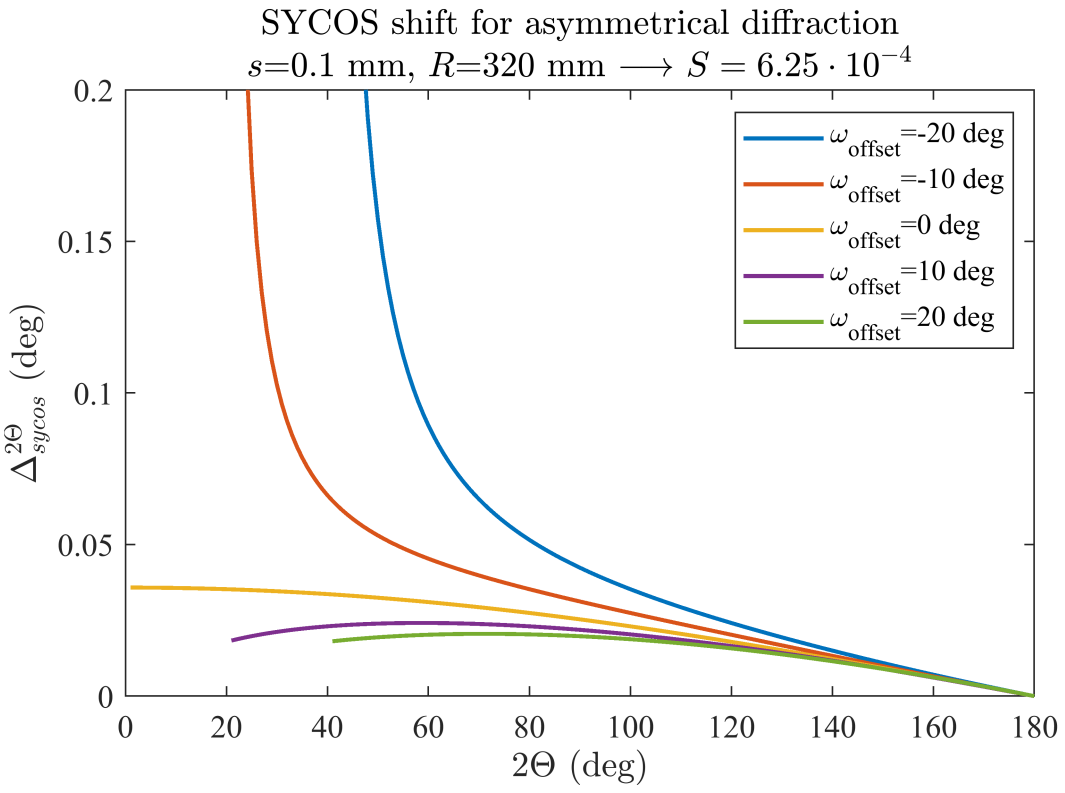

Figure A.2: Resulting sycos shift for different ω_{offset} ($\omega = \Theta + \omega_{offset}$).